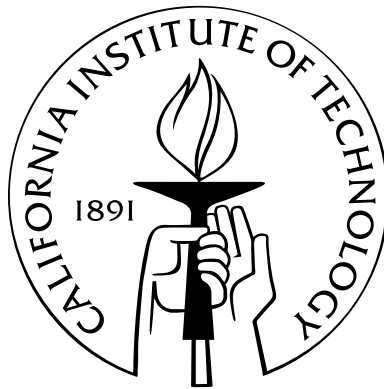# Wave Propagation in Granular Materials

Thesis by

Stephen R. Hostler

In Partial Fulfillment of the Requirements

for the Degree of

Doctor of Philosophy

California Institute of Technology

Pasadena, California

2005

(Defended October 12, 2004)

ii

Acknowledgements

I am particularly grateful to my advisor, Prof. Christopher Brennen, and Prof. Melany Hunt. My growth as a researcher and teacher is direct result of their mentorship and support. As a member of the Caltech Granular Flows Group, I had the opportunity to take part in a couple fairly adventurous research projects, namely field research at the Booming Dunes of Death Valley and the Mojave Desert and weightless research aboard the KC-135 ("vomit comet"). These experiences gave me invaluable research experience and were also quite a bit of fun. I thank Profs. Brennen and Hunt for giving me the chance to be a part of these projects. I would also like to thank the other members of my thesis committee, Prof. Tim Colonius and Prof. John Brady, for their valuable comments on my thesis.

I would like to thank those who helped with the setup of the experiments. In particular, I would like to thank Rodney Rojas for help in the machine shop and Raul Relles for help in the vibrations lab.

My time at Caltech has also been enriched by all of the other people I have known. I am grateful for discussions with Jim Cory, Gustavo Joseph, Kristo Kriechbaum, Matt Muto, and Steve Alves who were always willing to listen to my (often obscure) questions. More socially, I have had great time as a member of SOPS, the Aero soccer team, and the Thomas Lunch group.

Most of all I would like to thank my wife, Rochelle. First of all, I appreciate her willingness to move across the country. Secondly, I appreciate her love and support throughout my studies. I owe much of my success and the retention of the majority of my sanity to her support.

Abstract

Wave propagation is a fundamental property of all physical systems. The wave speed is directly related to the compressibility of the system and determines the rate at which local disturbances are propagated into the bulk of the material. The wave propagation characteristics of conventional forms of matter are well understood and well documented. In contrast, waves in granular materials are more complex due to the heterogeneous nature of these systems. The key element of the mechanics of a granular system is the force chain. It is along these preferentially stressed chains of particles that waves are transmitted. These nonlinear chains are heavily dependent on the geometry of the bed and are prone to rearrangement even by the slightest of forces.

Results from both experiments and simulations on wave propagation in granular materials are presented in the current study. The experiments measure the pressures at two points within the granular bed that result from the motion of a piston at one end of the bed. The simulations are a two-dimensional version of the experiments and use a discrete, soft-particle method to detect the wave at both the output of the simulated bed and at any point within it. In addition to examining wave propagation in a granular bed at rest, simulations and experiments are also performed for a granular bed undergoing agitation perpendicular to the direction of the wave input. Imposed agitation increases the granular temperature of the bed and allows for the exploration of the effect of granular state changes on the wave propagation characteristics. Such information may provide a means to diagnose the state of a flowing granular material.

Measurements of the wave speed and attenuation in the bed reveal the unique properties of waves in granular systems that result from the nonlinearity of the bed and the heterogeneity of the force chains. Sinusoidal waves demonstrate the nondispersive nature of a granular bed and show the transient effects of force chain rearrangement. Pulsed waves display a semi-permanent shape qualitatively similar to predictions from nonlinear wave theory. In an agitated granular bed, measurements of the wave characteristics were found to be possible even in the presence of significant agitation. The prevailing confining pressure, which changes throughout the agitation cycle, was determined to be the system parameter that correlates best with changes to the wave speed.

Contents

List of Figures

List of Tables

Chapter 1

Introduction

1.1 Granular materials and granular flows

Granular materials refer to any system composed of discrete, macroscopic particles. Examples include sand, coal, pills, grain, etc. For any of these materials, the particle size is on a comparable scale to the size of the total system. This similarity of scales leads to the heterogeneity observed in these systems.
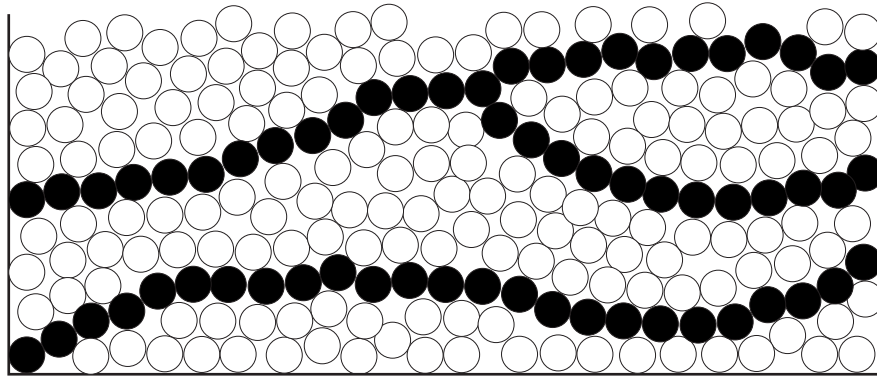
Figure 1.1: Force chains in a granular bed.

The heterogeneous nature of a granular bed is best illustrated by the concept of force chains. Force chains are chains of particles that carry a disproportionate amount of a given load due to geometrical effects. Figure 1.1 schematically depicts a few such chains that would result from the horizontal compression of the bed. Force chains are responsible for the nonisotropic distribution of stress in a granular pile (see photoelastic imaging of Geng *et al.* (2001)). Since wave propagation in granular materials is essentially the propagation of stress, these chains also are responsible for the propagation of pressure waves in a similar, heterogeneous manner. These chains are inherently fragile and susceptible to reorganization. Thus, repeatability is often a concern for experiments in granular materials. The irregular distribution of force chains also means that granular materials exhibit

strong configuration dependence. The results from experiments are often strongly influenced by the procedure used in preparation of the granular bed. More information on the unique characteristics of granular materials can be found in Duran (2000).

A granular *flow* is then any such system of discrete particles set into motion. Granular flows are a subset of all two-phase flows. In granular flows, the second phase is the interstitial fluid (liquid or gas) that occupies the space between particles. Forces in granular flows (as well as static granular materials) are predominantly the result of particle contact mechanics. Interstitial fluid effects, such as drag or particle cohesion due to surface tension effects, as well as electrostatic effects also may impact the forces in these flowing systems. We will neglect any of these additional forces in the simulations and consider them inconsequential to the experiments (see Wassgren (1997)).

Granular flows are omnipresent in industry and nature. In industry, granular materials compose the raw materials (ore, grain), the finished product (pharmaceuticals) or the intermediate processing stages (metal powder for sintering). The transport and processing of these materials requires knowledge of the characteristics of granular flows. Common transport techniques include chute and hopper flows. Processes include operations to sort and mix materials. Often, these processes are developed based on trial and error. Improving the theoretical development of granular flows will improve the efficiency of these operations, saving time and money.

Natural phenomena that involve granular flows cover the spectrum from the beautiful (sand dunes) to the dangerous (landslides, avalanches). The formation and evolution of sand dunes are governed by the interaction of sand and the prevailing winds, a situation in which the interstitial fluid is of utmost importance. The flow of sand down the steep face of a formed dune is a scenario ruled more by grain interactions. On some particular dunes, known as booming dunes, such flows give rise deep vibrational tone (Lindsay *et al.*, 1976; Nori *et al.*, 1997). These booming dunes have been identified since ancient times, but a full understanding of the mechanism that produces the sound has yet to be realized. The more hazardous side of natural granular flows include phenomena such as landslides, debris flows (mudslides), and avalanches. Estimates put the annual damage due to landslides at 25 to 50 deaths and \$2 billion nationally and thousands of deaths and injuries and billions of dollars globally (NDEC, 2004). Increased understanding of these flows would help identify susceptible areas and improve early warning systems to mitigate the damage caused by these natural disasters.

1.2   Waves in granular beds

In the current study, the focus is on pressure waves that are transmitted through the contacts of the particles in the granular bed. Such waves will be referred to as elastic waves. As alluded to earlier, the force chains in the granular bed will be the primary conduit of these waves. Since the particles are

Author	Material	Pressure (kPa)	Wave type	Speed ($\frac{m}{s}$)
Duffy and Mindlin (1957)	3.2 mm Steel	7 - 103	Compressional	274-549
Hardin and Richart (1963)	0.6-0.85 mm Ottawa sand	23 - 383	Compressional	213-488
Liu and Nagel (1992)	5 mm glass	1.5	Group velocity Time-of-flight	50-90 280 ± 30
Ben-Dor *et al.* (1997)	3.3 mm PVC 1.7 mm Al$_2$O$_3$ 1 mm Iron 0.45 mm Iron 0.45 mm Potash		Transmitted Wave	287 276 226 143 144
Jia *et al.* (1999)	0.4-0.8 mm glass	35-2500	Coherent (E)	500-1350

Table 1.1: Previously found wave speeds in granular materials

free to move relative to one another, these chains are easily deformed and broken. Simulations (Haff, 1987) and experiments (Liu, 1994) have shown the susceptibility of these chains to rearrangement. In the work of Liu and Nagel (1993), disturbances as weak as the thermal expansion of a particle far from the measurement point or the input of the pressure wave itself was found to change the wave propagation characteristics through the granular bed. For a flowing granular material these chains will be reorganizing constantly. Even static granular materials manifest interesting behavior due to the nonlinear nature of the contacts between the particles that form these chains (see Section 1.2.4).

A second type of wave is possible in granular systems. Waves in the particle concentration, known as kinematic or continuity waves, can exist in these systems. They are particularly common in relatively dilute systems such as granular gases (see Section 1.3.3). Elastic waves are the main interest and concentration waves will only be discussed in passing.

The primary characteristics of the wave propagation in the current study will be the wave speed and the attenuation of the wave energy. We first consider previous measurements of these quantities and the techniques used in these studies before turning to some theory on waves in granular beds.

1.2.1 Wave speed

Past experiments on wave propagation in granular materials have explored numerous experimental conditions and have used a variety of techniques to determine the wave speed. Not surprisingly, there is a wide range of reported wave speeds. One of the more important variables in the experiments is the pressure at which the wave speed measurement is made. The dependence of wave speed on pressure (or depth) is of particular interest in the field of soil mechanics and for such applications as oil exploration. Table 1.1 shows the wave speeds obtained in a number of earlier studies. The pressure range explored in each study is shown and the stated wave speeds are the corresponding values obtained at these pressure limits. The details of each study are described below.

Early wave speed experiments made use of the resonant column method to measure the wave

speed. This method involves exciting a column of granular material over a range of frequencies. A peak in the detected amplitude determines the resonant frequency. This frequency combined with the length of the specimen gives the wave speed. Duffy and Mindlin (1957) applied this method to a column formed from ball bearings packed into a face-centered cubic lattice. The packing was enclosed in a rubber bag and the bag was evacuated to varying degrees, leading to range of isostatic confining pressures. They found that the wave speed scaled with pressure to the 1/6 power (as their theory predicted) for pressures above 69 kPa. They explained the discrepancy in the scaling for lower pressures on a reduced number of particle contacts (the coordination number), due to variations in particle diameters. Their theory assumes particles of identical diameter. Hardin and Richart (1963) applied the same resonance method to a random packing of Ottawa sand. In addition to the confining pressure, they also examined the effect of void fraction and water saturation on the wave speed. In this the study, the wave speed was found to scale with confining pressure to the 1/4 power for both wet and dry sand.

The analytical work of Goddard (1990) attempted to explain the discrepancy in the pressure scaling. For Hertzian contacts, the scaling of the wave speed with pressure should be $c \sim p^{1/6}$. Goddard suggested two mechanisms for the quarter-power scaling observed at relatively low pressure by Duffy and Mindlin (1957). One explanation was based on a non-Hertzian contact at low pressures. At low pressure, Goddard argued that conical asperities dominate the interaction between particles. The second explanation was linked to macroscopic effects. Goddard suggested that the coordination number increased as the pressure increased. Both mechanisms were shown to display a 1/4 power scaling at lower pressure and a 1/6 power scaling at higher pressure. Granular dynamics simulations by Makse *et al.* (1999) support the coordination number argument for the pressure scaling transition. The simulation results for the bulk modulus, and thus the compressional wave speed, agreed well with analytic calculations (effective medium theory) if the increase in the coordination number with increasing pressure was taken into account. Velický and Caroli (2002) propose yet another explanation for the pressure scaling discrepancy. They attribute the quarter-power scaling to disorder induced stress fluctuations in the granular bed as opposed to the coordination number effect.

The unique characteristics of wave propagation in a macroscopic granular material were explored by Liu and Nagel (1993). The dependence of the propagation on a limited number of wave paths was accentuated by using 5 mm glass spheres. Measurements were made with an accelerometer of comparable size to an individual grain at distances as close as 4 cm from the wave source. Such an arrangement means that as few as 8 particles could separate the source and detector. The imposed pressure at the point of measurement was minimal as it was solely due to the weight of the overlaying particles and the depth was only 6 cm. The authors used two techniques to calculate the wave speed in the granular material and found two very different speeds. The time-of-flight measurement used the time required for a pulse introduced at the source to be detected at the buried accelerometer to

find the wave speed. In contrast, the group velocity measurement used a sinusoidal input at the wave source. The phase shift between the source and detected signals was found over a range of input frequencies. The group velocity was calculated from the slope of the resulting linear trend. The speeds from the two methods vary by roughly a factor of five and for both techniques there exists a wide range in the measurements. The authors insist that the discrepancy between the techniques is meaningful but offer little explanation.

The work of Jia *et al.* (1999) attempts to address the discrepancy in the wave speeds found by Liu and Nagel (1993). The authors use ultrasonic wave pulses to explore wave propagation in a frequency range passing through the effective wavelength that is comparable to the grain size. By doing this, they identify two distinct waves, which they term E and S waves. The E wave is a coherent, self-averaging wave with a narrow band of relatively low frequencies. Its effective wavelength is much larger than the particle size. They found that the speed of this wave scaled with pressure in accordance with effective medium theories- $v \sim p^{1/4}$ at lower pressures and $v \sim p^{1/6}$ at higher pressures. In contrast, the S wave had an irregular structure with an irregular, high frequency spectrum. This higher frequency signal had an effective wavelength comparable to the system grain size so it was argued that the irregular character of this wave was due to multiple scattering and interference in the granular material.

One application of granular materials is their use to mitigate shocks resulting from explosions. To this end, Ben-Dor *et al.* (1997) studied the interaction of a shock wave with a granular bed. They created a granular bed at the end of a long shock tube. The impact of the shock led to a series of waves in the bed. They identified each wave (transmitted, compaction, and weak rarefaction wave) from pressure traces. Their transmitted wave appears most similar to the waves encountered in the current study, but there are some doubts about their similarity. Since the same wave is detected at sensors measuring the pressure through the granular material as well as at sensors measuring the air pressure, this wave may not be traveling through the contact network of the granular material. Additionally, the variation of the measured wave speed with material composition and particle size is contrary to what should be expected for wave propagation through a granular material.

1.2.2 Dissipation

In a granular bed, there are a number of mechanisms through which wave energy is dissipated. Since particle contacts are inelastic and frictional, some energy is lost during particle interactions. Frictional effects convert some of the wave energy into heat. Plastic deformation of the particles can also absorb some of the wave energy. A second loss mechanism involves rearrangement that is possible within the granular bed. Some energy can be converted to kinetic energy of a particle when it breaks loose from its neighbors. A third mechanism, at least an apparent mechanism, is the scattering of wave energy through the particle contact network. Wave energy can scatter away from

the point at which measurements are made giving the appearance that the energy has been lost. In reality, the energy is not lost but merely redirected.

The body of work on dissipation of waves in granular materials is much more limited. Information about dissipation is available with any wave speed measurement, but results for dissipation are rarely published.

We now turn from past work on wave propagation in granular materials to some theoretical developments for these systems. These theories will be used in subsequent chapters to understand the results from our experiments and simulations.

1.2.3   Linear waves

Some elements of linear wave theory will be used for purposes of rough analogy. The granular bed is highly nonlinear so one must be cautious in applying linear theory. Despite the complexity of the system, some phenomena of linear waves provide a do good qualitative description of some observations of our strongly nonlinear system.

In this section, the derivations will be presented following Lighthill (1978).

1.2.3.1   Dispersion

To measure the wave speed, we examine two measurements separated by a distance, L, in space. The speed will be this distance divided by the time shift, T, between the arrival of the wave at the two measurement points as given by

$$c(\omega) = \frac{L}{T(\omega)}. \tag{1.1}$$

In general, the phase speed, c, could vary with the frequency, ω, of the disturbance. For nonlinear waves, the speed could also be a function of the wave amplitude. For convenience, we replace the time shift with the phase shift, ϕ, given the relationship, $\phi(\omega) = \omega T(\omega)$, resulting in

$$c(\omega) = \frac{L}{\phi(\omega)}\omega. \tag{1.2}$$

Waves are considered nondispersive if the phase speed is not a function of its frequency. That is, a wave composed of several frequencies will remain coherent over time for a nondispersive wave. For a dispersive wave, the frequency components of the wave separate over time as each moves with a different speed. The phase speed for linear nondispersive waves can then be considered a constant, $\hat{c}$, and the phase can be shown to vary linearly with frequency ($f = \frac{\omega}{2\pi}$),

$$\phi(f) = 2\pi \frac{L}{\hat{c}} f. \tag{1.3}$$

The group velocity is defined as

$$U = \frac{d\omega}{dk}, \tag{1.4}$$

where k is the wavenumber. The group velocity can be rewritten in terms of the cyclic frequency, f, and phase shift, ϕ as

$$U = 2\pi L \frac{df}{d\phi}. \tag{1.5}$$

Thus, in a harmonically excited system, if the dependence of the phase shift on the frequency is known, the group velocity can be determined from the derivative of this relationship. If the phase shift is linear with frequency, the group velocity is a constant and the system is nondispersive.

1.2.4 Nonlinear waves
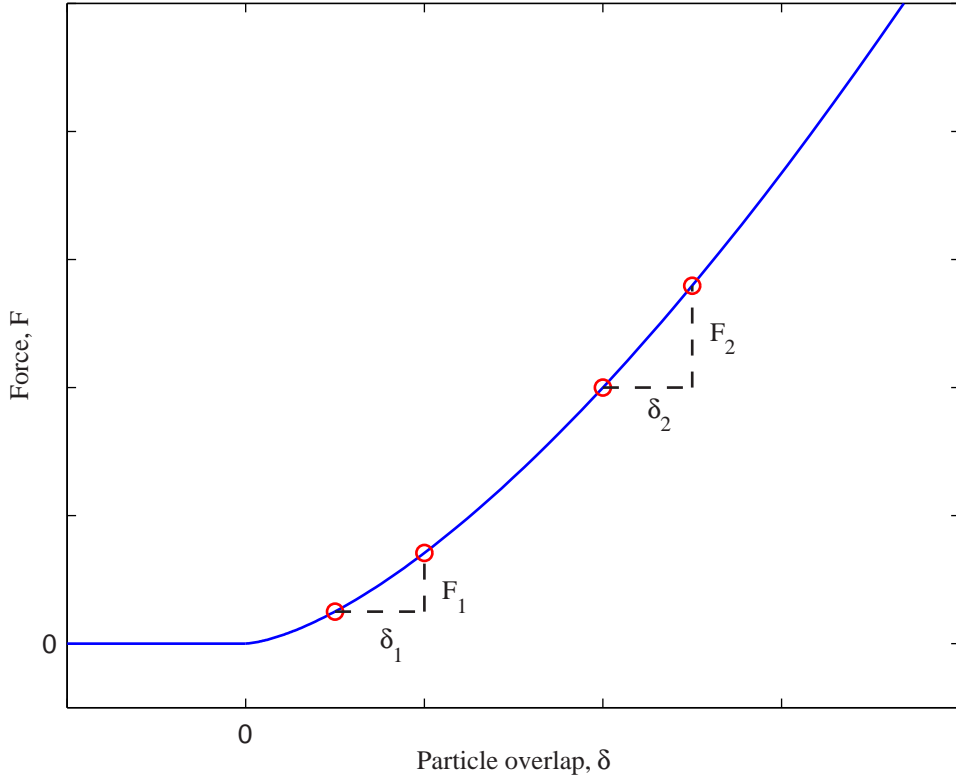
Figure 1.2: Force-displacement relationship for a Hertzian contact between two spheres.

Granular materials are inherently nonlinear. This can be seen by examining the interaction of two particles. The force between the two particles is given by a power-law in terms of the overlap between the particles, $F = \delta^n$, where δ is the particle overlap. For two perfectly spherical particles, the exponent is $3/2$ as given by Hertz's Law:

$$F = K_2 \delta^{3/2}, \tag{1.6}$$

where $K_2 = \frac{2E}{3(1-\nu^2)} \left(\frac{R_1 R_2}{R_1 + R_2} \right)^{1/2}$. R_1 and R_2 are the radii of the particles and E and ν are Young's modulus and Poisson's ratio, respectively, for the particle material. The relationship between force and particle overlap is shown in Figure 1.2. When the particles are in contact ($\delta > 0$), the nonlinearity is such that a greater force ($F_2 > F_1$) will result from the same incremental displacement, $\delta_1 = \delta_2$, for two particles in a greater state of prestress. This nonlinear dependence is due to geometrical effects alone. A second nonlinear effect occurs when the particles lose contact. Naturally with zero particle overlap, there is no force. These nonlinearities give rise to a number of nonlinear wave phenomena. These waves are similar to those seen in conventional fluid mechanics (Whitham, 1974; Leibovich and Seebass, 1978) and plasmas (Infeld and Rowlands, 2000) and a number of other systems.

The nonlinear waves that are possible in granular materials can be seen by studying a simplified geometry compared to Figure 1.1. The ultimate idealization of a force chain is a 1-D chain of particles (shown in Figure 1.3). The chain is compressed by an initial static force, F_0, that leads to an initial overlap, δ_0, between any two particles. In the present study, there is no applied static force, per se. Initial compression of the force chains arises from the overburden of granular material and the constraint of the side walls. Consequently, this initial compression is expected to be small compared to the piston amplitudes used to produce waves in the system.

Figure 1.3: Idealization of a force chain: 1-D chain of particles.

Following the derivation by Nesterenko (2001), a system of equations can be written to describe the motion of each particle in a 1-D chain of identical particles as

$$\ddot{u}_i = B \left(\delta_0 - u_i + u_{i-1} \right)^{3/2} - B \left(\delta_0 - u_{i+1} + u_i \right)^{3/2}. \tag{1.7}$$

Here, u is the displacement of particle i from its static displacement due to the imposed force, F_0, and B ($= \frac{K_2}{m}$) is a factor based on the properties of the particles.

Nesterenko (2001) showed that nonlinear wave solutions exist in this 1-D chain system in two limits. One limit is a situation in which particle displacements are very small compared to the initial overlap due to the confining force, F_0. Nesterenko termed this situation the strongly-compressed chain. The other limit is the opposite case in which the particle displacement is large or comparable to the initial overlap. The next two sections recount the derivation of Nesterenko (2001) for both of these limits.

1.2.4.1   Strongly compressed chain

A strongly-compressed chain corresponds to a situation in which

$$\frac{|u_i - u_{i-1}|}{\delta_0} \ll 1. \tag{1.8}$$

Applying this condition with the anharmonic approximation, Equation 1.7 can be rewritten as

$$\ddot{u}_i = \alpha \left(u_{i+1} - 2u_i + u_{i-1}\right) + \beta \left(u_{i+1} - 2u_i + u_{i-1}\right)\left(u_{i-1} - u_{i+1}\right), \tag{1.9}$$

where $\alpha = \frac{3}{2}B\delta_0^{1/2}$ and $\beta = \frac{3}{8}B\delta_0^{-1/2}$.

Assuming that the wavelength of the disturbance is larger than a particle diameter (the long-wave approximation), the individual particle displacements, u_1, neighboring displacements can be expanded in exponential series about a central point ($u_i = u(x)$, $u_{i-1} = e^{-2RD}u(x)$, $u_{i+1} = e^{2RD}u(x)$, $D = \frac{\partial}{\partial x}$) into a continuous displacement variable, $u(x)$. Using this expansion and neglecting higher order terms, Equation 1.9 leads to the nonlinear wave equation

$$u_{tt} = c_s^2 u_{xx} + 2c_s\gamma u_{xxxx} - \sigma u_x u_{xx}, \tag{1.10}$$

where $c_s^2 = B\delta_0^{1/2}6R^2$, $\gamma = \frac{c_s R^2}{6}$, and $\sigma = \frac{c_s^2 R}{\delta_0}$.

Now, applying the transformation $\xi = -u_x$ leads to the Korteweg-de Vries equation

$$\xi_t + c_s\xi_x + \gamma\xi_{xxx} + \frac{\sigma}{2c_s}\xi\xi_x = 0. \tag{1.11}$$

One exact solution of this equation is a soliton solution of the form

$$\xi - \xi_0 = \Delta\xi = \Delta\xi_m sech^2\left[\left(\frac{\sigma\delta\xi_m}{24c_s\gamma}\right)^{1/2}(x - Vt)\right], \tag{1.12}$$

where $V = c_s + \frac{\sigma}{6c_s}\Delta\xi_m$ is the soliton phase velocity. $\Delta\xi_m$ is the maximum strain amplitude and $T_{ws} = \left(\frac{24c_s\gamma}{\sigma\Delta\xi_m}\right)^{1/2}$ is the characteristic width of the wave.

Solitons have several unique properties. One is their resistance to shape change. Solitons maintain their shape as they propagate. Even after a collision with another soliton, both waves emerge from the interaction with no change in their shape or speed.

The shape of a soliton is plotted in Figure 1.4 for three different values of the amplitude for a fixed value of $\frac{\sigma}{24c_s\gamma}$. The width of the wave increases as the amplitude decreases. This 1-D theory does not include any effects of dissipation so there will be no decay in the amplitude over time. Real granular materials are dissipative, so any soliton observed in experiments will not be able to maintain the permanent shape predicted by the theory and will exhibit a decrease in its amplitude.

It is yet to be seen whether a decrease in the amplitude due to attenuation will translate into a width increase in accordance with the theory.
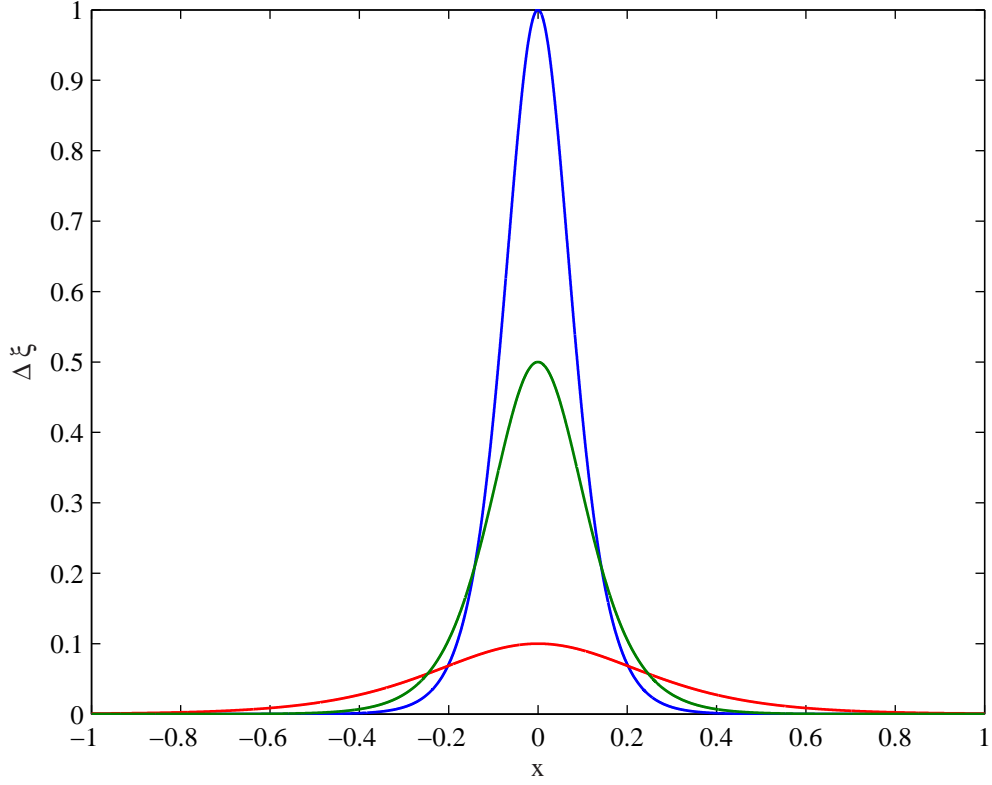
Figure 1.4: Soliton solutions to the Korteweg-de Vries equation.

1.2.4.2 Weakly compressed chain

A weakly-compressed chain corresponds to a situation in which

$$\frac{|u_{i+1} - u_i|}{\delta_0} \gtrsim 1. \tag{1.13}$$

The starting point is again the system of equations for a chain of particles, Equation 1.7. Given the weakly-compressed condition, the initial compression, δ_0, can be neglected in this equation to give

$$\ddot{u}_i = B \left(u_{i-1} - u_i \right)^{3/2} - B \left(u_i - u_{i+1} \right)^{3/2}. \tag{1.14}$$

The long-wave approximation allows for the displacement at neighboring points to be expanded in power series about a central point, $u_i = u$

$$u_{i-1} = u - u_x(2R) + \frac{1}{2}u_{xx}(2R)^2 - \frac{1}{6}u_{xxx}(2R)^3 + \frac{1}{24}u_{xxxx}(2R)^4 + \ldots, \tag{1.15}$$

$$u_{i+1} = u + u_x(2R) + \frac{1}{2}u_{xx}(2R)^2 + \frac{1}{6}u_{xxx}(2R)^3 + \frac{1}{24}u_{xxxx}(2R)^4 + \ldots. \tag{1.16}$$

These are substituted into Equation 1.14 and then the terms to the 3/2 power are expanded into additional series. Some simplification and the introduction of the strain ($\xi = -u_x$) leads to the equation

$$\xi_{tt} = c_w^2 \left\{ \xi^{3/2} + \frac{(2R)^2}{12} \left[\left(\xi^{3/2} \right)_{xx} - \frac{3}{8}\xi^{-1/2}\xi_x^2 \right] \right\}_{xx}, \tag{1.17}$$

where $c_w^2 = B(2R)^{5/2}$. By looking for stationary solutions of the form $u(x - Vt)$, a solitary wave solution is found

$$\xi = \left(\frac{5V_p^2}{4c_w^2} \right)^2 \cos^4 \left(\frac{\sqrt{10}}{5(2R)}x \right), \tag{1.18}$$

where V_p is the phase speed of the periodic wave and is a function of the minimal and maximal strains.
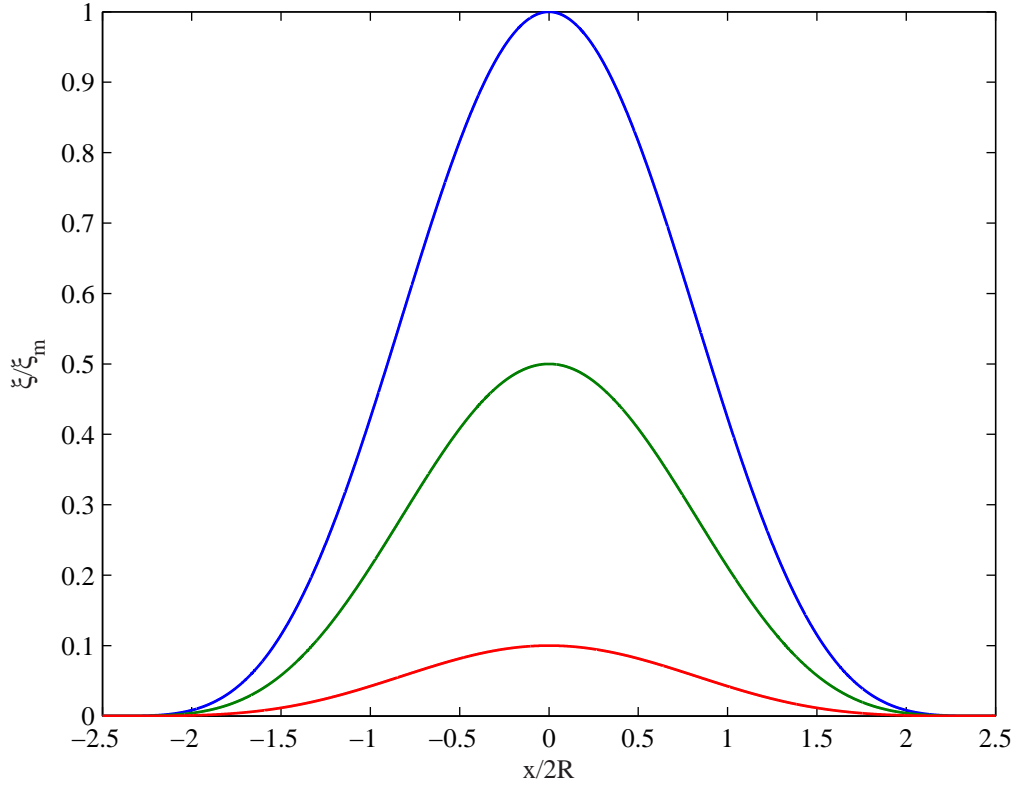
Figure 1.5: Solitary wave solution. Length is normalized by the particle diameter.

The shape of a solitary wave based on this equation is plotted in Figure 1.5 for three different values of the amplitude. Unlike the soliton in Figure 1.4, this wave has the same width regardless of amplitude. The width of the wave in Figure 1.5 is roughly five particle diameters and is not dependent on any system parameter.

Several studies have examined such 1-D chains of particles to verify the existence of these solitary waves in real granular systems. Nesterenko (1984) observed these waves in simulations and made comparisons to the theory. The first experimental measurements of solitary waves in 1-D particle chains were made by Lazaridi and Nesterenko (1985). More extensive experiments were conducted by Coste *et al.* (1997). In this study, the authors compared the detected wave shapes to the 1-D theory. They also measured the wave speed through the chain as a function of the confining force on the chain and compared this scaling with that predicted by the 1-D theory.

The bulk of the discussion to this point has focused on wave propagation through a granular material in a state of rest. For a flowing granular material, there can be additional complications. Most notably, force chains in an agitated or flowing granular material will be actively rearranged.

1.3 Thermodynamic analogy for granular flows

In considering granular flows, an analogy to homogeneous matter can be made by viewing the particles in a granular system as molecules. In this sense, we can think of a granular solid, liquid, or gas (Jaeger *et al.*, 1996). As temperature determines the state of standard matter, the granular temperature will determine the phase transitions in a granular flow. The notion of a granular temperature was first introduced by Ogawa (1978) and is defined as

$$T = \left\langle \vec{u}'^2 \right\rangle, \tag{1.19}$$

where $\vec{u}'$ is the instantaneous deviation from the mean velocity and $\langle \ \rangle$ represents an appropriate average.

There are two limitations of such a description. First, granular materials are inherently dissipative due to inelastic contacts. Thus, granular systems have an ever-present energy sink. In order to maintain a granular temperature, energy must be constantly supplied to the system. Second, for standard matter there are a sufficient number of molecules in a given sampling volume to apply the continuum hypothesis and form proper averages of continuous properties such as pressure, temperature, etc. In contrast, granular flows typically have too few particles per sampling volume to define continuum properties. Nevertheless, a thermodynamic analogy provides a useful framework for describing a number of phenomena in granular flows, particularly when examining transition in granular flows.

Granular Solid   Granular Liquid   Granular Gas
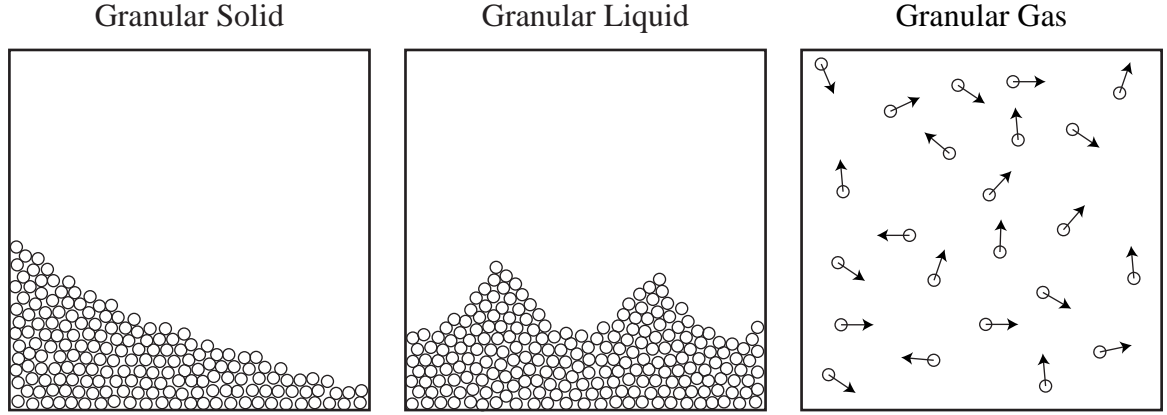
Figure 1.6: States of a granular material.

1.3.1 Granular solid

A granular solid is the lowest energy state of a granular flow. A granular material in the solid state is depicted in the left of Figure 1.6. Like a conventional solid, a granular solid can resist shear. Granular solids can also maintain an angle of repose up to which flow will not occur.

Wave propagation in a granular solid will be dictated by the geometrical configuration of the force chains in the system. Waves will travel over this fragile, yet persistent (in comparison to the other granular states), force network.

1.3.2 Granular liquid

With a sufficient amount of energy input to a granular system, the system will transition to a granular liquid state. The center of Figure 1.6 shows the liquid granular state. This state is characterized by a number of properties common to conventional liquids. Granular liquids cannot hold an angle of repose and have limited resistance to shearing. There is relative particle motion and circulation cells are established within the bulk of the granular material as the result of interaction at the system boundaries. A level free surface will be formed as at a conventional liquid-gas interface. Surface waves in granular materials, similar to surface-gravity waves at a conventional liquid-gas interface, also have been observed in both experiments and simulations (Wassgren, 1997).

The picture of wave propagation in a granular liquid is also governed by the forces chains, but in the liquid state this network is even more tenuous. Relative particle motion and convection lead to continuous rearrangement of the contact network. As long as particle contacts are maintained long enough for a wave to be transmitted, elastic wave propagation is still possible.

1.3.3 Granular gas

Further energy input can lead to a granular gas state. This state is shown in the right of Figure 1.6. Like a conventional molecular gas, these systems are collisional in nature with few lasting particle contacts. Granular materials in a gaseous state are also comparatively dilute. As the particles are quite energetic in these systems, these flows are often referred to as rapid granular flows. A thorough review of such flows can be found in Campbell (1990).

Wave propagation through a granular gas is completely different in character from that in a granular solid or liquid. Since particle contacts are rare and short in duration, waves cannot be propagated through chains of particle contacts. The only possibility is a wave in the concentration of particles that transmits the energy of the wave input source by the action of more frequent particle collisions. Since the speed of sound based on granular temperatures in granular gases is relatively low, these waves most often take the form of shocks (Kamenetsky *et al.*, 2000; Harada *et al.*, 2003).

1.3.4 Agitated granular beds

In experiments, the source of energy used to maintain or raise the granular temperature is most often an applied shaking of the granular bed. Transitions are predicted at particular values of Γ, the ratio of the applied acceleration amplitude to the acceleration of gravity. Clearly, $\Gamma = 1$ will be the point at which the floor of a granular bed will be pulled away from its maximum displacement faster than the bed can fall under gravity.

Another possible energy source in experiments is a drag force imparted by a flowing fluid as in the case of a fluidized bed. In naturally occurring granular flows, the driving force that sustains a granular temperature is usually a gravitational potential, such as an inclined slope.

1.4 Simulation background

The simulations used in the current study utilize the Discrete Element Method (DEM). Such simulations are similar to molecular dynamics simulations and are applied frequently to granular flows. A full description of the simulation technique can be found in Section 2.2. Here, we will focus on the past applications of the DEM to granular flows with particular emphasis on prior work done on simulated wave propagation in granular materials.

The first application of the discrete element method to granular materials was done by Cundall and Strack (1979). The code was originally developed to study problems in rock mechanics. In the cited paper, the authors numerically reproduced force-vector plots obtained through experiments using photoelastic particles. The simulations were able to minutely show the contact network of stresses in a compressed 2-D sample.

Discrete element simulations by Haff (1987) examined pressure waves that are transmitted as a result of shaking a granular bed. Such waves are relatively large in amplitude since the shaking typically exceeds the gravitational pull on the particles. In these studies, the authors filled the simulation cell through "pouring", leading to a geometrical configuration defined by the equilibrium of the interparticle forces. The observed phase difference between the force at the bed floor and the force measured on a piston at the top of the bed demonstrated the speed of the pressure wave that was transmitted through the bed. In a more recent paper, Potapov and Campbell (1996) examined similar pressure waves in a deep (1000 mean particles) granular bed. They observed shock-like structures due to an increase in the local wave speed behind a passing pressure wave due to an increase in the local coordination number.

Other recent work has focused on comparatively weak pressure wave propagation in granular materials. In these studies, the pressure wave is introduced in a direction perpendicular to the pull of gravity. Leibig (1994) attempted to reproduce some of the experimental results of Liu and Nagel (1992) with a simplified packing geometry. He modeled the granular bed as a square lattice of identical particles connected by linear springs. The only disorder in the system was a random distribution of spring constants. Dissipation and gravity were also included. Despite the simplicity, these simulations were able to capture much of frequency dependent behavior of the experiments and also showed wave localization. Melin (1994) performed similar simulations, but included a few additional elements of complexity. He formed the granular bed on a triangular lattice with nonlinear, Hertzian springs connecting the particles. Some simulations had identical particles, while others included a distribution of particle diameters. He examined the dependence of the wave speed with depth by looking at the shape of the wave front. The predictions of the simulations were not consistent with the theoretical predictions (Goddard, 1990) for the depth dependence. In an effort to reduce the computational effort, neither of these simulated systems included the positional disorder that is inherent in granular experiments. Both simulations placed the particles in regular arrays.

Chapter 2

Experiments and Simulations

2.1 Experiments

The experimental setup is depicted in Figure 2.1. A clear, Plexiglas box (25x25 cm floor) is filled
with a granular material to a depth of 16.5 cm by pouring in the particles with attention paid to
avoiding any unnecessary compaction of the bed. This procedure defines the loose state of the bed.
A circular piston (diameter 10 cm, 1/4 in thick, center 8 cm above floor) is used to create the
wave disturbances in the horizontal direction. The piston is driven by an electromechanical shaker
(Acoustic Power Systems ELECTRO-SEIS 113: 15.9 cm max. peak-to-peak displacement, 0-2000
Hz frequency range, 133 N max. force), which is controlled by either a function or a pulse generator.
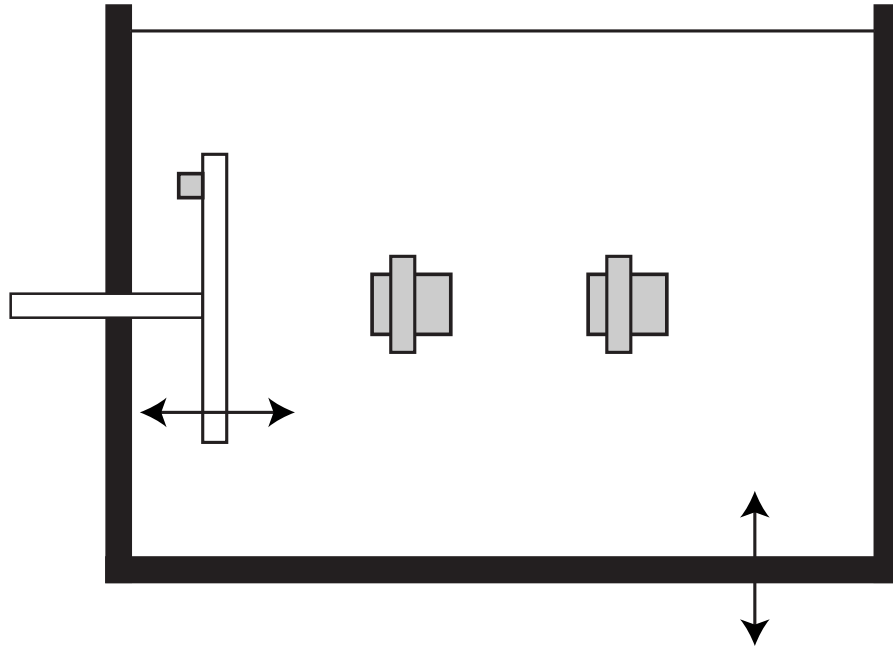
Figure 2.1: Schematic of the experimental setup. Two pressure transducers are buried in a granular
bed. The bed can be shaken vertically. Pressure waves are introduced horizontally via the piston,
whose motion is monitored by an accelerometer.

Two strain-gauge pressure transducers (Honeywell AB/HP ABH006PGC1B: 0-6 psi, 1.9 cm active face) are buried in the bed at the same depth but at different distances from the piston. The near transducer is typically placed 50 mm from the piston and the far transducer is located 50 mm or more beyond this point. They are held fixed from above with lab clamps and offset laterally so that the near transducer minimally obstructs the propagation of the signal to the far transducer. Holding the transducers rigidly in this manner allows for accurate determination of their distances from the piston and maintains this distance even when the bed is agitated. Further, the location of the transducer diaphragm is held stationary as the moving piston compresses the particles between the piston and the transducers. The alternative would be to bury the transducers in the bed without any link to the container, essentially "floating" them in the granular bed. Due to concerns about the repeatability of the results in such a "floating" configuration, the transducers were held fixed in all experiments. The output from the transducers is relatively weak (0-100 mV), so the signals are amplified (Sensotec Inline Amplifier 060-6827-01) before being sent to the data acquisition system.

The data acquisition system consists of a computer with a data acquisition card. In the course of the experiments, two different cards were used. The earlier experiments (sinusoidal input) made use of a high speed card (Measurement Computing PCI-DAS4020/12: Max. 20 MHz sampling rate) set to take data at 100,000 samples per second. For the later experiments (pulsed input), a more moderate speed card (Measurement Computing CIO-DAS16/M1: Max. 50 kHz sampling rate) was used. Data was taken at its maximum sampling rate. Programs were written in Labview and then Matlab to interface with the acquisition cards.

The motion of the piston is monitored by an accelerometer (Dytran 3150A3: 1-3000 Hz frequency range, $\pm 50g$ acceleration range) attached to its back surface. The entire apparatus is mounted atop a second electromechanical shaker (MB Dynamics PM-500HP: 2" max. peak-to-peak displacement, DC-3000 Hz frequency range, 80g peak acceleration) which provides agitation of the bed through vertical shaking. The motion of the shaking is measured with a second accelerometer, identical to that used on the piston.

Vertical shaking serves two purposes in the experiments. One use is to consolidate the bed. To create a consolidated bed state, the bed is shaken for several minutes at a frequency of 20 Hz and an acceleration amplitude over 1g. Over this time, the depth of the material drops a distance of about 1 cm. The bed is considered consolidated once the depth appears to stabilize. The second use of shaking is to create an agitated state in which to make measurements. Shaking leads to a nonzero granular temperature (defined in Section 1.3). The goal is to relate this degree of random particle motion with the wave propagation characteristics of the bed.

In response to concerns about wave reflection from the box walls, the box was internally lined with foam rubber. It was found that the presence of the foam had no discernable effect on the results. This fact is likely a result of the high attenuation in the granular bed. All of the wave

energy is dissipated before a wave can complete a reflection path. In the end, the foam was only used on the rear wall of the box behind the piston for cases in which the accelerometer was not needed. For these cases, the foam served two purposes. First, it reduced the possibility of waves reflecting off of the back wall, the shortest possible reflection path. Secondly, the foam allowed for the piston to be less constrained by the granular material. The piston was pulled back against the foam so that particles only contacted the front face. This was preferable to surrounding the piston with granular material.

Measurements of the wave speed in the granular bed were made by determining the difference in the arrival time of the wave at the two transducers. For the continuous, sinusoidal input experiments, the phase shift between the signals arriving at the two transducers was found by cross-correlation. This phase shift leads to a corresponding time shift which was used to calculate the phase speed. The phase speed of waves traveling through the granular bed is the distance between the transducers divided by the time shift. For the single pulse experiments, determination of the difference in the arrival time is made more directly. In each sensor output, the point is identified at which the pressure leaves its static value due to the arrival of the wave. The time shift is the difference between these arrival times and the wave speed follows as before.

Attenuation data was also gathered by comparing the amplitudes of the signals received by the two transducers. The attenuation is plotted, as is customary, as

$$\lambda = \frac{\ln \frac{\Delta p_2}{\Delta p_1}}{x_1 - x_2}, \tag{2.1}$$

where Δp_1 and Δp_2 are the amplitudes measured at distances, x_1 and x_2, respectively, from the piston. This assumes exponential decay of the amplitude ratio with distance. Experiments show this functional form to be an accurate description (see Figure 4.2).

A variety of granular materials were used in the experiments. A listing of their properties is given in Table 2.1. The glass beads of various diameters allow for the examination of particle size effects. The plastic particles permitted the evaluation of different material compositions, as characterized by E and ρ, and the effect of particle geometry. None of the plastic particles have the uniform, spherical geometry of the glass. The PVC and polyethylene particles are cylindrical and the polypropylene particles are spheroidal. One can imagine that the angularity of the contact, particularly with the PVC, will strongly affect the packing and rearrangement characteristics of the particles.

2.1.1 Continuous input

Sinusoidal piston excitation involved the input of waves of a particular frequency. By controlling the frequency of the waves, the dispersion relation of the granular system could be found. The frequency of the waves along with their amplitude (in terms of an acceleration amplitude) was specified and

Material	Shape	$\rho \left(\frac{kg}{m^3}\right)$	E (GPa)	ν	c_0 $\left(\frac{m}{s}\right)$	Size (mm)
Glass	Spherical	2500	70.3	0.220	5300	0.3, 2, 3, 4, 5
PVC	Cylindrical	1500	2.75	0.420	1350	1 x 3
Polyethylene	Cylindrical	921	0.24	0.38	515	4 x 3
Polypropylene	Spheroidal	900	1.5	0.3	1290	~ 1

Table 2.1: Material properties of the granular materials used in experiments. Material properties from `http://www.mindrum.com/tech.html` (glass) and `http://www.dow.com` (plastic).

sent to the system from a function generator. The signals received at the transducers are also sinusoidal. Wave speeds are determined by cross-correlating the signals to get a time shift between the wave arrival at each transducer. The amplitude of the wave is just the pressure amplitude of the detected wave. The effect of changing both the frequency and amplitude was examined.

In one class of experiments, the acceleration amplitude of the piston was fixed and the frequency was swept through a range of 50-2500 Hz. Due to the dynamics of the piston-shaker assembly, running at a fixed acceleration amplitude was nontrivial. The dynamic response of this assembly is shown in Figure 2.2 where the measured acceleration of the piston is shown for a fixed voltage input to the shaker over a range of frequencies. Thus, at each frequency during the experiments, the acceleration amplitude had to be tuned to the desired piston acceleration value to counteract the dynamics of the wave source. There is a particularly strong response of the piston around 600 Hz. This peak is present even in the absence of granular material so it cannot be caused by a resonance of the box or the granular bed. Thus, it must be the result of the piston, connecting rod, or the shaker. After achieving the desired acceleration, the wave (phase) velocity and attenuation were measured at each frequency. The dependence of the phase velocity on frequency allowed construction of the dispersion relation for the granular bed.

Another class of experiments involved the converse: the frequency was fixed and the amplitude was varied. Due to concerns of bed rearrangement as a result of the passage of these waves of ever-increasing amplitude, a few additional procedural steps were taken. The amplitude was first increased to a maximum acceleration level and then decreased to look for hysteretic effects in the measurements. Additionally, at each acceleration setting, multiple samples (thirteen) were taken in order to examine the repeatability of the measurement at a particular acceleration amplitude. The wave speed and attenuation data were plotted as the mean of these thirteen samples with the standard deviation also shown.

For continuous excitation of the piston in the presence of vertical agitation of the bed additional steps were taken. The detected signals were composed of components from both the shaking and the wave input. By keeping the agitation frequency, typically 20 Hz, an order of magnitude lower than that of the wave input, typically 500 Hz, high-pass filtering could be done to isolate the input wave signal. The methods of the unagitated experiments could then be employed to calculate the
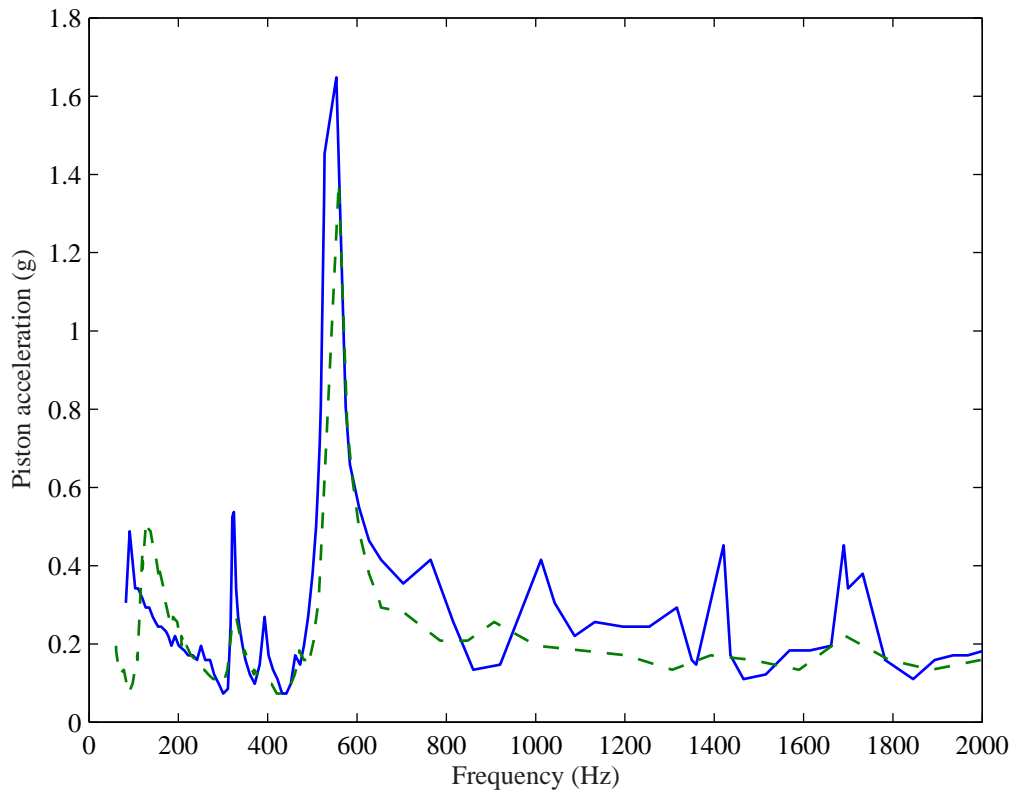
Figure 2.2: Acceleration of the piston for a constant voltage input in air (solid) and in a granular bed (dashed).

wave speeds and attenuation through the agitated bed.

2.1.2 Pulsed input

A pulsed movement of the piston allows for a discrete disturbance to be created in the bed. Since the excitation is of finite duration, the full lifetime of this wave energy can be observed without the complications of continuous energy input. Thus, the existence of wave reflections can be determined. Additionally, such excitation is comparable to the methods used by others (Nesterenko, 2001; Coste *et al.*, 1997) who have examined the nonlinear characteristics of 1-D particle chains.

Pulses were sent to the shaker from a pulse generator with independent control of the pulse width and amplitude. The pulses were sent at intervals which allowed all oscillations from the previous pulse to damp out before the following pulse was created. The pulse width was varied between 1 and 100 ms and the amplitude was varied from 0-1 V. Due to the complex interaction of the piston with the granular bed, this electrical input to the pulse generator is not overly meaningful. For this reason, the true input to the bed was judged from the characteristics of the wave at the near transducer. The relationship between the input amplitude voltage and the near transducer pressure amplitude can be seen in Figure 4.10.

Pulses were square in shape, fully positive in displacement, and returned to zero displacement at the end of each pulse. Pulses resulted in a wave that was detected at the two transducers as it traversed the bed. The speed of the wave was measured by finding the difference in the arrival times at the two transducers. Defining the arrival of the wave as the point at which the pressure first deviates from the background pressure level (see Figure 4.1) was found to produce the most consistent results. As in the continuous excitation experiments, the attenuation through the bed was found by comparing the amplitudes of the signals measured by each transducer.

For pulsed waves in an agitated bed, as in the continuous excitation experiments, the signals were a combination of the shaking and the input wave. In this case, the repeatability of the signal due to shaking alone was used to subtract out its effect. A given signal is shifted by one period of the shaking and then subtracted from the original signal as described in more detail in Section 7.3. This approach appears to work well in reducing the signals with agitation to something very similar to the unagitated experiments.

2.2 Simulations

The simulations use a soft-particle, Discrete Element Method (DEM) similar to others applied to granular flows (Cundall and Strack, 1979). The program tracks a specified number of discrete elements (particles), advancing each by integrating the equations of motion. At any instant in time, the entire state of each particle is known. The particles are soft in the sense that collisions between

particles (and between particles and the walls) have a non-zero collision time. This is in contrast to hard-sphere models (Campbell and Brennen, 1985) in which collisions are binary and instantaneous, with resulting velocities determined by a coefficient of restitution. Soft-particle methods require a contact model to describe the forces throughout the collision process. The contact model used is described below in Section 2.2.1.
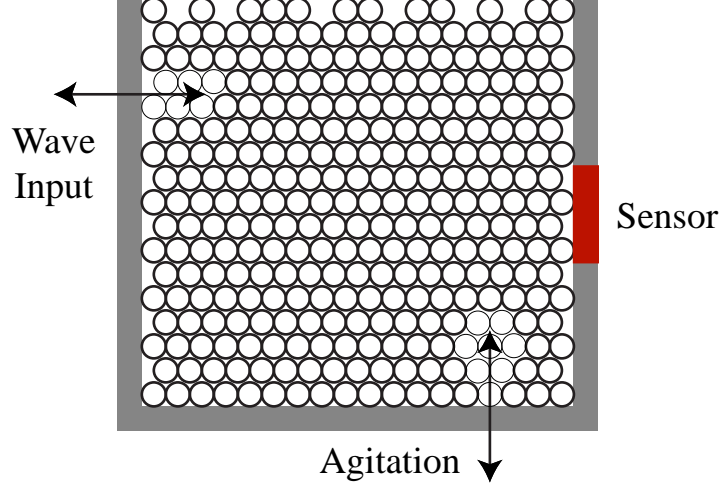
Figure 2.3: Schematic of the simulation cell.

The simulation is two-dimensional with spherical particles. The particles are three-dimensional for the purposes of calculating their masses and moments of inertia, but they are confined to move in a two-dimensional plane. The particles are free to translate in two directions and to rotate about an axis normal to this motion. The simulation setup is shown schematically in Figure 2.3. The particles are confined between three walls. The left wall is moved, either in a sinusoidal or pulsed manner, to initiate a wave in the bed. For sinusoidal motion, the frequency and maximum displacement of the piston are specified. The pulsed input consists of constant positive acceleration followed by a constant, negative acceleration of the same magnitude. This piston motion is shown in Figure 2.4. The pulse width, T_p, and the maximum velocity, v_{max}, are specified leading to a pulse with net displacement, d_{max}. This pulse shape was chosen so that no infinite accelerations were sent into the system. The lower boundary of the simulation cell can also be moved (sinusoidally) to simulate vertical shaking of the bed.

Waves are detected in the bed with simulated pressure transducers. By summing particle forces on the right wall over some specified area, a pressure is defined. One such detector is depicted on the right wall of Figure 2.3, but any number of sensors could be defined on any wall of the cell. Further, since the states of all particles are known, the wave can be visualized as the transmission of forces between particles in the bed.

Two additional steps are taken to better match the conditions of the simulations with those
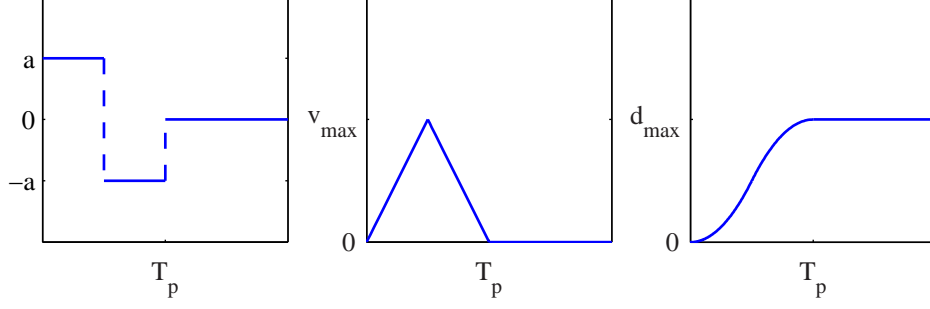
Figure 2.4: Pulsed motion of the piston in simulations. Shown are the acceleration (left), velocity (center), and displacement (right) of the piston.

of the experiments and real granular materials. The particles are polydisperse. That is, they are given some random variation of particle diameter about a specified mean value. The dispersity, D', is given as a percentage of the mean particle diameter around which the particle diameters are randomly distributed. This variation mimics real granular materials. The dependence of the results to changes in the polydispersity is not examined in the current study and the dispersity is set to 10% for all simulations. Sensitivity of the results to the degree of dispersity may be of interest for future study. The geometric packing of a granular bed is also marked by irregularity. The initialization of the simulation attempted to capture this irregularity. The particles start in a regular grid, well separated in both directions. They are given random initial velocities and allowed to settle under the effect of gravity. The wave disturbances are introduced at the left wall only after the settling of the bed has ended. This procedure creates a unique bed for each simulation.

2.2.1 Contact model

The contact model determines the forces between any two contacting particles. The model does not explicitly calculate the deformation of the bodies in contact, but merely determines the forces as if they were deforming. The model is shown schematically in Figure 2.5.

The force in the normal direction, F_n, is a combination of a force due to elastic, conservative particle interaction, F_{elas}, and a force due to dissipative effects, F_{vis}. The force due to the elastic deformation of spheres in contact is given by Hertz's theory (Johnson, 1987) as

$$F_{elas} = K_2 \delta^{3/2}, \tag{2.2}$$

where δ is the particle overlap and K_2 is a material constant. This nonlinear relationship between the elastic force and the particle deformation is the major change in the contact model from that used by Wassgren (1997) whose elastic force depended linearly on the deformation ($F_{elas} = k_n \delta$). Since one goal of the present investigation is to observe nonlinear wave effects, the current nonlinear
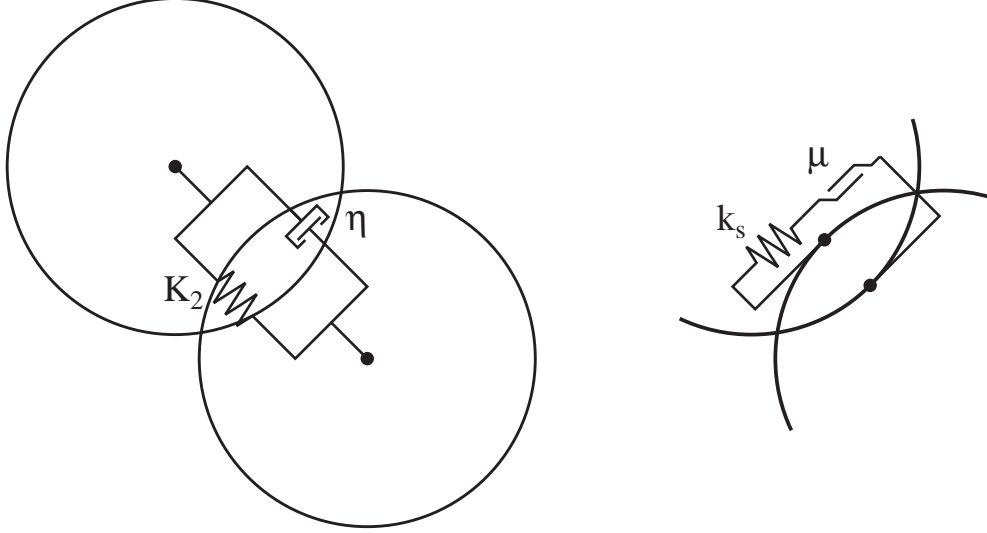
Figure 2.5: Contact model in the normal (left) and tangential (right) directions.

interaction given by Equation 2.2 is preferable to the linear interaction. The prefactor, K_2, is based on the material properties of the colliding bodies and is given by Hertz's theory as

$$K_2 = \frac{2}{3}\frac{E}{1-\nu^2}R_{eff}^{1/2},$$

(2.3)

where E is Young's modulus of elasticity, ν is Poisson's ratio, and $R_{eff} = \frac{R_1 R_2}{R_1+R_2}$ is the effective radius of the colliding bodies of radii R_1 and R_2. The expression for K_2, Equation 2.3, assumes that the colliding bodies are composed of the same material. The generalization to the collision of dissimilar bodies is possible, but is not pertinent here. Additionally, for purposes of calculating these interaction constants, we assume that $R_1 = R_2 = R$ for collisions between particles. Thus $R_{eff} = R/2$ for particle/particle collisions and $R_{eff} = R$ for particle/wall collisions.

Dissipation occurs in all real granular material interactions. Dissipation in the simulated system is introduced through a viscous force in the normal direction as was done in the viscoelastic model of Brilliantov *et al.* (1996). This force is derived through a quasistatic analysis as done in Hertz's theory for the elastic force. It is proportional to the deformation rate and given by

$$F_{vis} = \eta\delta^{1/2}\dot{\delta},$$

(2.4)

where $\dot{\delta}$ is the rate of change of the overlap with time and η is a material constant. For the linear spring and dashpot used by Wassgren (1997), the dissipative force was linearly related to the deformation rate alone. Here, the deformation also factors into the dissipative force. The linear modeling leads to a direct relationship between the dashpot coefficient and a constant coefficient of restitution. In this nonlinear normal contact model, this direct relationship is not possible and the

coefficient of restitution varies with the initial incident velocity of the colliding particles.

Material property effects for the dissipative force are characterized by the factor η, which is given by Brilliantov *et al.* (1996) as

$$\eta = \frac{E}{1 - \nu^2} R_{eff}^{1/2} A. \tag{2.5}$$

As with the prefactor, K_2, η depends on the modulus of elasticity, Poisson's ratio, and the effective radius between incident particles. Also included here is a dissipation factor, A, which is composed of the viscous constants, η_1 and η_2, for the bulk material and the other material properties, E and ν, and has the functional form

$$A = \frac{1}{3} \frac{(3\eta_2 - \eta_1)^2}{(3\eta_2 + 2\eta_1)} \left[\frac{(1 - \nu^2)(1 - 2\nu)}{E\nu^2} \right]. \tag{2.6}$$

Since the viscous constants for the materials under consideration are not known, A is used as a fitting parameter. It is determined by running baseline simulations where a single particle is dropped from a given height to find the coefficient of restitution as a function of A. A is then chosen to yield a reasonable range of coefficients of restitution. It may also be possible to fit A to measured wave attenuation rates from experiments.

Some care must be taken when applying Hertz's law to granular flows. The force-displacement relationship was originally derived for the static interaction of bodies, so for dynamic situations, such as granular flows, one must verify that collisions obey quasi-static assumptions. Since the viscous force was derived under the same assumptions, its validity also depends on these assumptions holding. The conditions necessary for the quasi-static assumption to apply to particles in dynamic contact are listed by Nesterenko (2001) as:

- The maximum shear stresses achieved in the vicinity of the contact must be less than the elastic limit.

- The size of the contact surfaces must be much smaller than the radius of curvature of each particle.

- The characteristic times of the particle interaction, τ, must be much longer than the oscillation period, T_o, of the elastic sphere. Specifically,

$$\tau \gg T_o \approx 2.5 \frac{R}{c_0}, \tag{2.7}$$

where c_0 is the speed of the sound in the particle material. The validity of this condition in the simulations will be discussed using the dimensionless form of this expression in Section 2.2.2.

The contact model in the tangential direction, shown on the right in Figure 2.5, allows for both the effect of elastic loading in this direction and the possibility of frictional sliding between the particles. The linear spring, k_s, loads until the static friction force, μF_n, is reached where μ is the

coefficient of friction and F_n is the total normal force. Beyond this point, the force is just this friction force value as the particles slide over each other. The model is identical to that used by Wassgren (1997), where it is described in more detail.

A difficulty arises in choosing the values for the tangential model parameters, k_s and μ. For the fully linear model, k_s is just some fraction of the normal spring constant, k_N; according to Cundall and Strack (1979) somewhere between 2/3 and 1 times k_n. For the nonlinear normal model, the nonlinear spring in the normal direction needs to be related to the linear spring in the tangential direction. This is accomplished by linearizing the nonlinear spring about a typical force, F_{typ}, equal to the weight of the particles above the half-height of the bed. Specifically,

$$F_{typ} = \frac{N\bar{m}g}{2W^*}. \tag{2.8}$$

Here, N is the total number of particles, W^* is the ratio of the width of the simulation cell to the particle diameter, and $\bar{m}$ is the average mass of a particle. This linearization leads to an effective linearized normal spring constant from which the tangential linear spring, k_s, is then calculated. The value used for μ is the same as that used by Wassgren (1997), $\mu = 0.1$ for both particle-particle and particle-wall collisions.

The simulation time step, Δt, was chosen to ensure accurate integration and to fully resolve all collisions. In addition to the translational and rotational periods calculated by Wassgren (1997), the Hertzian contact time (Goldsmith, 1960) is also calculated in the current study as

$$\tau_H = \frac{2.9432}{v_0^{1/5}} \left[\frac{5}{4K_1 K_2} \right]^{2/5}. \tag{2.9}$$

Here, $K_1 = \frac{m_1 + m_2}{m_1 m_2}$ is the effective mass between the colliding particles of individual masses m_1 and m_2 and K_2 is the elastic prefactor as defined in Equation 2.3. The maximum velocity in the system defines the minimum contact time. Examining the contact time, the translational period, and the rotational period, the shortest time is found and the simulation time step is set to one-tenth of this time.

2.2.2 Dimensionless parameters

The simulation variables are made dimensionless by the average particle mass, $\bar{m}$, the average particle diameter, $\bar{D}$, and the speed of sound, $c_0 = \sqrt{\frac{E}{\rho}}$, in the bulk of the material of which the particles and walls are comprised. Clearly, $\bar{m}$ and $\bar{D}$ define a characteristic mass and length, respectively, for the system. The combination of the sound speed and the average particle diameter, $\frac{\bar{D}}{c_0}$, defines a characteristic time that corresponds to the time required for a wave to travel through a single particle.

This scaling leads to some interesting results for the parameters in the contact model. In the normal direction, the expressions for K_2 and η (denoting the dimensionless values by K_2^* and η^*) are significantly simplified. These expressions are

$$K_2^* = \frac{\bar{D}^{5/2} K_2}{\bar{m} c_0^2} = \frac{4}{\pi (1 - \nu^2)} R_{eff}^{*1/2} \tag{2.10}$$

and

$$\eta^* = \frac{\bar{D}^{3/2} \eta}{\bar{m} c_0} = \frac{6}{\pi (1 - \nu^2)} R_{eff}^{*1/2} A^*. \tag{2.11}$$

R_{eff}^* in both expressions is a constant depending on the type of contact. It is equal to $1/2$ for the collision of particles and $1/4$ for the collision of a particle on a wall. Written this way, the nonlinear spring constant, K_2^*, is only a function of Poisson's ratio, ν. If one assumes that the majority of the energy from an incident plane wave is transmitted through this force link, one would also expect the wave speed to depend on only Poisson's ratio. The prefactor, η^*, in the dissipative normal force depends on the dimensionless dissipation factor, A^* ($= \frac{c_0}{\bar{D}} A$), as well as Poisson's ratio. The attenuation through the bed will likely depend strongly on this dissipative factor so one would expect the attenuation rate to be a function of only ν and A^* given this scaling.

The surprising result of this scaling is the lack of dependence of the dimensionless results on, mostly notably, the particle diameter. Thus, the scaling suggests that the wave speed should be independent of particle diameter.

Now, returning to the validity of the quasi-static assumption, the third condition, equation Equation 2.7, can be written in dimensionless form as

$$\tau^* = \frac{c_0 \tau}{\bar{D}} \gg T_o^* = \frac{c_0 T_o}{\bar{D}} \approx 1.25. \tag{2.12}$$

Thus, the characteristic times of the simulation, the width of the input pulse (T_s) or the period of sinusoidal excitation (T_p), should be kept well above 1.25. The smallest period for sinusoidal excitation ($T_s = 770$) was nearly three orders of magnitude larger so the assumption certainly held for these simulations. In contrast, the smallest pulse width ($T_p = 8$) was less than a factor of ten larger than minimum time scale at which the quasi-static assumptions are valid. No adverse effects were observed in this low limit of the pulse width. The largest pulse width was $T_p = 800$, a value well within the valid range for the assumptions. Smooth trends in measured quantities continued from this maximal value down to the lowest widths.

The scaling in the tangential direction is more involved, mostly due to the manner in which the tangential spring constant, k_s, is calculated. The linearization of the nonlinear normal force leads to additional terms related to the linearization. The dimensionless effective linear spring in the normal

N	4000
W*	50
ν	0.1
D'	10 %
$\frac{k_s^*}{k_n^*}$	0.1
A^*	0.7
Fr	1.74×10^{-9}
Δt	2.94

Table 2.2: Parameter values used in the simulations.

direction becomes

$$k_n^* = \frac{\bar{D}^2 k_n}{\bar{m} c_0} = K_2^{*2/3} F_{typ}^{*\,1/3} = \left[\frac{4}{\pi\left(1-\nu^2\right)} R_{eff}^{*1/2} \right]^{2/3} \left[\frac{N^* Fr}{2} \right]^{1/3}. \qquad (2.13)$$

In addition to a nonlinear dependence on K_2^*, the effective linear spring constant depends on the depth of the bed in particle diameters, $N^* = N/W^*$, and the Froude number, $Fr = \frac{g\bar{D}}{c_0^2}$. Both N^* and Fr are the same for all simulations presented here. The dimensionless, tangential spring constant, k_s^*, is some fraction of this value. For all simulations run, this fraction was set to 1 for particle-particle collisions and 0.1 for particle-wall collisions consistent with Wassgren (1997).

The values of the parameters used in the simulations are shown in Table 2.2.

2.2.3 Preliminary results

This section discusses some simulation results that are indirectly related to the propagation of elastic waves in a granular bed. First, some interesting observations of concentration waves that are evident in the initialization procedure of the simulations will be presented. Then the focus turns to the static distribution of pressure that results from the geometric configuration of the bed after initialization and settling. These results show that the simulations are capable of capturing phenomena that are seen in real granular materials and granular flows.

2.2.3.1 Settling

The initialization of the granular bed in the simulations allows the particles to settle under the effect of gravity. As the particles find their resting place in the bed, a concentration wave forms and propagates from the base of the bed to the free surface that eventually forms at the top of the bed. The arrival of the wave corresponds to a local increase in the solids fraction of the bed.

Figure 2.6 shows the passage of this concentration wave in terms of the local pressure. There is a large peak in the pressure as the wave arrives at each of the sensors. The difference in the arrival time at each of the sensors defines a speed for this wave. In the case shown in Figure 2.6, the speed of the concentration wave is 4.9×10^{-4} in dimensionless velocity units. This speed is one hundred

times slower than the elastic waves that travel through particle contacts.

Before the arrival of the wave, there are smaller pressure spikes that correspond to the collisions of individual particles with the sensing surface. After these collisional events, the pressure returns to zero. Once the concentration wave has passed, the pressure takes a stable value dictated by the geometrical configuration of the bed. The pressure scaling with depth for a series of different initializations of the simulation bed is discussed below.

The arrival of the concentration wave at the free surface of the bed leads to another interesting observation. Visualizations of the simulated bed show that a few particles are ejected from the surface layer upon arrival of the wave. Such saltation is commonly observed at the surface of real shaken granular beds.
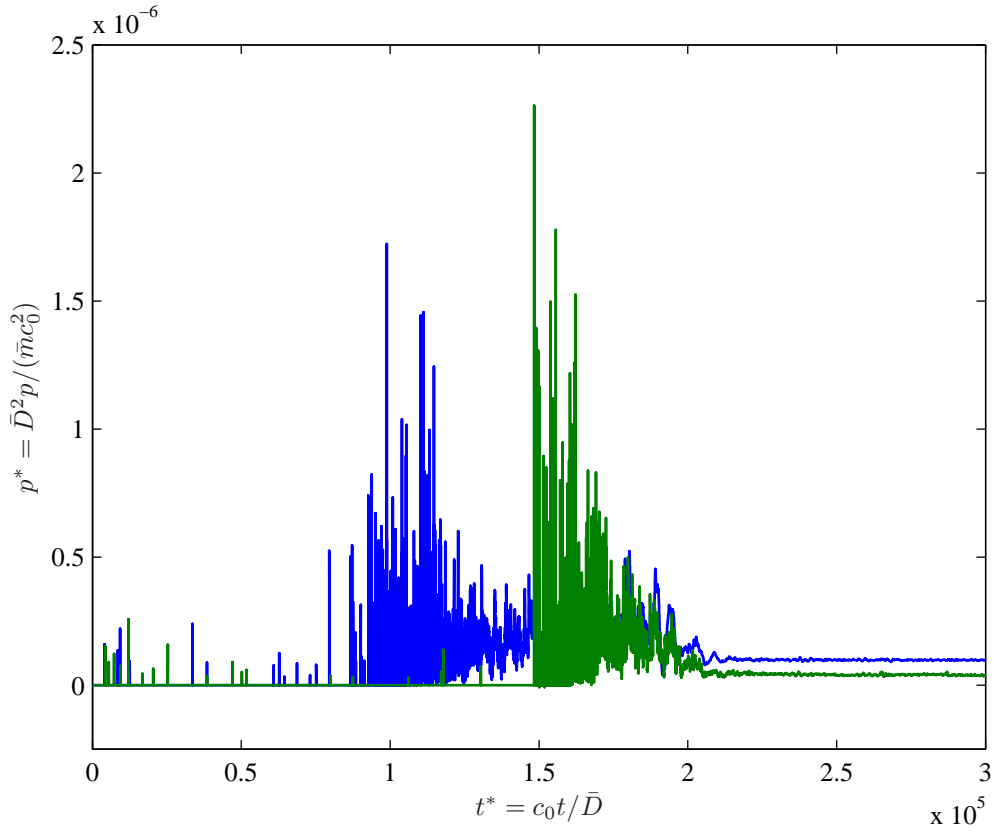
Figure 2.6: Pressure signals from detectors at 0.2 (first pressure disturbance) and 0.5 (second pressure disturbance) of the domain height from the bottom of the simulation cell.

2.2.3.2 Pressure scaling with depth

The value of the static pressure after the settling phase of the simulations is shown in Figure 2.7. The results represent a large number of initializations of the bed. As expected, the simulations predict a linear variation of the pressure with depth. This dependence only holds in an averaged

sense. As shown by the error bars, there can be a large degree of variation in the pressure value for any one particular initialization of the simulated bed. The scatter in the data increases with depth. The variation in the static pressure is a consequence of the heterogeneous nature of the granular bed. At greater depth, there is the possibility of increased configurational complexity as there are more particles and more particle contacts before the point of the measurement.

For real granular materials, such a linear (hydrostatic) increase in the pressure would only hold to a particular depth. At a critical depth, typically around the width of the container, the side walls would frictionally support the additional weight of particles and the pressure would become constant. The simulations do not display this behavior, at least at the depths tests. The measurement at greater depth ($z^* = 50$) corresponds to the expected critical depth, but the pressure continues to increase. This inconsistency with the expected pressure dependence hints at some error in the modeling of friction in the simulations.
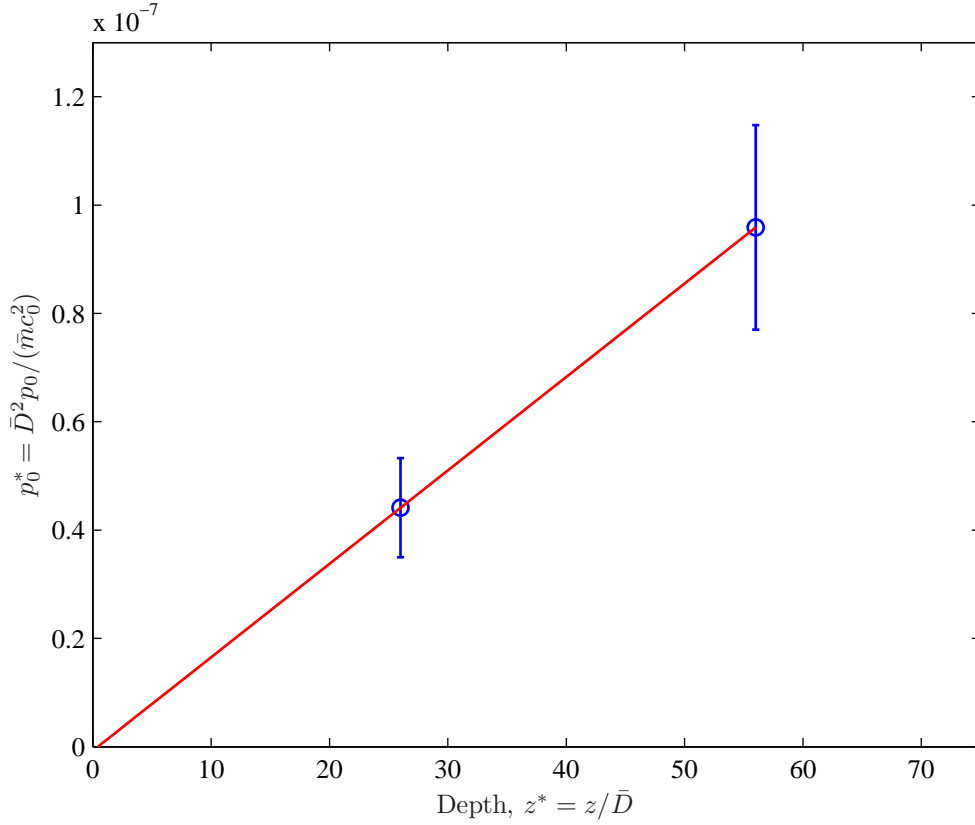
Figure 2.7: Static pressure with depth from the free surface in the granular bed. Each data point is averaged over 240 different initializations of the simulation cell. The standard deviation is shown by the error bars.

Chapter 3

Experiments with continuous input

In this chapter, the results of experiments in which sinusoidal waves were continuously input into the granular bed via the piston will be discussed. Such continuous excitation provides two main advantages over the pulsed input. First, the disturbances in these experiments are of a fixed, known frequency. A pulse will be a summation of a variety of frequency components. By testing over a range of frequencies, the dependence of the wave speed on the frequency can be found. Such information can provide insight into the dispersity of the granular bed. Secondly, since the applied force at the piston is constantly changing, temporal variation of the bed can be probed. Such studies are particularly useful for the shaken granular bed experiments as the state of the bed can vary from one instant of the shaking period to another, but transient effects are seen also in static experiments. Results from agitated bed experiments are presented in Section 7.1.

Here, the behavior of a sinusoidal input into an unagitated granular bed is described. In the first section, results will be presented for experiments performed at a constant piston acceleration amplitude. Such studies will establish the dispersion relation for the granular bed. Later, the results for constant frequency experiments will show the role of bed rearrangement in the variation of wave propagation characteristics of the granular bed. For an unagitated granular bed, the geometric framework through which the waves travel is fragile and is susceptible to rearrangement from disturbances as weak as the input pressure waves (Liu and Nagel, 1993).

3.1 Constant acceleration experiments

Figure 3.1 is a typical result of the present experiments and demonstrates the nondispersive characteristics of wave propagation in a static granular bed as previously described by Liu and Nagel (1994). As shown in Section 1.2.3.1, nondispersive wave propagation implies a linear relationship between phase and frequency. The trend in Figure 3.1 is, on average, linear with irregular deviations about this trend. Measurements were made at two different input acceleration amplitudes. Both amplitudes were tested at a given frequency before incrementing the frequency value. The
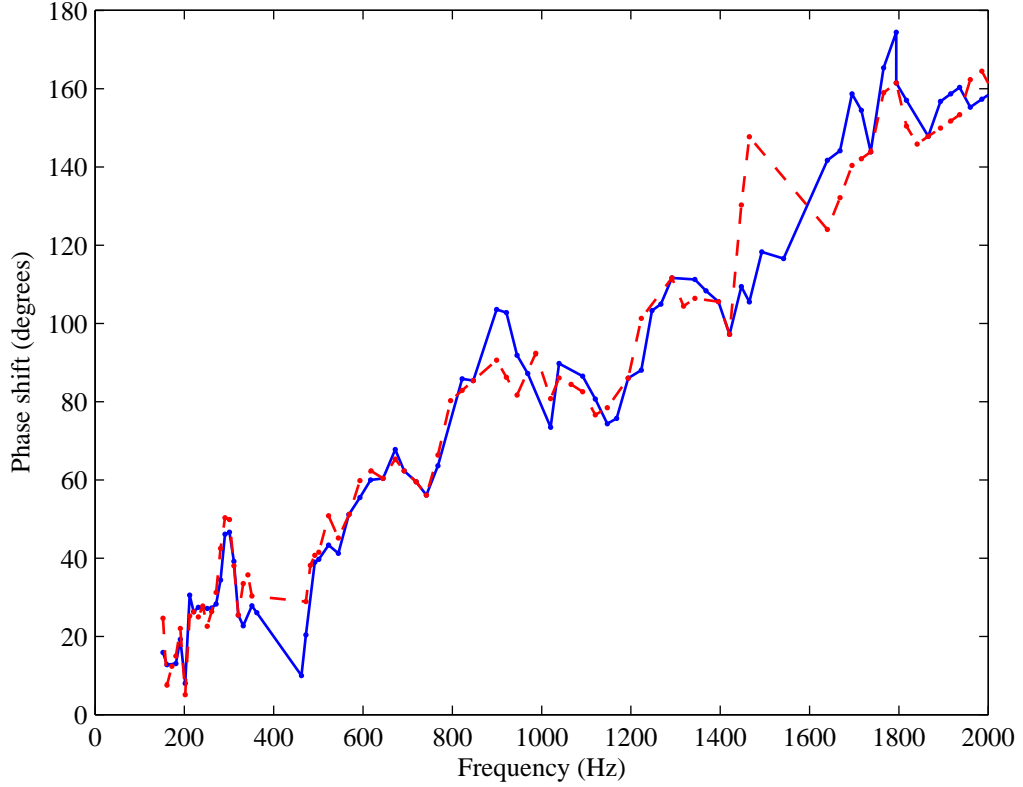
Figure 3.1: Phase shift between signals at the near and far transducer (40 mm spacing) in 4 mm glass beads. The frequency range is swept at constant acceleration values of 0.20g (solid) and 0.30g (dashed).

alternative would be to sweep the entire frequency range at one acceleration amplitude level and then resweep the range at the other value. As is seen in Figure Figure 3.1 and confirmed by examining other similar plots for different conditions, this change in amplitude has little effect, at least with the testing procedure used. One would expect greater variation between the two acceleration amplitudes if the frequency range were swept in two passes. Particle rearrangement in the course of the first frequency pass would likely affect the results of the second pass. With the procedure used, any particle rearrangement occurs before the frequency is incremented and affects the values for the measurements at both amplitude levels for the next frequency. Both the linear trend of the plots and the minimal variation with amplitude are consistent over all particles sizes and materials examined.

The deviations from the linear trend are especially large at the lower frequencies, in the range of 300-500 Hz. These large deviations can be seen in Figure 3.1, but are particularly apparent when this data is plotted as a phase speed in Figure 3.2. Plotting in this way also emphasizes the nondispersive nature of the granular bed. The phase speed is not a function of the frequency. The significant fluctuations at low frequency are attributed to the natural frequencies in the system.
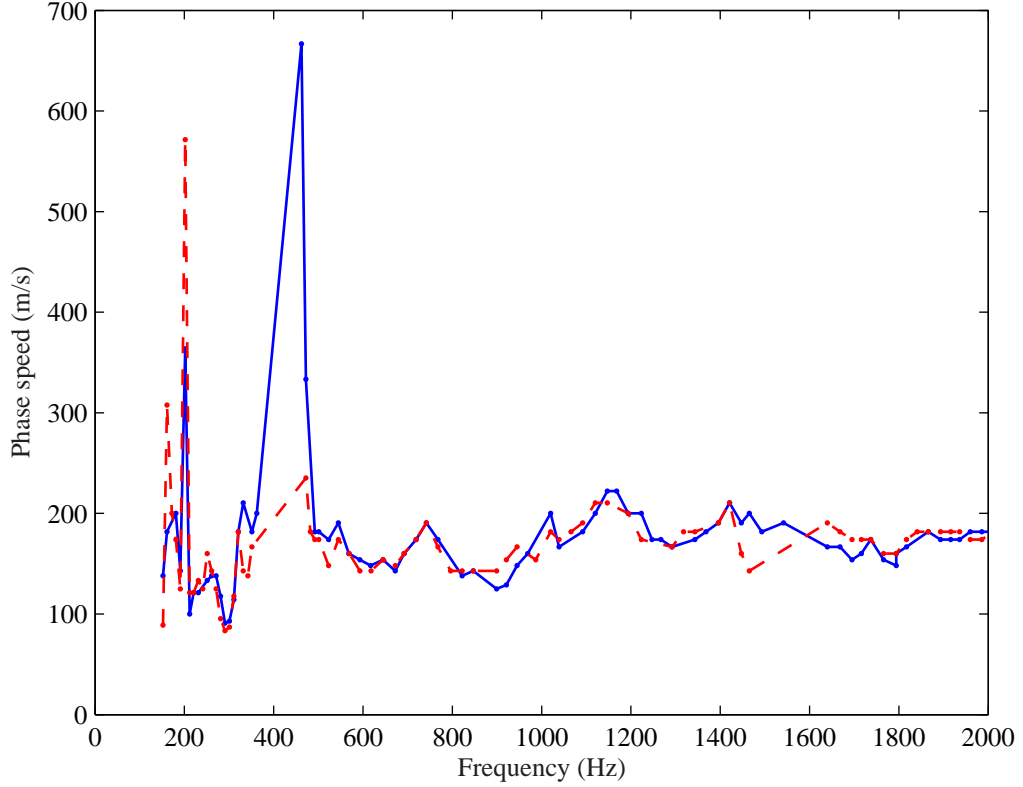
Figure 3.2: Phase speed measured at constant acceleration values of 0.20g (solid) and 0.30g (dashed) in 4 mm glass beads at a spacing of 40 mm.

The natural frequency of the box in the direction of wave propagation (based on calculated wave speeds in glass beads) is 325 Hz. Additional resonant frequencies exist in the dynamics of the wave source. The natural frequencies of the piston and rod connecting it to the shaker have been measured (with an impact hammer) to be 300 Hz. By holding the rod, the natural frequency of the piston alone was found to be 400 Hz. The largest peak in the phase speed is near 400 Hz and there is a sharp minimum around 300 Hz. The peaks around 200 Hz do not agree with any of these calculated frequencies, but are probably due to some additional resonance. Consequently, the large fluctuations of the phase speed in the low frequency range agree well with the resonant frequencies of the system. The deviations at the higher frequencies were found to be dependant on the geometrical packing of the bed. They were not repeatable between experiments and tended to smooth out when averaged over multiple realizations of the same experimental conditions. Thus, the higher frequency deviations are deemed to be an artifact of the bed microstructure and possibly a sign of localized dispersion. Despite this, the system is still considered to be nondispersive in a general sense since these deviations average out over multiple experiments.

Examination of the phase speed also reveals another trend. Neglecting the large spikes in the phase speed, the average of the speed at low frequency (< 500 Hz) appears to be lower than that

measured at larger frequencies. This trend is confirmed by closer inspection of the plot of the phase shift (Figure 3.1). The slope of the phase with frequency does appear to be shallower for values of frequency below 500 Hz.
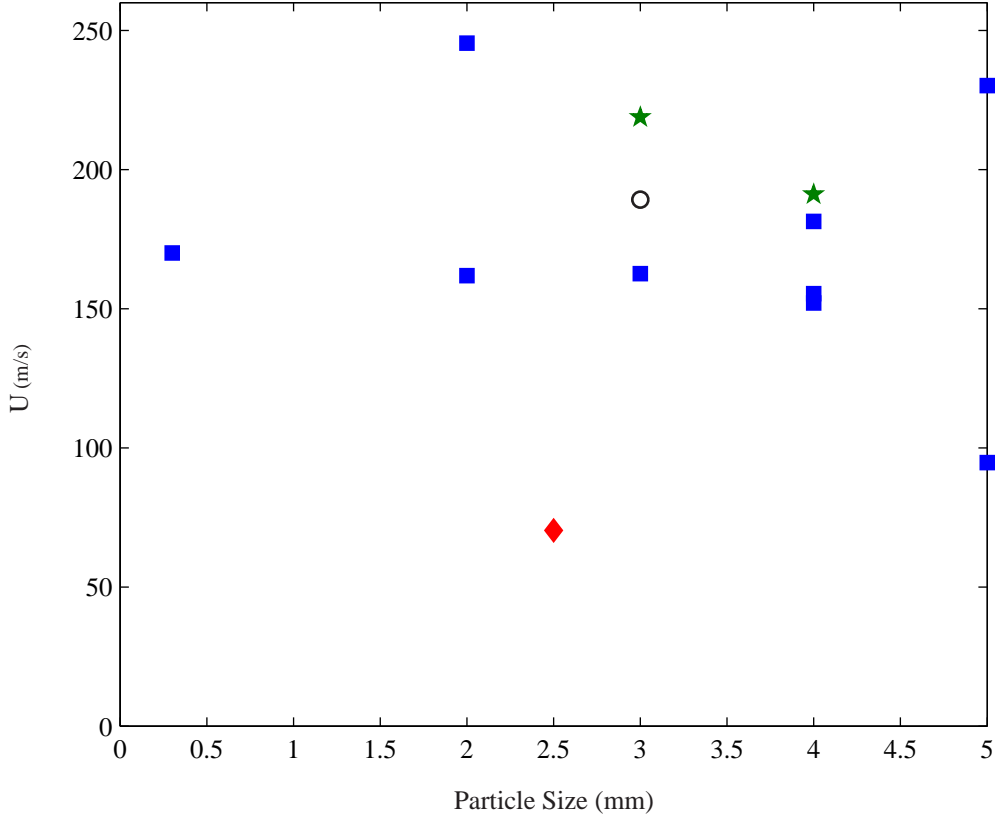
Figure 3.3: Summary of the group velocity as a function of particle size. Data shown for PVC cylinders (♦) and glass spheres: unconsolidated (■), increased overburden (○), and consolidated (★).

Since wave propagation in the granular bed appears to be nondispersive, the group velocity, as defined in Equation 1.5, was evaluated and compared for different materials and conditions. For each experiment, a straight line was fit to the data and this slope was used to calculate the group velocity. The group velocity values for the different acceleration amplitudes were averaged. The results from the constant acceleration experiments are summarized in Figure 3.3 for a variety of experimental conditions. The general trend is that particle size does not affect the group velocity. For the glass particles, the group velocity is 170 m/s for nearly all particle diameters. The exceptions are the point at 250 m/s which can be attributed to a poor curve fit and the data points at the largest particle sizes where there is significant spread in the group velocity measurements. To measure the wave speed accurately, averaging must be done over multiple force chains. As the particle size increases relative to the fixed size of the transducer face, this averaging procedure begins to fail since few particles and few force chains are in contact with the transducer face. Specifically, the

coherence of the averaging begins to break down for 4 mm particles and by 5 mm the accuracy of the measurement is severely reduced.

The strongest influence on the group velocity is the material composition of the particles, characterized by the speed of sound in the bulk material, $c_0 = \sqrt{E/\rho}$, where E is Young's modulus and ρ is the density. The measured group velocity in the PVC cylinders is less than half that measured in the glass particles. A large difference is expected as the sound speed in bulk PVC is a third of the value of the sound speed in bulk glass. One might expect that scaling the group velocity by the bulk sound speed would collapse the data, but simulations have also shown a strong dimensional dependence of the wave speed on Poisson's ratio (see Section 6.2.1). It appears that a proper scaling of the group velocity should include both the bulk sound speed and Poisson's ratio.

Consolidation and an increase in the overburden have a smaller effect on the group velocity as exemplified in Figure 3.3. Consolidation increases the solids fraction and the effective stiffness of the granular bed. Increasing the amount of material above the point of measurement increases the local pressure at which the speed is measured. An increase in the wave speed is expected and measured from both effects.
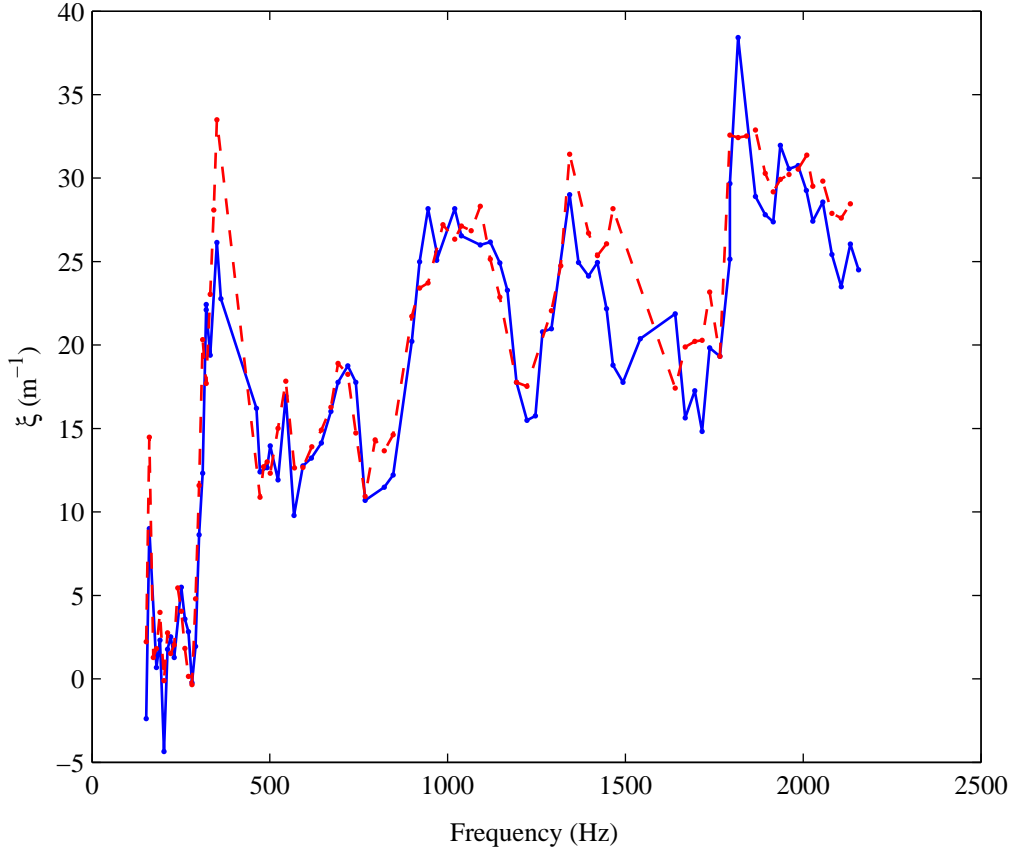
Figure 3.4: Attenuation ratio between the near and far transducers in 4 mm glass beads. The frequency range is swept at constant acceleration values of 0.20g (solid) and 0.30g (dashed).

For the phase (and phase speed) some variation was observed about the linear (constant) trend. Measurements of the attenuation in a static granular bed show even greater irregularity. The variation of the attenuation ratio, ξ (defined in Equation 2.1), with frequency is shown in Figure 3.4 for the same experiments displayed in Figure 3.1. Even over very small frequency changes, the attenuation ratio can vary by a factor of nearly three. Sharp fluctuations in the attenuation ratio are seen over the entire range of experimental conditions. The increase in the attenuation ratio with frequency, as seen in Figure 3.4, is observed over all conditions. Such an increase is expected, as higher frequency disturbances should decay more quickly than lower frequency disturbances.

There also appears to be slight demarcation between the behavior at low frequencies and that at higher frequencies as was seen in the phase and phase speed. Neglecting the larger peaks that may result from resonances, the attenuation ratio at frequencies less than 500 Hz increases more gradually and the variation is more muted than at frequencies above 500 Hz.
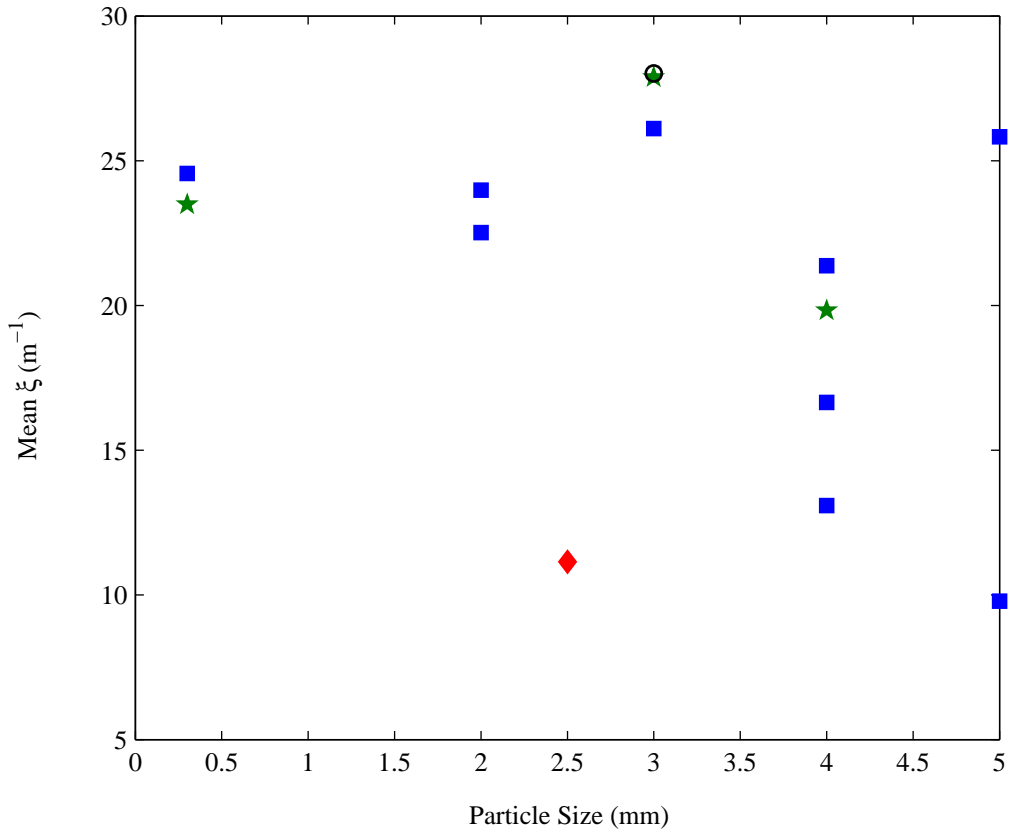
Figure 3.5: Summary of the attenuation ratio plotted as the average of the ratio over all frequencies as a function of particle size. Data shown for PVC cylinders (♦) and glass spheres: unconsolidated (■), increased overburden (○), and consolidated (★).

The increasing trend in the attenuation data with frequency leads to some difficulty in comparing results between different experimental conditions. Despite the irregularity and the trend of the data,

an average over all frequencies is taken for each experimental condition. Though this approach may appear rather coarse, it is sufficient to indicate trends. Figure 3.5 summarizes the attenuation data based on the mean.

Some of the dependencies are similar to those seen for the group velocity data. Again, the different sizes of glass particles yield nearly the same attenuation (around 25 m^{-1}) for all but the larger particle sizes. Glass particles of diameter 4 and 5 mm produce divergent and scattered results. These scattered results are again likely due to deficiencies in the averaging over different wave paths as the particle size to sensor area ratio increases. Consolidation does not lead to any consistent trend in the attenuation. For the smallest particles, consolidation decreases the attenuation, but for the 3 mm particles the opposite is true. Increased overburden also increases the attenuation for the 3 mm particles, but this one point is not nearly sufficient to draw any general conclusions about the role of increased pressure on the attenuation. Through the lighter, softer PVC the attenuation is over half that of the glass. This result is counter-intuitive and contrary to what was observed for pulsed waves (see Figure 4.2).

3.2   Constant frequency experiments

Constant frequency experiments provide some insight into the role that bed rearrangement has on wave propagation. The experiments were performed by beginning at low amplitude then raising the amplitude and then lowering it. Figure 3.6 shows the effect of rearrangement by comparing an initially unconsolidated bed, where relative particle motion is more likely due to the residual potential energy in the system, and a consolidated bed where motion is less likely. For the unconsolidated case, the measured phase speed takes different values on the increasing and decreasing path of input acceleration. Near the middle of the acceleration range, the difference is quite significant, as much 100 m/s. This discrepancy can be attributed to particle rearrangement in the granular bed. The act of passing pressure waves of increasing amplitude through the bed breaks and reforms the particle chains that serve as wave paths. In contrast, the consolidated case gives nearly the same speeds in both directions. Up to a shaking acceleration amplitude of 0.22g, the phase speed increases. Beyond this amplitude, the phase speed decreases slightly. The same phase speed measurements are reproduced as the acceleration amplitude is reduced.

Further evidence of particle rearrangement can be seen in the scatter of the data. The scatter for the unconsolidated case is generally much larger than that for the consolidated case. The particles in the consolidated case have limited mobility due to the denser state of their bed so there is minimal distortion of the force chains and the measurements are quite consistent even at the larger values of the acceleration amplitude. In contrast, the scatter for the unconsolidated bed increases with piston acceleration amplitude. One would expect a larger force input at the piston to disturb additional
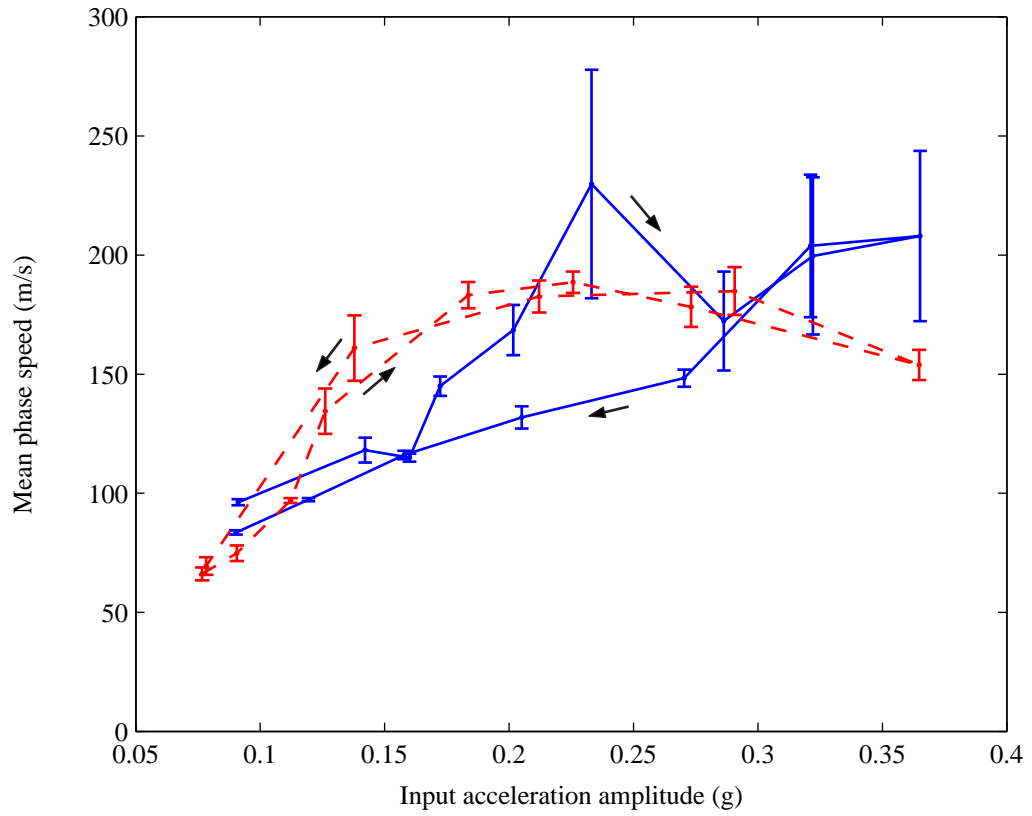
Figure 3.6: Mean phase speed for an unconsolidated bed (solid) and a consolidated bed (dashed) of 4 mm glass beads as the amplitude of the input wave is increased and then decreased.

force chains and increase the variability of the data. An increased number of effected chains leads to a greater range of values in the phase speed measurement. Despite the irregularity in the phase speed as the input acceleration is increased, some repeatability does exist at the largest values. Above an acceleration amplitude of 0.3g, the phase speed in the unconsolidated bed takes a consistent value on both the increasing and decreasing path of the piston amplitude. This hints at some, at least local, uniformity of the state near the piston as the agitation becomes greater.
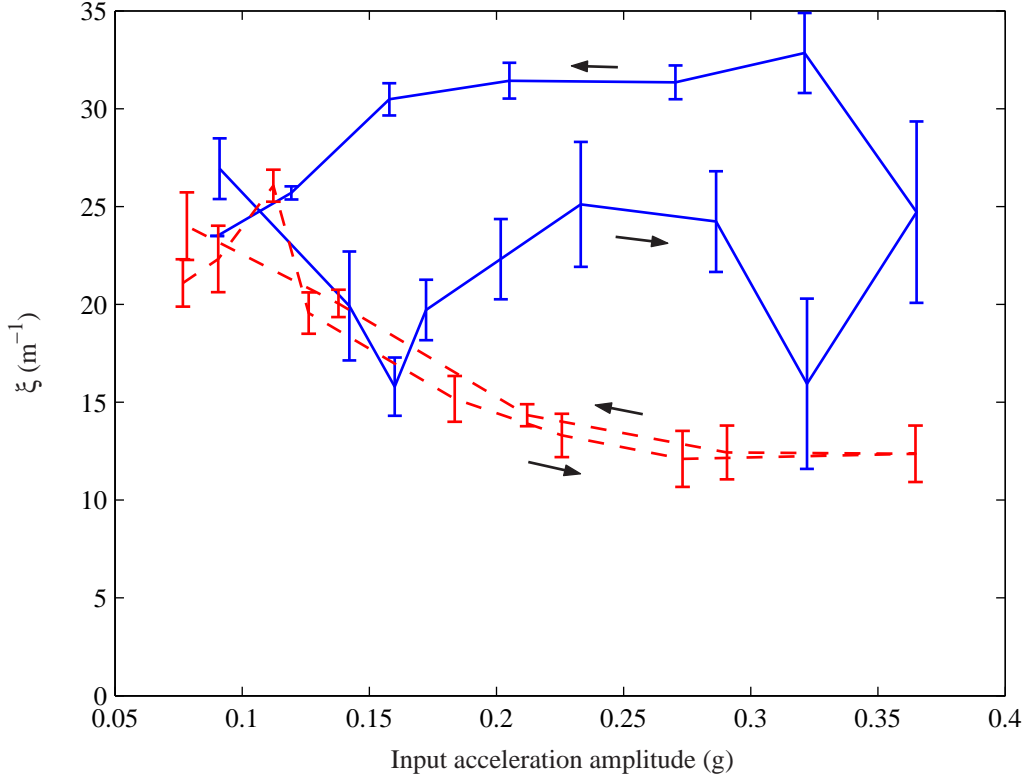
Figure 3.7: Attenuation ratio for an unconsolidated bed (solid) and a consolidated bed (dashed) of 4 mm glass beads as the amplitude of the input wave is increased and then decreased.

Trends in the measurements of attenuation through the bed are similar, but more exaggerated, than those of the wave speed. Figure 3.7 shows the attenuation ratio at varying levels of the piston acceleration amplitude for both an unconsolidated and a consolidated bed. Again, rearrangement leads to a lack of repeatability in the unconsolidated bed. In fact, there is no repeatability between the increasing and decreasing acceleration amplitude paths at any value of the amplitude. A different mean value of the attenuation ratio is found over the entire range of accelerations. As before, the consolidated case shows comparatively good repeatability compared to the unconsolidated case. The attenuation for the consolidated case is consistently lower than that for the unconsolidated case. Less of the wave energy is diverted into relative particle motion so a reduced amount of attenuation is observed.

The scatter in the data, as in the wave speed results, also indicates bed rearrangement. For the unconsolidated case, the scatter in the attenuation data increases slightly with acceleration. In contrast, the consolidated bed has roughly the same amount of scatter at all accelerations. The scatter is also generally larger for the unconsolidated bed compared to the consolidated bed.

3.3   Summary

The results of experiments with a continuous, sinusoidal wave source show the unique properties of wave propagation in a granular bed.

Experiments in which the acceleration amplitude was fixed showed the nondispersive character of a granular as was previously observed by Liu and Nagel (1994). For a variety of materials and particle sizes, the phase shift between the pressure signals arriving at two transducers at different distances from the wave source varied linearly with frequency. Based on a linear analysis, such a dependence implies nondispersive wave propagation and a constant group velocity. The measured group velocities were compared for different particles and experimental conditions. Little or no variation was observed in the group velocity with increasing particle size. Increased pressure (through increased particle overburden) and consolidation increased the group velocity slightly, but the greatest influence on the group velocity was found to be the composition material of the particles as characterized by the bulk sound speed in the material. The group velocity was found to be over twice as large in glass particles compared PVC particles. Based on simulations to be presented later, a dependence of the group velocity on Poisson's ratio (in addition to this sound speed) is also expected.

Measurements of attenuation through the bed were also made. The variation of the attenuation with frequency was much more irregular than the group velocity, but did tend to increase with frequency. Particle material composition was found to have the largest impact on the attenuation, but the trend was contrary to what was expected. The attenuation was higher in the stiffer glass particles than the softer PVC particles. The effect of consolidation, pressure, and particle size was minimal.

Constant frequency experiments demonstrated the tenuous nature of the particle contact network. Measurements of the wave speed and attenuation in an unconsolidated bed showed a high degree of hysteresis while increasing and then decreasing the acceleration amplitude of the piston. Scatter was also high in these measurements as both the wave speed and attenuation varied with time at large input amplitudes. Both the scatter and the hysteresis are the result of particle and force chain rearrangement from the action of the input waves alone. Performing the same experiments in a consolidated bed led to more repeatable curves and reduced scatter.

Chapter 4

Experiments with pulsed input

In this chapter, the properties of waves that result from a pulsed motion of the piston are described. The discrete nature of such excitation allows for the determination of absolute attenuation characteristics of the granular bed without the complicating factor of resonant behavior that is inherent with sinusoidal excitation. Both the effects of the shape of the input pulse and the level of consolidation of the granular bed are explored. To systematically examine the effect of the input pulse on the characteristics of these waves, the input width and amplitude of the pulse are independently varied while maintaining a positive, square shape. For consolidation studies, the wave propagation characteristics before and after consolidating the bed are compared. More information on the experimental setup can be found in Section 2.1.2.

4.1 General characteristics

4.1.1 Wave shape

A typical wave due to a pulsed motion of the piston is shown in Figure 4.1. The wave consists of a sharp rise from the static pressure, p_0, followed by a smooth increase to the maximum pressure, p_{max}, due to the passing wave. The static pressure is the pressure that results from the weight of the particles above the point of measurement. The amplitude of a given pulsed wave, Δp, is just the difference between p_{max} and p_0. After reaching a maximum, the pressure falls off smoothly until it approaches the static pressure value at which point there is a local pressure minimum before a series of oscillations. The details of these oscillations will be addressed in Section 4.2.1. Since the pressure in the initial peak does not cross the static pressure value, the wave width is chosen to be the time over which the pressure is above half of the pressure amplitude.

The propagation speed of the wave is determined based on its arrival at the two transducers. The arrival time was taken as the point at which the pressure signal deviates from the static pressure value by more than the signal noise and is exemplified in Figure 4.1. Other points were explored in defining
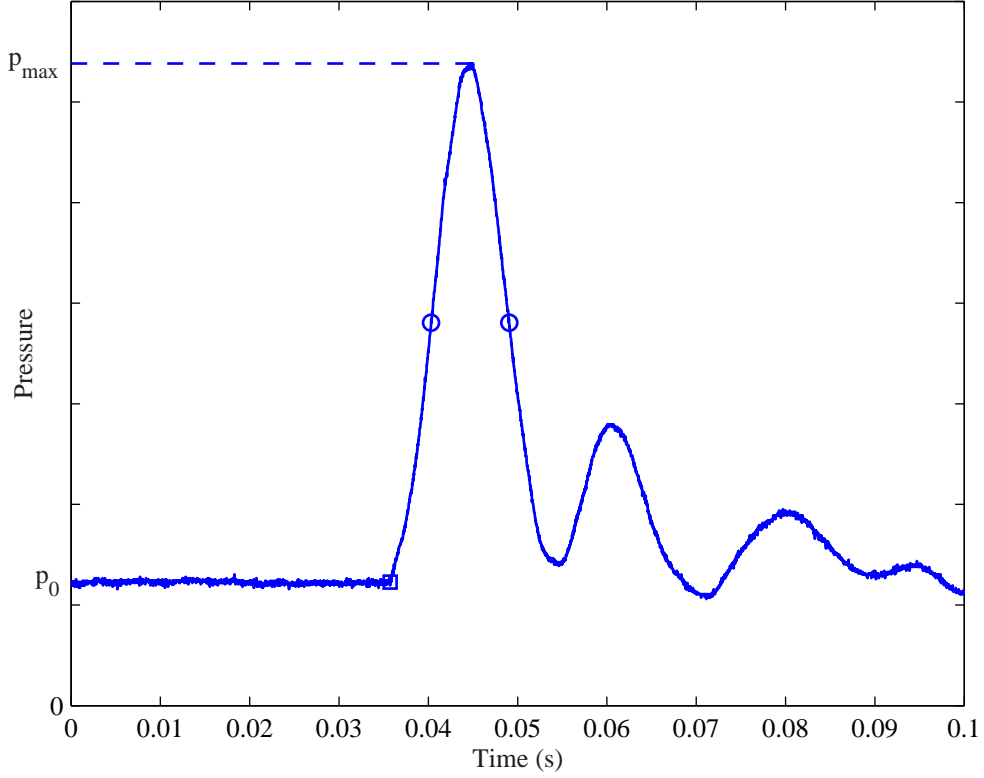
Figure 4.1: Experimental signal showing a representative wave due to a pulsed motion of the piston. The point used to calculate the arrival of the wave is shown with a square. The width of the wave is determined at the location of the circles.

the wave's arrival; alternatives included the time at the pressure maximum, p_{max}, and the time at which the pressure reached half of its maximum. Neither of these produced results as consistent as the point of the first change in the pressure. The wave shape changes with propagation and with parameter variations lead to the imprecise results from the alternative techniques. Discussion of the measured wave speeds will be postponed until Section 4.4. It is appropriate to discuss other features of the pulse propagation first.

4.1.2 Pulse attenuation

The spatial decay of the pulsed wave is shown in Figure 4.2 for both glass particle and plastic particle cases. A longer box (84 x 25 x 16.5 cm) was used for these measurements so that the range of transducer spacings could be extended.

Attenuation is significantly higher in the PVC compared to the glass beads. The decay rate is over twice as great for the PVC. Even though the attenuation in the glass particles is low compared to the PVC, it is still quite high in an absolute sense. It was experimentally observed that a pulse in 3 mm glass particles is completely attenuated at a distance of 420 mm from the piston. One
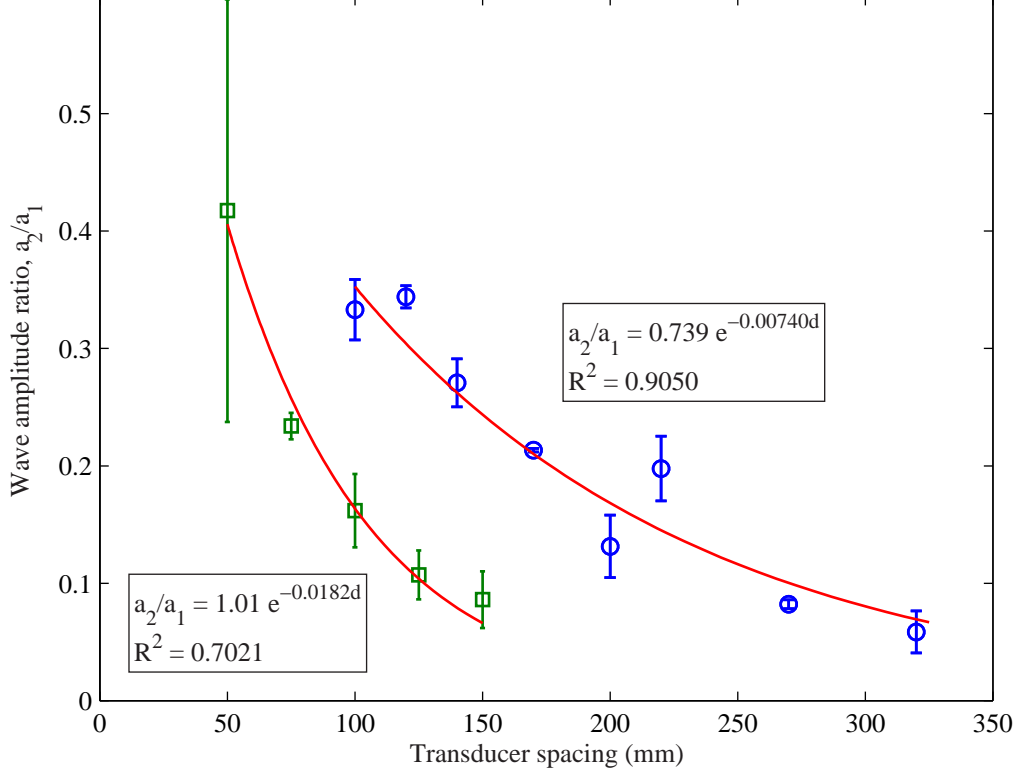
Figure 4.2: Pressure amplitude ratio decay with increased distance between the transducers. The near transducer, with pressure amplitude a_1, is fixed at 50 mm from the piston while the far transducer is moved. Results for both 3 mm glass beads ($\circ$) and PVC cylinders ($\square$) are shown. Each point is the mean of several points. Error bars show the standard deviation of the measurements.

advantage of the high attenuation is the reduced possibility of wave reflections interfering with the measurements. Even in the smaller box with the glass particles, all of the wave energy is dissipated before a wave can return to the transducer after being reflected from the wall opposite the piston.

For both data sets, an exponential curve fits the data with reasonable success. The fit for the PVC particles is detrimentally affected by the scatter in the data at a 50 mm spacing. The increased scatter is likely a result of the comparably few particles that fill the space between the transducers. Fewer particles per length lead to a reduction in the granular bed's ability to average the signal over multiple wave paths. The quality of the fit would be much improved if this point were omitted. The success of the exponential fit shows that the amplitude ratio is properly formed as an attenuation ratio. If this data is plotted as an attenuation ratio, it is nominally constant with distance.

4.2 Constant pulse amplitude experiments

In the first set of experiments, the input pulse amplitude was held fixed and the duration of the pulse (the input pulse width) was incrementally changed. The amplitude of the pulse sent to the shaker

was set to 0.2 V and the width was varied from 2 to 66 ms. Due to the complex dynamics between the piston and the granular bed, these electronic settings on the pulse generator do not provide much information regarding the true input to the bed. For this reason in plots that follow, the input to the bed is described in terms of the characteristics of the wave at the near pressure transducer. The relationship between the electronic pulse amplitude and the near wave pressure amplitude is shown in the left of Figure 4.10. At each setting of the width, four data points, corresponding to four waves, were taken. Two waves were captured in a single sampling period. Several seconds later, a second sample was taken with two more waves. This procedure was used to quantify any transient changes in the measurements. If the bed were changing with time as a result of the pulses altering the force network, measurements would vary between individual waves. Adjacent waves would show possible changes in the bed over short time scales. The comparison between the two samples separated by seconds would show longer-time transient effects.

Figure 4.3: Wave shape for four different input pulse widths (4,14,41,65 ms) for a fixed input pulse amplitude of 0.2 V. Measurements made at 50 mm from the piston in a bed of PVC cylinders.

The effects of input pulse width on the shape of the detected pressure waves are shown in Figure 4.3 and Figure 4.4. For small input pulse widths, the wave consists of a single peak much like the wave shown in Figure 4.1. The 4 ms and 14 ms waves in the PVC, Figure 4.3, and the 6 ms wave in the glass, Figure 4.4, are examples of such waves. This initial peak is followed by a series of

oscillations around the static pressure value.

As the input pulse width is increased, two changes are observed. First, the amplitude of the detected wave increases. This effect is thought to be a result of the limited response time of the shaker and will be discussed in more detail later. The second effect is what appears to be a splitting of the individual peak into multiple peaks. This splitting is most evident in the change in the wave shape between the 14 and 41 ms pulses. The largest input pulse width, 66 ms, shows the developed shape. The additional peaks are actually oscillations, similar to those seen around the static pressure value, that ring about an elevated pressure due to the forward motion of the piston. The elevated pressure level falls off abruptly as soon as the piston is retracted during the last part of the pulse.
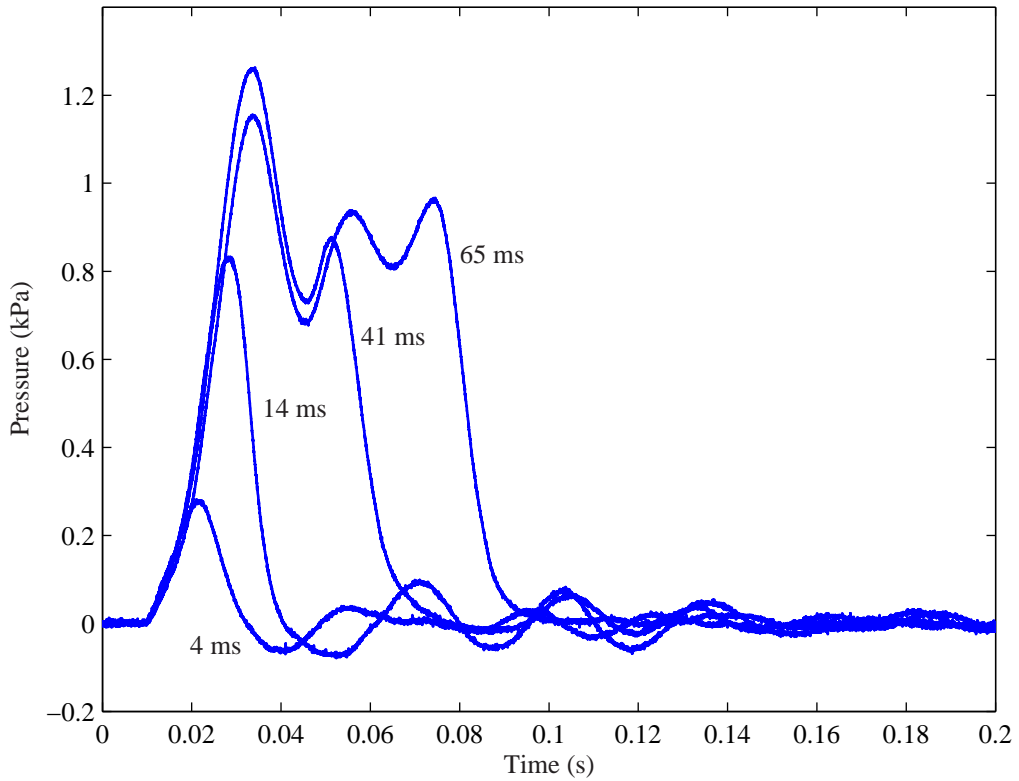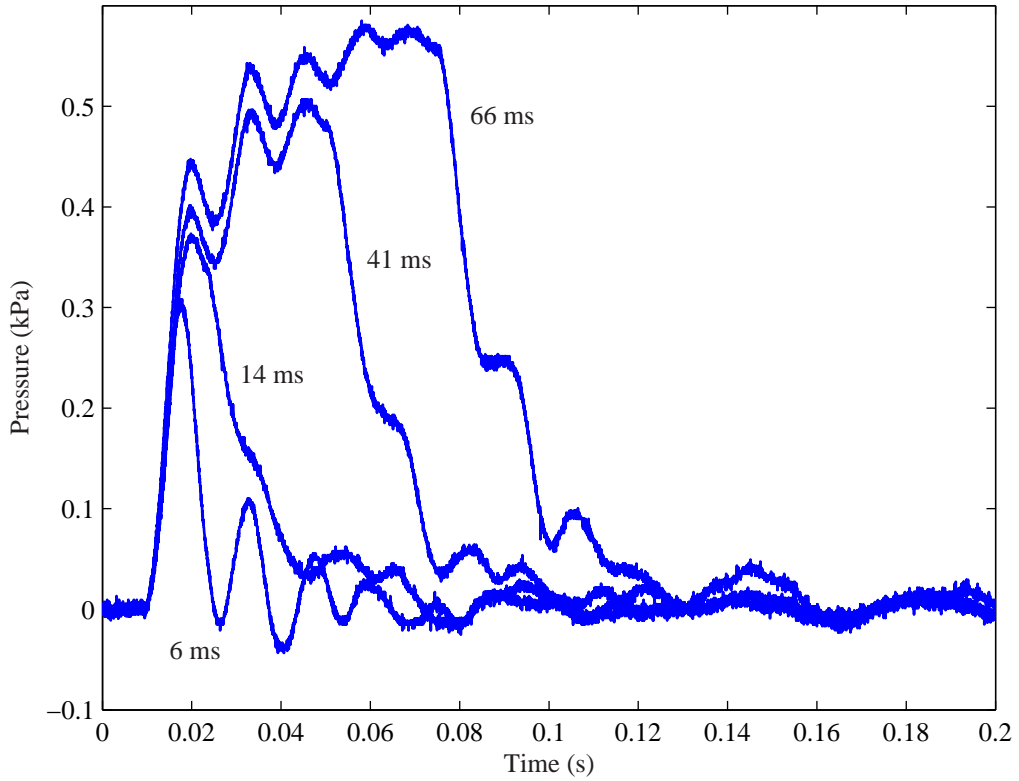

Figure 4.4: Wave shape in 3 mm glass for four different input pulse widths (6,14,41,66 ms) for a fixed input pulse amplitude of 0.2 V. Measurements made 50 mm from the piston.

The wave shapes in 3 mm glass, Figure 4.4, are qualitatively similar to the PVC results, but there are a few interesting differences. Splitting of the wave peak is also observed in the glass. A single wave breaks into multiple peaks as the input pulse width is increased. In the glass particles, the transition case between one and two peaks has been captured. This case is the 14 ms wave in Figure 4.4. The shape of this wave is a combination of the primary and secondary peaks. For the larger input widths, where the oscillations about the elevated pressure are apparent, the transient behavior is different than that of the PVC. The mean of the pressure during the oscillations continues

to rise as the ringing proceeds. This behavior is in contrast to that of the PVC in which the pressure oscillates around a value slightly less than that of the first peak. The two materials also produce differences near the end of the pulse. For the larger input widths, the drop in the pressure for the glass is accompanied by a trailing bump in the pressure that is absent in the PVC. The large width PVC cases simply drop smoothly to the static pressure value.

Figure 4.5: The left figure shows the amplitude of the detected pulse in PVC particles at transducers 50 mm (∘) and 100 mm (□) from the piston as a function of the pulse width. The right figure shows the attenuation rate.

Looking more quantitatively at the changes in the wave with increasing input pulse amplitude, Figure 4.5 shows the effect on the measured wave amplitude. The wave amplitude increases smoothly with input pulse width and then becomes constant at around 30 ms. This behavior is likely associated with the response time of the electromechanical actuator. The amplitude of the pulse from the pulse generator specifies the displacement of the piston. For the widths less than 30 ms, the actuator does not have enough time to reach its displacement target due to a physical acceleration limit. Increasing the input width allows the actuator to get progressively closer to its target amplitude by giving it more time to respond. At 30 ms, the actuator is able to respond fast enough and after this point, the amplitude input is constant leading to a constant measured wave amplitude. By comparing the cutoff level of 30 ms with the wave shapes in Figure 4.3, it is clear that the constant wave amplitude regime occurs after wave splitting.

The small amount of scatter in this data is also remarkable. Over the entire range of input pulse widths, there is very little divergence in the four data values at each width setting. This repeatability of the data suggests that minimal rearrangement of the particles is occurring between measurements.

The attenuation is plotted on the right side of Figure 4.5. The trend is fairly consistent with what was seen for the wave amplitude. The attenuation is roughly constant at 21 m^{-1} for the larger

widths. For widths less than 20 ms, there is some dependence on the value of the input pulse width.
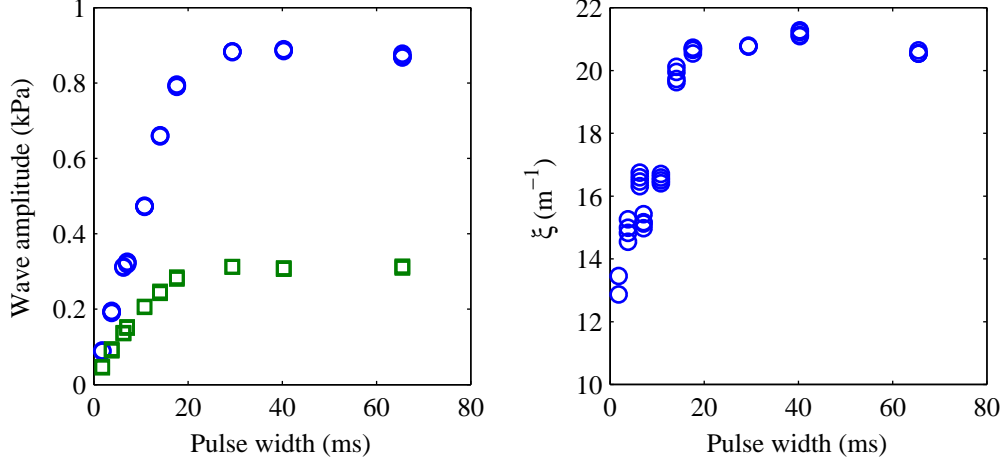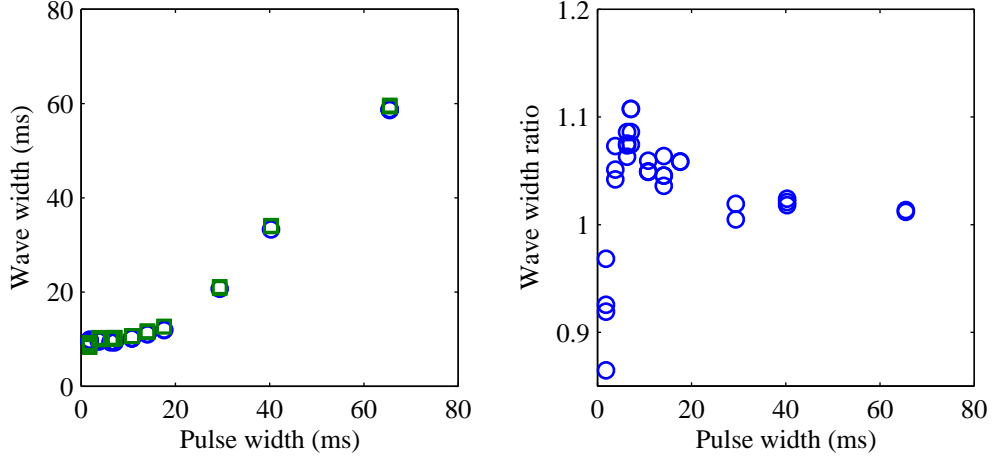

Figure 4.6: The left figure shows the wave width of the detected wave in PVC particles at transducers 50 mm (○) and 100 mm (□) from the piston as a function of the pulse width. The right figure shows the ratio of these widths (far/near).

The variation in the detected wave width with input pulse width is presented in Figure 4.6 (left) and shows two distinct regimes. For larger input pulse widths (greater than 20 ms), the detected width just scales with the input pulse width as one would expect. In this range, the wave width is always less than the pulse width, a result of how the wave width is measured. Since the width is taken at the half-height, the width should always be less than a width measured at the base of the wave, which should be much closer to the pulse width. The more intriguing regime is that at small input pulse widths (less than 10 ms). Here, the detected wave width is independent of the input pulse width. Regardless of the input pulse width, the width of the detected wave is 10 ms. This width corresponds to a disturbance with a frequency of roughly 50 Hz. Waves in this regime are a form of semi-permanent wave for which the input conditions have little effect on the wave shape. Semi-permanent waves were also observed in simulations (see Section 6.1). In the simulations, the wave width was nearly the same regardless of the shape or size of the pulse that created it.

The right portion of Figure 4.6 shows the ratio of the wave widths measured at the two transducers. Over most of the range of input pulse widths, wave broadening occurs. That is, the width measured at the far transducer is greater than that measured at the near transducer. Only the smallest input pulse widths show the opposite trend and these points may be suspect due to the weakness of the signals at such short pulse widths.

4.2.1 Oscillations

Focus is now shifted to the oscillations that are observed behind the primary peak of these pulsed waves. The origin of these oscillations is still uncertain. The typical frequency of the oscillations is
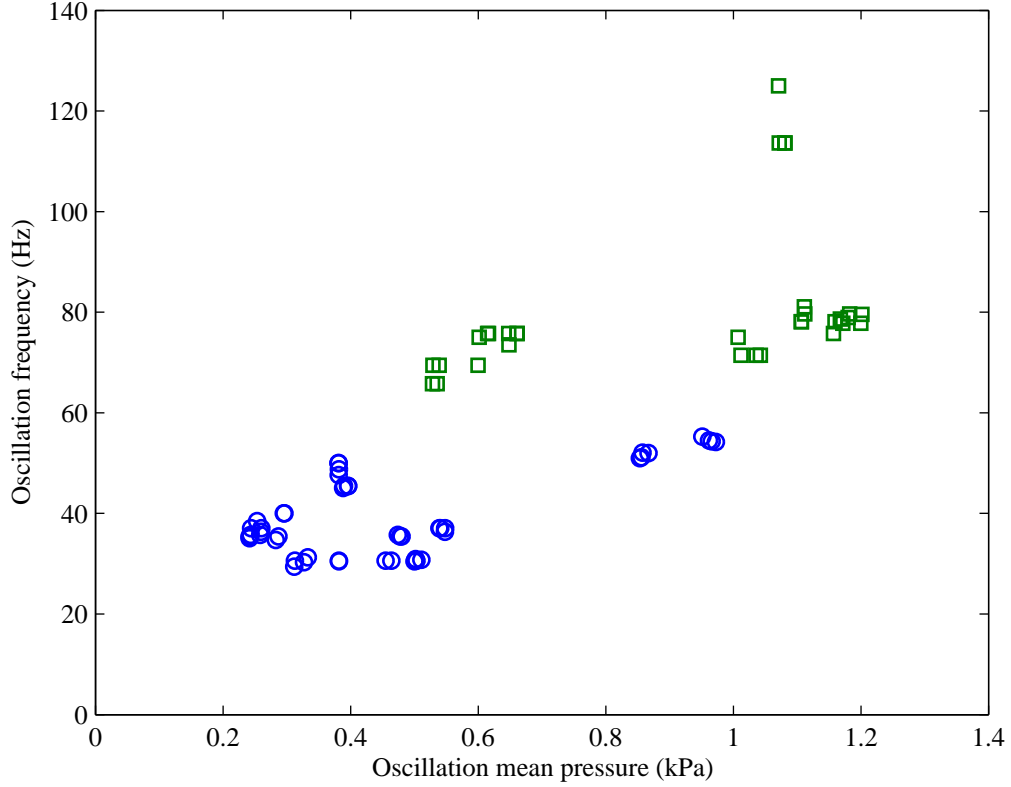
Figure 4.7: Frequency of the oscillations after the passing of the initial peak plotted as a function of the mean pressure during the oscillations. Measurements were made in PVC (○) and 3 mm glass (□) particles.

in the range 25 to 80 Hz. These frequencies are far too low to be attributed to the natural frequency of the transducer diaphragm. They are more likely associated with some structure on a larger length scale. One possible explanation is that these oscillations constitute a natural frequency of the force chains through which the waves travel. In this scenario, one would expect the frequency to increase with the confining stress on the chain. Thus, ringing about an elevated pressure level should occur at a higher frequency than ringing about the static pressure.

Two different types of ringing were observed. Short-duration oscillations were seen at the elevated pressure due to the push of the piston (see Figure 4.3: 41 and 65 ms widths) and just after the release of the piston about the static pressure (see Figure 4.4: 6 ms width). These oscillations were characterized by a relatively smooth, sinusoidal shape. They were limited in duration to a maximum of three periods. Long-duration oscillations were observed behind the wave after any short-duration oscillations (see Figure 4.9 after 0.2 s) and could last for as long as twenty periods. Their structure was comparatively noisy, but their frequency was consistently 20 Hz. In contrast, the short-duration oscillations could take on various frequencies in the range 25-80 Hz.

An effort was made to calculate the oscillation frequencies and relate them to the confining pres-

sure on the particles. The degree of confining pressure was determined as the mean pressure about which the oscillations occurred. The frequencies of the short-duration oscillations were determined by windowing two to three periods of the ringing and calculating the frequency by inspection. The use of Fourier spectra proved ineffective due to the limited number of periods of the oscillation. No more than three periods were used as the character of the oscillations appeared to change to that of the long-duration oscillations after this period of time.

The results of these calculations are shown in Figure 4.7. There is an apparent linear dependence of the frequency on the mean pressure despite the scatter in the data. Note that the gap in the mean pressure for both the PVC and glass constitutes the boundary between oscillations about the static pressure and those about the elevated pressure. Ringing about the elevated pressure consistently occurs at a higher frequency than that about the static pressure. This result provides at least some indication that the frequency is dependent on some variable property of the bed and is consistent with the hypothesis that the oscillations arise from a natural frequency of the force chains.

To estimate the natural frequency expected from theory, a 1-D chain of identical particles as depicted in Figure 1.3 is considered. The system is modeled as a series of masses for the particles connected by nonlinear springs with a Hertzian relationship between the force, F, and the overlap, δ between particles such that

$$F = K_2 \delta^{3/2}. \tag{4.1}$$

It is assumed that the chain of particles is subjected to an initial force, F_0, which leads to an initial particle overlap, δ_0, between each pair of particles. The nonlinear force-overlap relation is then linearized about this initial overlap. The linearized stiffness about this initial overlap will be

$$k = \frac{dF}{d\delta} = \frac{3K_2 \delta_0^{1/2}}{2}. \tag{4.2}$$

Written in terms of the initial confining force, this stiffness will be

$$k = \frac{3}{2} K_2^{2/3} F_0^{1/3}. \tag{4.3}$$

The force amplitude of the vibrations is assumed to be much less than the confining force. Otherwise, the particles would come out of contact due to the vibrations or the linearization would no longer hold.

The system is now a series of point masses with this linearized stiffness between them. The equation of motion is written for each particle in the chain. The resulting system of equations is solved to find the natural frequencies of the chain of particles. The primary frequency, f_{nat}, will have the form

$$f_{nat} = G\sqrt{\frac{k}{m}}, \tag{4.4}$$

where k is the linearized stiffness between particles, m is the mass of a particle and G is a factor that depends on the number of particles in the chain and the boundary conditions at the end of the chain. In general, G decreases as the number of particles increases. Substituting for k and m $(= \frac{1}{6}\pi\rho D^3)$, the frequency becomes

$$f_{nat} = G\frac{3^{2/3}}{\pi^{1/2}}\frac{1}{\rho^{1/2}D^{4/3}}\left(\frac{E}{1-\nu^2}\right)^{1/3}F_0^{1/6}. \tag{4.5}$$

For a chain of 100 particles with its ends fixed, G will be on the order of 1×10^{-3}. The value of $\sqrt{\frac{k}{m}}$ will be on the order of 1×10^5 Hz for glass spheres if the initial compression force is taken as the weight of particles occupying a height of 80 mm above the point of measurement. The result will be a frequency on the order of 100 Hz which is in the range of the measurements of Figure 4.7. The data in Figure 4.7 may also scale with the pressure to the 1/6 power as the theory predicts the frequency to scale with confining force, but more data is needed to draw a firm conclusion on this dependence.

4.3   Constant pulse width experiments
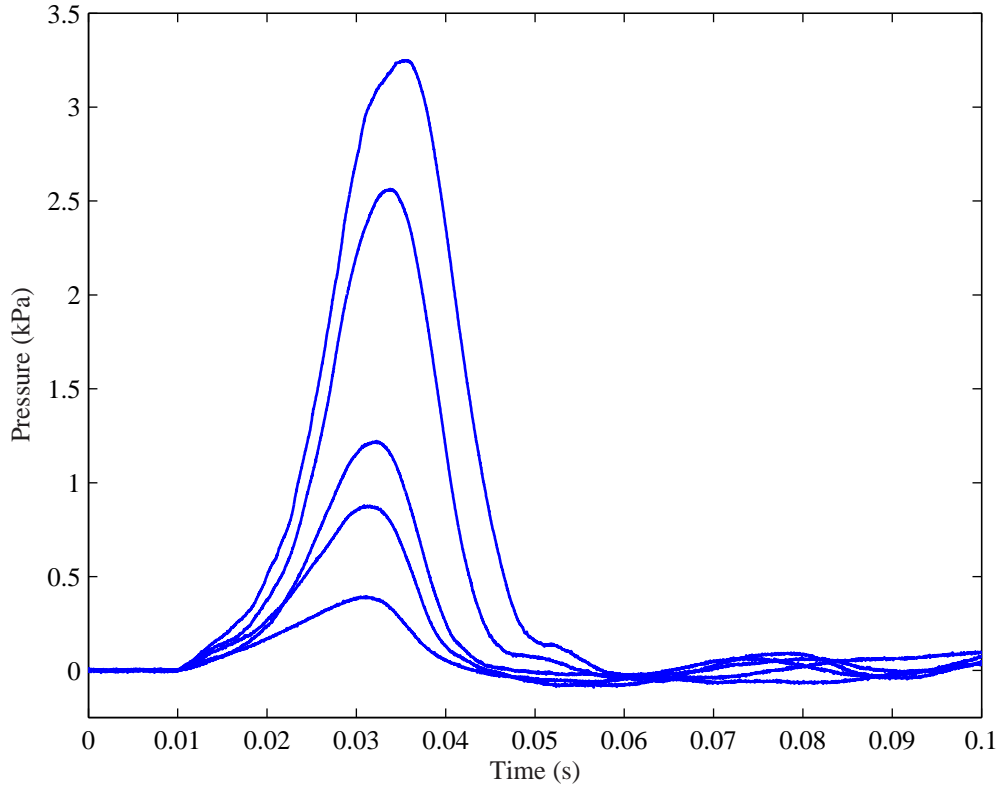
Figure 4.8: Wave shape in PVC for five different input pulse amplitudes for a fixed input pulse width of 18 ms.

A second set of experiments was carried out to examine the effect of increasing the input pulse amplitude on the measured properties of the waves. The width of the wave was fixed at three different values (6,18,40 ms) and the pulse amplitude was varied from 0.1 - 1 V in increments of 0.1 V. Since semi-permanent waves were found to exist below 10 ms, the presented results will primarily focus on waves of width 6 ms.

Figure 4.8 shows the shape of the detected wave as the input pulse amplitude is increased for a fixed input pulse width of 18 ms. This input pulse width is shorter than that which yields wave splitting so one clean wave with a single-peaked structure is obtained. Increases in the input pulse amplitude feed directly into increases in the wave amplitude without significant changes in the wave shape. The exceptions to this similarity in wave shape can be seen at the extremes of the input pulse amplitude range. The smallest wave shown has a much shallower front edge compared to the larger amplitude waves. Its back edge is steeper than the front leading to an overall lack of symmetry. Symmetry is the norm for the rest of the waves.

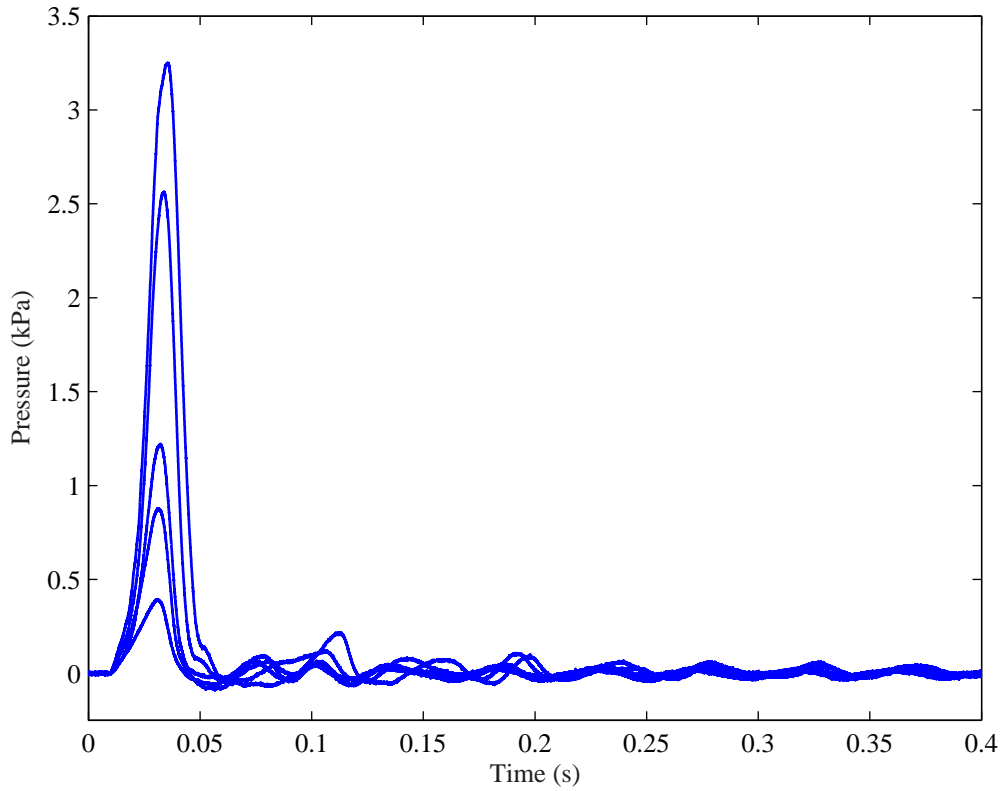Figure 4.9: Wave shape in PVC for five different input pulse amplitudes for a fixed input pulse width of 18 ms.

Figure 4.9 shows the long-time behavior after the primary wave has passed. As was seen in the fixed amplitude experiments, the wake of the primary wave consists of a series of oscillations about the static pressure. The characteristics of this ringing were described in Section 4.2.1. The long-time

(after around 4 cycles) oscillations are in phase. This fact is probably more apparent for this set of experiments than the fixed amplitude experiments since the waves here end at roughly the same point in time. The early oscillations are more irregularly spaced and not generally in phase.

One oscillation is of particular interest due to its shape. The largest amplitude oscillation in Figure 4.9 (at 0.1 s) shows a remarkable similarity in shape to the smallest amplitude primary wave. Both structures have the same asymmetry: a shallow front edge with a steeper back edge. This similarity suggests that this structure in the wake of the largest primary wave may actually be a secondary wave as opposed to some internal vibration. Additionally, the shape of this secondary wave demonstrates a direct relationship between amplitude and wave shape.
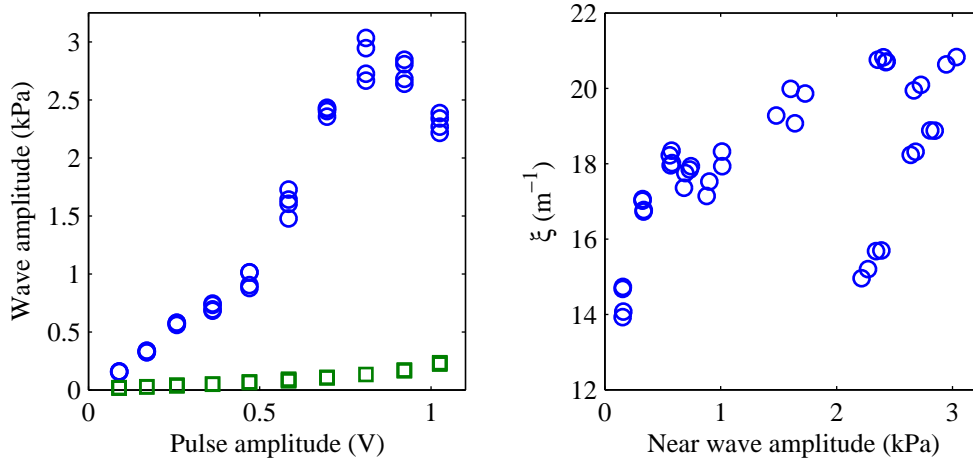
Figure 4.10: Wave amplitude, left, and attenuation rate, right, as a function of the input pulse amplitude for a fixed input pulse width of 6 ms. Measurements are made at transducers 50 mm (○) and 200 mm (□) from the piston in a bed of PVC cylinders.

The wave amplitude data on the left of Figure 4.10 shows the relationship between the voltage specified at the pulse generator and the pressure amplitude of the waves measured in the granular bed. In later plots, the pressure amplitude at the near transducer is used to characterize the amplitude input to the bed. Figure 4.10 provides strong evidence that rearrangement of the force chains is occurring for the larger pulse amplitudes. For the smaller pulse amplitudes at the near transducer and at all pulse amplitudes for the far transducer, the wave pressure amplitude increases in a regular, although nonlinear, fashion with the input pulse amplitude. Beyond pulse amplitudes of 0.4 V at the near transducer, the data begins to scatter and then the regular growth trend is broken with the wave amplitude actually decreasing with increasing pulse amplitude for the larger pulse amplitudes. Both of these behaviors are consistent with force chain rearrangement. If one of the multiple force chains connecting the source and the detector was broken, one would expect a drop in the measured pressure. Time-varying measurements resulting from particle rearrangement would account for the increased scatter. The fact that neither of these effects is seen at the far transducer

further strengthens the case for particle rearrangement near the piston where the pressure changes are greatest. At the far transducer, the wave is so attenuated there is not enough energy to cause particle rearrangement. Thus, there is no noticeable effect on the scatter or the trend of the wave amplitude increase.

The right side of Figure 4.10 shows the effect of increasing input pulse amplitude on the attenuation measured in the bed. The majority of the data increases in a regular, quadratic manner with increasing input amplitude to the bed and tends to approach a constant value of 21 m^{-1} for the largest pressure amplitudes. The two groups of data points below this curve correspond to the largest two voltage inputs to the shaker. Since the pressure amplitude decreases at these two voltages, comparisons with the rest of the data are dubious. For such large amplitudes, the decrease in the pressure is most likely the result of a reduction in the number of force chains connecting the wave source and the detector. A changing number of force chains would lead to an abrupt change in the measured attenuation.
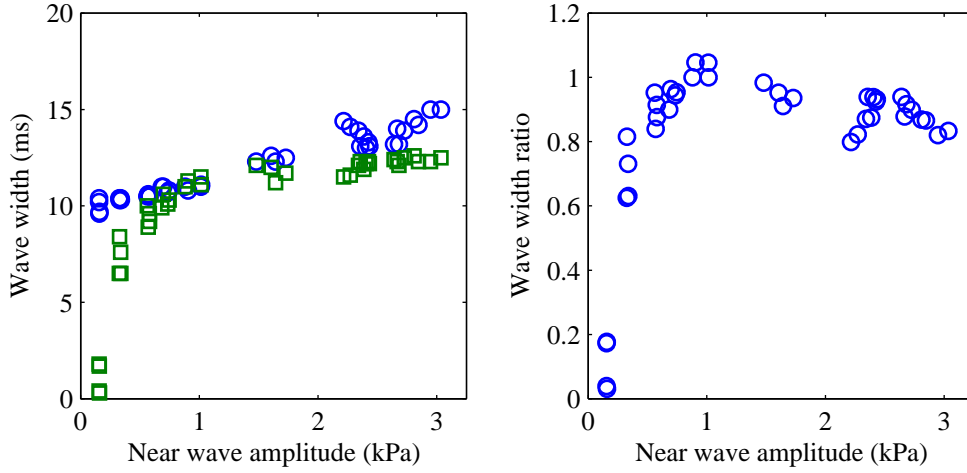
Figure 4.11: Wave width, left, and wave width ratio (far/near), right, as a function of the near wave amplitude for a fixed input pulse width of 6 ms. Measurements are made at transducers 50 mm ($\square$) and 200 mm ($\diamond$) from the piston in a bed of PVC cylinders.

The width of the detected wave increases only modestly with increasing input pulse amplitude. This weak dependence was seen qualitatively in the waves shapes of Figure 4.8, but is detailed on the left in Figure 4.11 for a narrower fixed input pulse width of 6 ms. For the constant input amplitude experiments, a width of 6 ms was found to be in the semi-permanent wave regime. Figure 4.11 shows that even within this regime, the wave width still changes, albeit slightly, with the pulse amplitude. For the near transducer, the relationship between the wave amplitude and width is linear. The scatter in the data increases at the largest pressure amplitudes. Again, this scatter likely can be attributed to bed rearrangement due to the larger pulse amplitude. The width at the far transducer displays a more complex behavior than the linear trend at the near transducer. The fall-off in the

width measurements at the lowest amplitudes is likely an artifact of low signal strength rather than any true effect of the system. There may be some linear portion of this curve, but the range of pressure amplitudes at the far transducer is so limited due to attenuation in the system that it is hard to discern.

The width ratio results shown in right of Figure 4.11 seem to conflict with what was observed in the corresponding figure from the constant amplitude experiments, Figure 4.6. For the constant amplitude case, wave broadening was seen over nearly all pulse widths and, in particular the width used for this set of constant width experiments, 6 ms. Figure 4.11 shows that the waves become narrower (width ratio less than one) for nearly all amplitudes as they travel from the near to the far transducer. The width ratio decreases nearly linearly with pulse amplitude after 1 kPa. The earlier decrease in the width ratio is related to the decrease at the far transducer which was attributed to weak signal effects. The difference in the transducer spacing for the two cases may be the cause of the difference between the two sets of experiments. These constant input width experiments had a spacing three times larger than that used for the constant amplitude experiments. Over this longer distance, the attenuation of the wave may dominate the effect of any nonlinear broadening of the wave.

4.4   Wave speed comparison

The wave speed measured in both the constant input amplitude and the constant pulse width experiments is shown in Figure 4.12 where it is plotted against the amplitude of the wave detected at the near transducer. The measured amplitude of the wave is used because it is an accurate description of the actual input to the measurement. By plotting in this way, the wave speeds measured in both types of experiments coincide for both materials. Increasing the width of the input pulses indirectly increases the amplitude of the detected wave. Directly increasing the input pulse amplitude scans the range more thoroughly. Measurements in both materials have some degree of scatter, but the scatter is significantly larger in the glass particles. The higher wave speed in the glass particles leads to a time shift between the arrival at the two transducers that approaches the time resolution of the measurement. There is little variation in the wave speed with increased wave amplitude.

On average, the speed for the PVC cylinders is around 60 m/s. The wave speed in the glass particles is roughly twice this value, averaging to about 120 m/s. Both of these speeds are is the same range, but slightly lower than their corresponding continuous input measurements. Sinusoidal piston excitation led to group velocities of 75 and 160 m/s for the PVC and glass particles, respectively. This discrepancy is likely related to the difficulty in determining the departure of the pressure from its static value in the pulsed experiments. Signal noise obscures this point of departure, particularly
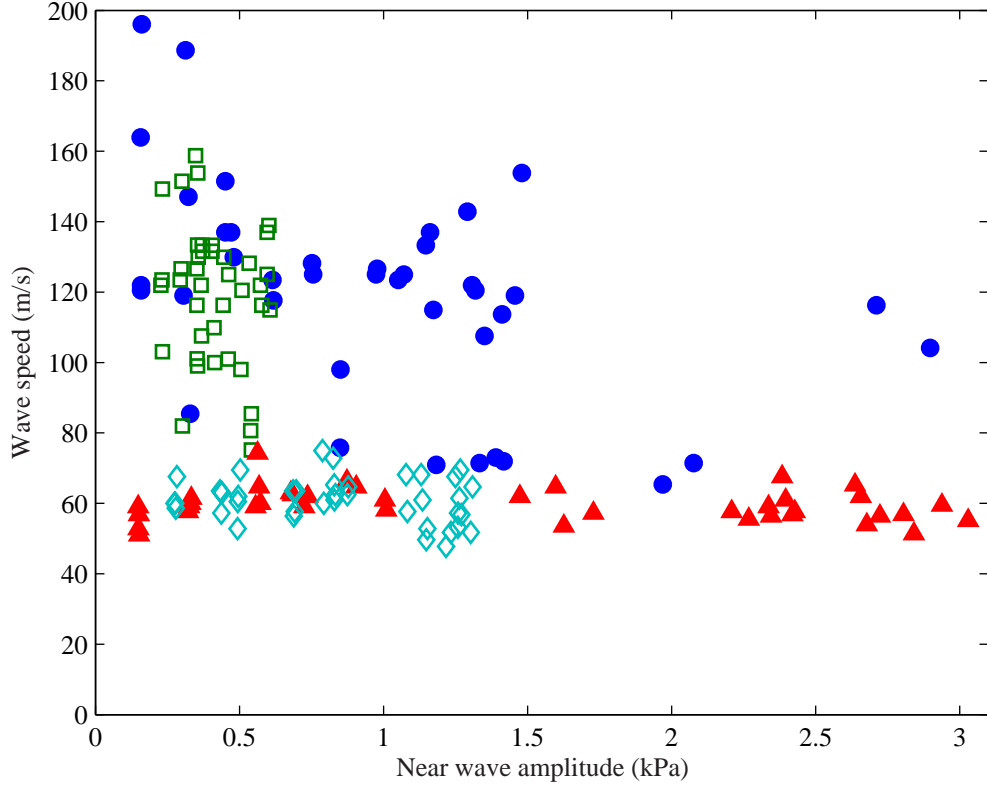
Figure 4.12: Wave speed as a function of the wave amplitude measured at the near transducer. Both constant amplitude (PVC ($\diamond$), glass ($\square$)) and constant width (PVC ($\blacktriangle$), glass ($\bullet$)) experiments are plotted.

in the weaker signal at the far transducer. A delay in the detection of this point relative to a more certain detection for the near transducer signal leads to a reduction of the calculated wave speed.

4.5   Effect of consolidation

One would expect consolidation of the granular bed to have a dramatic effect on its wave propagation characteristics. The denser state that results from consolidation leads to an effectively stiffer bed and reduces the possibility of rearrangement by removing excess potential energy from the system. Details of the consolidation procedure can be found in Section 2.1.

Figure 4.13 compares the measured wave amplitudes in consolidated and unconsolidated beds for both the PVC cylinders and 2 mm glass spheres. The same effects of bed rearrangement that were seen in Figure 4.10 can be seen here. The regular increase in the wave amplitude with input pulse amplitude gives way to irregular, scattered data at the near transducer for the larger pulse amplitudes. In the glass, consolidation limits this effect. The linear increase in the wave amplitude continues past well past the point at which the data from the unconsolidated bed begins to diverge

Figure 4.13: Wave amplitude measured at 50 mm (top figures) and 185 mm (bottom figures) from the piston for an unconsolidated (○) and a consolidated (□) bed. Materials: PVC (left) and 2 mm glass spheres (right).

and scatter. One explanation could be that the denser, consolidated bed impedes the piston motion and prevents magnitudes of the pressure disturbance for which rearrangement occurs. This cannot be the full explanation since the measured wave amplitude exceeds that at which the unconsolidated bed begins to scatter. A second explanation is that the consolidated bed is less fragile so relative particle motion is less likely.

The data from the bed of PVC particles shows the same scatter regardless of consolidation. This may be a result of the relatively irregular shape of the PVC particles compared to the spheres. Force chains constructed from the cylinders may be less stable than those made from spheres.

As was seen before, the signals at the far transducer never show any effect of dynamic particle rearrangement due to wave passage. For the PVC particles, consolidation leads to a change in slope in the plot of wave amplitude against input pulse amplitude. In comparison, the glass data with and without consolidation coincide.

The attenuation ratios that correspond to the wave amplitude data from Figure 4.10 are shown in Figure 4.14. Consolidation consistently reduces attenuation in both materials and reduces the scatter in the data. The consolidated attenuation measurements also show variations with near wave
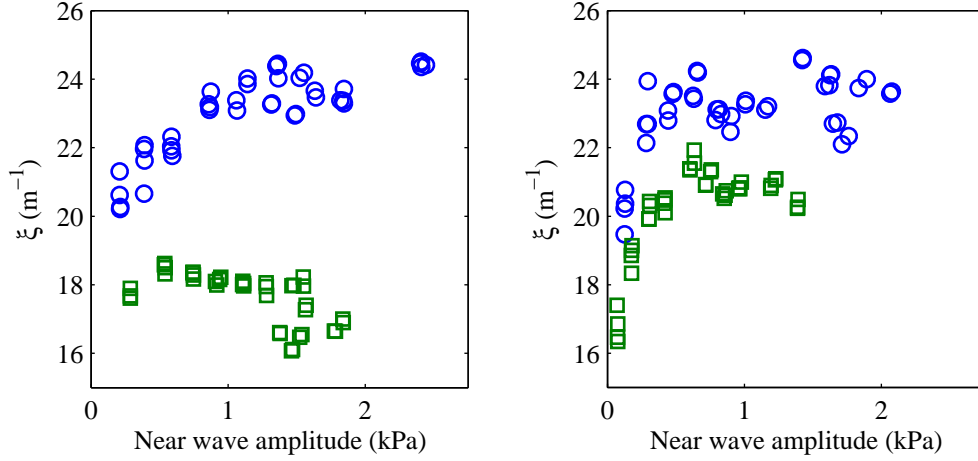
Figure 4.14: Attenuation ratio in an unconsolidated (circles) and a consolidated (stars) bed with increasing initial wave amplitude. Materials: PVC (left) and 2 mm glass spheres (right).

amplitude that are different from the unconsolidated cases.

The effect of consolidation on the measured wave width is displayed in Figure 4.15. The general trend is that consolidation leads to decreased wave width. This is particularly evident in the glass data at the near transducer, but is also clear at the far transducer. For PVC particles, this effect is delayed in terms of the wave amplitude at which it is observed. Consolidation makes little difference in the data for amplitudes less than 1.25 kPa. For larger amplitudes, the wave width is smaller in the consolidated bed at both the near and far transducers. The delay is likely related to the comparative ease of bed rearrangement in the glass relative to the PVC.

The same delay is echoed in the wave width ratio shown in Figure 4.16. The data for the bed of glass particles, the right plot in this figure, decreases linearly with increasing wave amplitude. Interestingly, consolidation makes no difference to the ratio and the data for both the consolidated and unconsolidated beds entirely coincide. This decreasing linear trend can also be seen in the data for the PVC particles in the left of Figure 4.16, but it does not start until after a wave amplitude of 1.25 kPa. Below this value, the width ratio increases with increasing wave amplitude. The data here also largely coincides regardless of consolidation, but there is considerably more scatter.

The results of wave speed measurements in both consolidated and unconsolidated beds for both PVC and glass are plotted in Figure 4.17. For both materials consolidation increases the wave speed as would be expected. The average speeds in the bed of glass particles are 175 and 142 m/s for the consolidated and unconsolidated beds, respectively. The corresponding average speeds measured in a bed of PVC particles are 79 and 59 m/s. Thus, there is a significant increase in the propagation speed due to the density increase associated with consolidation.

Consolidation also leads to slightly increased scatter in data that is already prone to scatter. Scatter is particularly bad in the measurements made in the 2 mm glass particles.
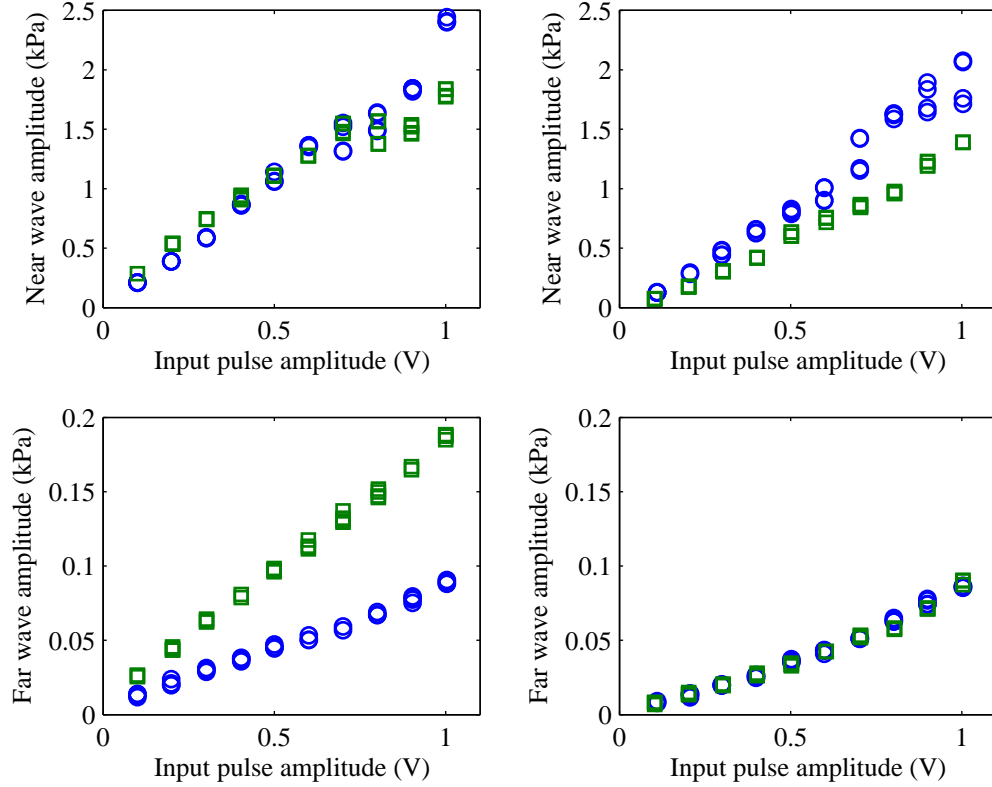
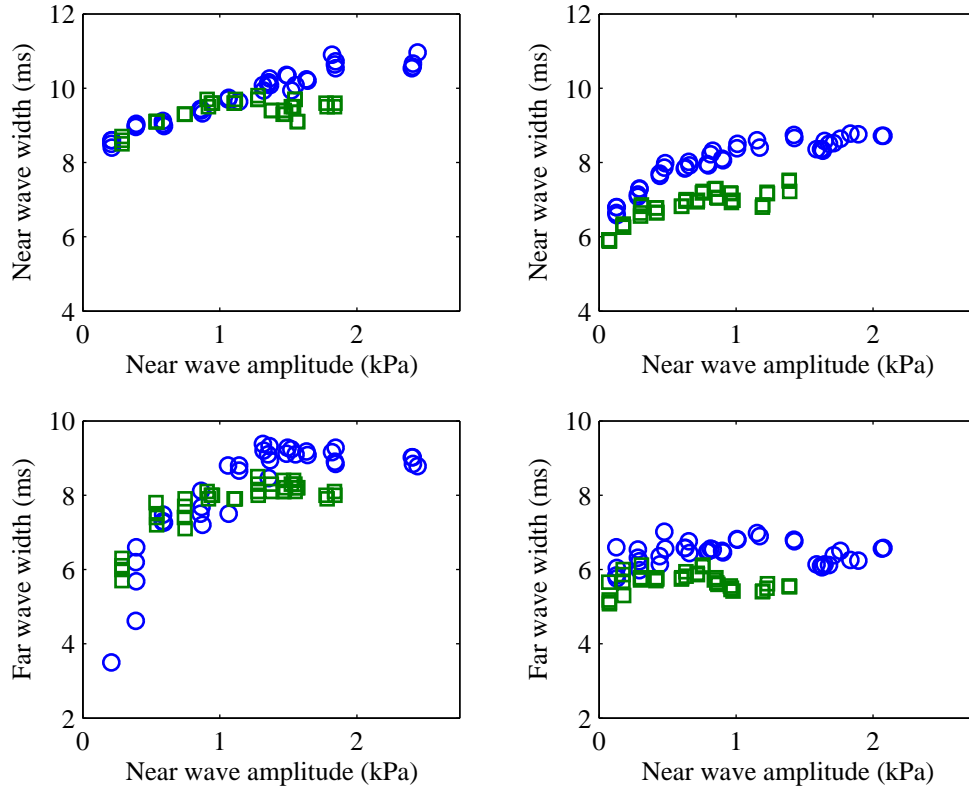Figure 4.15: Wave width measured at 50 mm (top figures) and 185 mm (bottom figures) from the piston for an unconsolidated (∘) and a consolidated (□) bed. Materials: PVC (left) and 2 mm glass spheres (right).
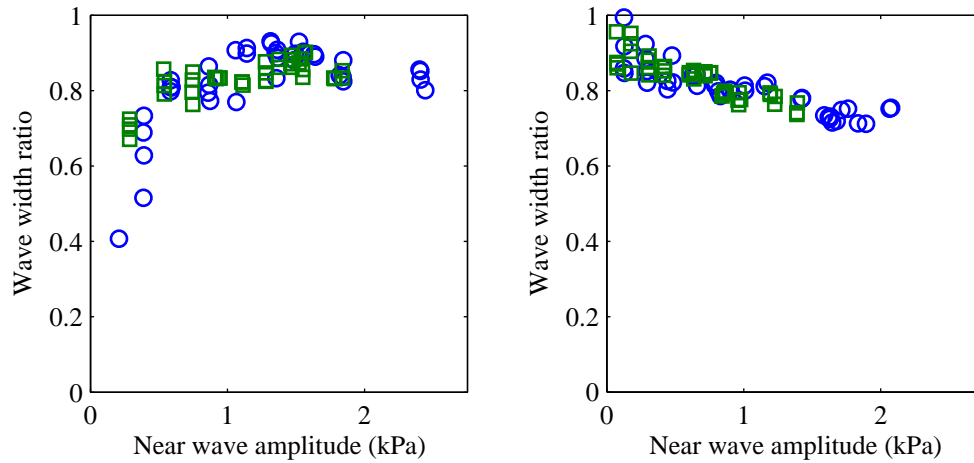
Figure 4.16: The ratio of the wave widths in an unconsolidated (∘) and a consolidated (□) bed with increasing initial wave amplitude. Materials: PVC (left) and 2 mm glass spheres (right).
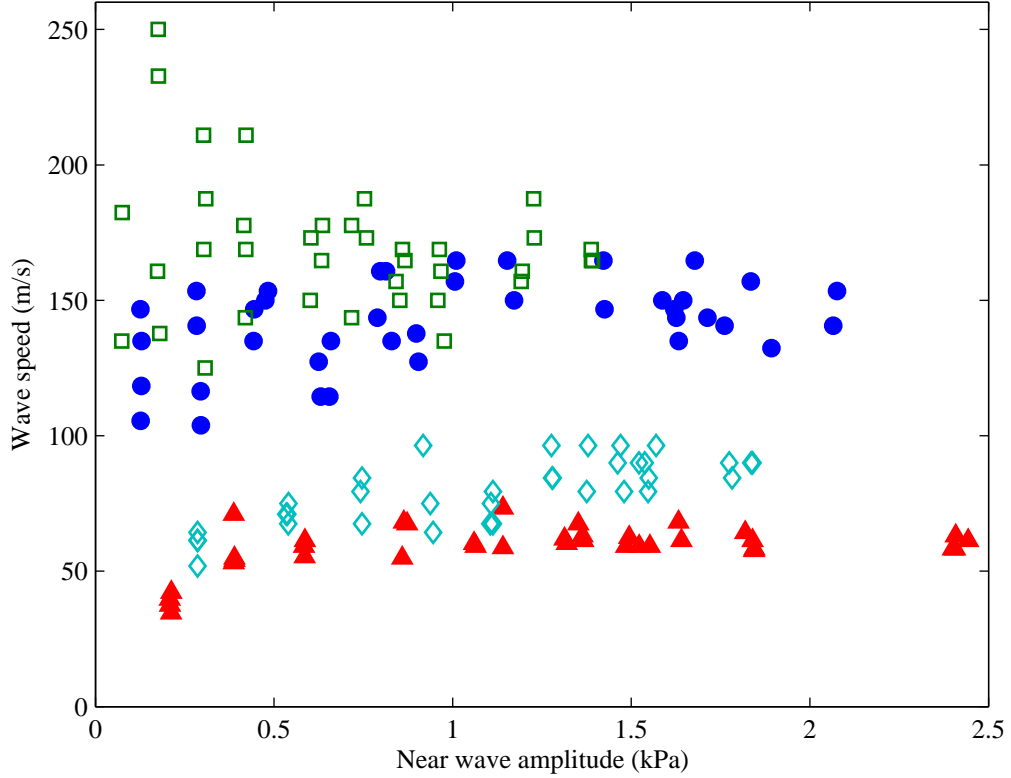
Figure 4.17: Wave speed in beds of 2 mm glass and PVC cylinders. Results are shown for both the unconsolidated (glass (●), PVC (▲)) and consolidated (glass (□), PVC (◇)) state of each bed for increasing initial wave amplitude.

4.6 Summary

In this chapter, the experimental properties of pulsed waves in a granular bed have been examined. Such finite duration waves are particularly useful for probing the attenuation characteristics of the bed since the energy input is finite. The amplitude of these waves was seen to decrease exponentially with distance and the rate of decay was noticeably higher in the PVC particles than the glass particles.

Two sets of experiments were performed to elucidate the relationship between the input pulse shape and the characteristics of the measured wave. In the first set, the input pulse amplitude was fixed and the pulse width was varied. A semi-permanent wave regime was observed for the smallest pulse widths. In this range, the detected width was insensitive to changes in the input width. Such insensitivities are predicted for nonlinear waves in 1-D particle chains (Nesterenko, 2001), but the spatial size of the wave in our experiment does not match the value predicted by the theory. Both the amplitude of the waves and the attenuation were constant at sufficiently large input widths, but increase for smaller widths.

Constant pulse width experiments confirmed previous observations on the effect of increasing

wave amplitude. Particle rearrangement led to increased scatter and irregular changes in wave amplitude and width measurements for the largest input amplitudes. The wave speed showed no variation with wave amplitude. Any variation was lost in the relatively high degree of the scatter in the wave speed data compared to the other measurements. The wave speeds measured in both the glass and PVC particles were comparable to, but slightly smaller than the group velocities measured in the continuous input experiments.

In the course of these experiments, some interesting oscillations in the pressure signal were seen behind the primary pulsed waves. Due to the relatively low frequency of these oscillations, they must occur over some appreciable length and may be the result of a natural frequency of the force chains. To support this idea, the oscillation frequency was compared to the confining pressure. Consistent with what is expected for the natural frequency of a force chain, the oscillation frequency increased for larger confining pressure and increased with the stiffness of the particle material.

The effect of consolidation was also examined. Consolidation of the bed was seen to consistently decrease attenuation and increase the wave speed through the granular bed.

Chapter 5

Simulations with continuous input

This chapter presents the results of simulations in which a sinusoidal excitation is introduced at the left wall of the simulation cell. The simulation procedure is described in Section 2.2. The results demonstrate the effectiveness of the simulations in capturing the essential physics of the problem, as demonstrated by the good agreement with the experimental measurements.

5.1 General characteristics

After the settling period (described in Section 2.2.3) and before the generation of waves, the static pressure stabilizes at some value dictated by the geometric configuration of the granular bed. At this point, the left wall is set into motion at a specified frequency and amplitude. Typical pressure traces that result from the sinusoidal motion of the left wall are shown in Figure 5.1. The pressure recorded at both walls is sinusoidal in shape and is smooth and relatively devoid of noise. The shape of the signal is free of any steeping of the peaks due to nonlinear effects, at least at this level of the input amplitude. The phase shift between the signals is apparently about half a period of the signal. The phase speed is derived from this shift. As expected, the mean pressure level is larger for the measurements made deeper in the bed. Due to the heterogeneity of the bed, the mean pressure measured at the same depth in the bed (left versus right wall) shows some variation. This effect occurs at both depths at which sensors were placed.

To examine the frequency dependence of the wave propagation characteristics, a series of frequencies were propagated into one particular bed configuration. The acceleration amplitude of the left wall was maintained through the changes in frequency, effectively applying a constant force amplitude to the bed. Figure 5.2 shows the long-time pressure response of the system through these frequency changes. The dependence of the pressure amplitude on the input frequency as well as the transient behavior for a given frequency can be seen. Fixing the acceleration amplitude leads to a decreasing maximum displacement of the left wall as the frequency is increased. Thus, one may expect the measured pressure amplitude of the waves to also decrease with increasing frequency.
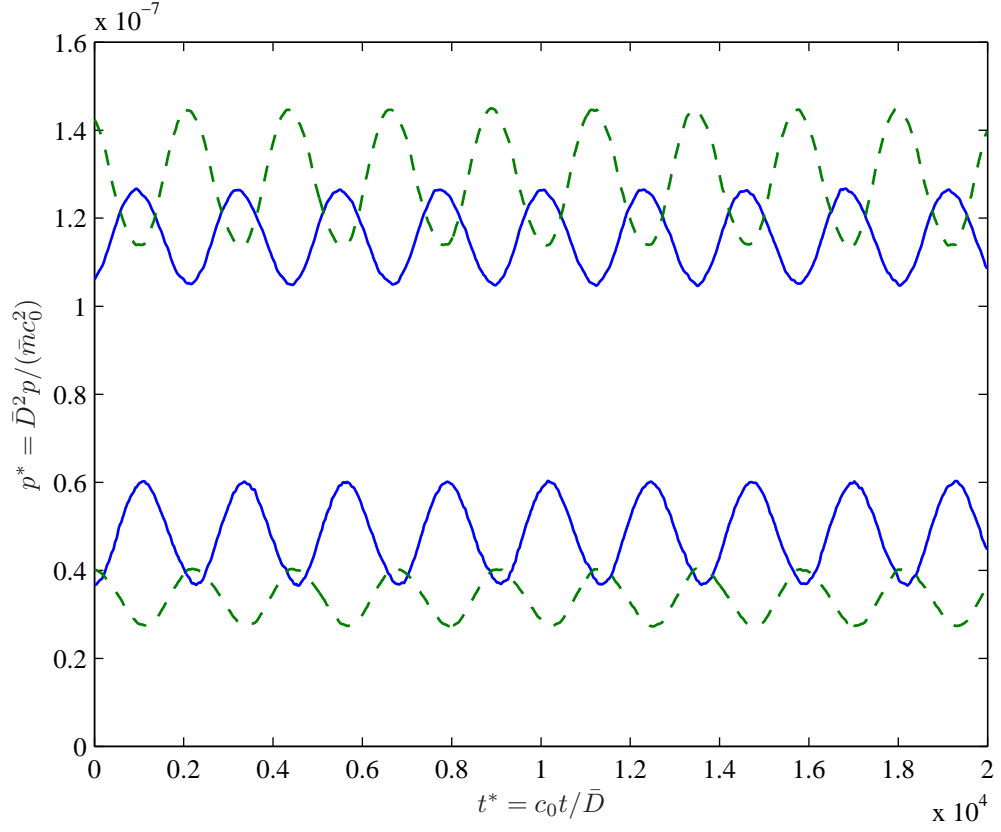
Figure 5.1: Representative signals resulting from sinusoidal motion of the left wall of the simulation cell. The input signal, the pressure at the left wall is plotted as solid lines and the detected signal, the pressure at the right wall, is plotted as dashed lines. The upper curves are from measurements made at 20 particle diameters above the bottom of the cell and the lower curves are from measurements at 50 particle diameters above the bottom.
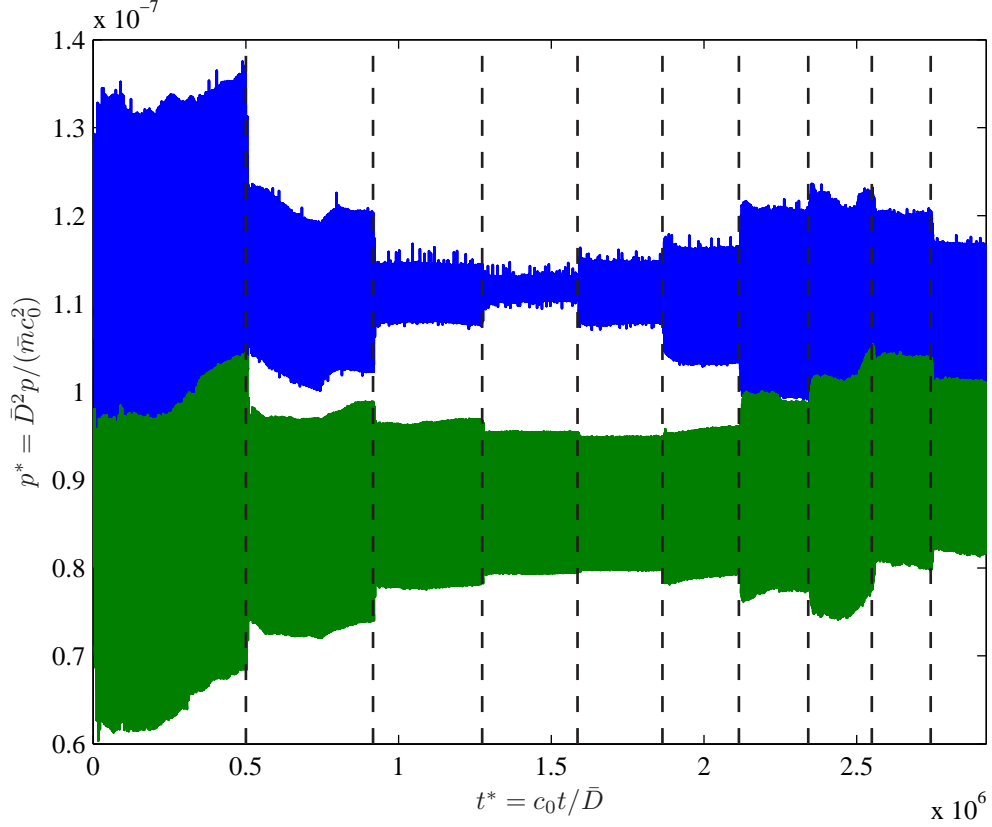
Figure 5.2: Pressure amplitude envelope for ten different frequencies of motion of the left wall of the simulation cell. The upper curve is the envelope of the input signal, the pressure at the left wall, and the lower curve is the envelope of the detected signal, the pressure at the right wall. Both measurements were made 20 particle diameters above the floor of the bed. Dashed lines show the frequency changes. Each division has 100 cycles of a given frequency.

The response is slightly more complicated. The pressure amplitude does decrease, but eventually increases at higher frequencies after establishing a minimum. This minimum is more likely a result of resonant behavior in the system than decreasing excitation displacement amplitude. More information on this resonance can be found below in Section 5.3.

The transient behavior at a given frequency consists mostly of a drift in the mean pressure and is most pronounced for the larger pressure amplitudes. However, the pressure amplitude remains roughly constant despite this shifting mean pressure. The mean pressure drift is likely a result of particle rearrangement due to the larger pressure amplitude. At smaller pressure amplitudes, the pressure amplitude as well as the mean pressure remains constant for the duration of a particular input frequency.

5.2   Phase and phase speed

The phase shift between the pressure detected at the right wall and the displacement of the left wall is shown in Figure 5.3. The general trend of the data is linear, as was seen in the experiments, but here the deviations from the trend are more pronounced and systematic. At first, the strong deviations were thought to be the result of changes in the pressure amplitude. As shown in Figure 5.2, there are large variations in the pressure amplitude with changes to the frequency input into the system. Closer inspection failed to produce any definite correlation between the pressure amplitude and the undulating portions of the phase versus frequency curve. The systematic nature of the variation suggests that some other unaccounted for system parameter is responsible for the deviations.
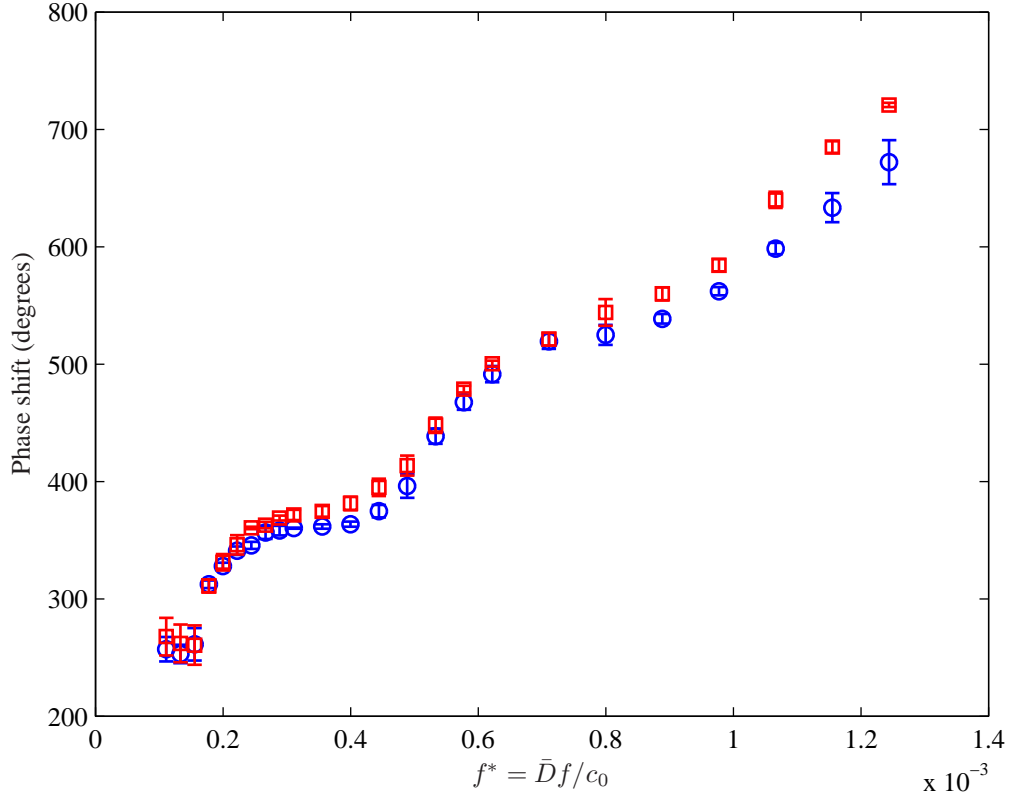
Figure 5.3: Phase shift between the output pressure (right wall) and the displacement of the left wall. Measurements are made 20 ($\circ$) and 50 ($\square$) particle diameters from the floor of the bed.

Even with the variations in the data, a straight line is a good fit at both the lower and upper sensors ($R^2 = 0.9712$ and $R^2 = 0.9799$, respectively). The slope from the fitted line leads to a group velocity (see Section 1.2.3.1) in dimensionless units of 0.0525 at the lower sensor and of 0.0480 at the upper sensor. In a bed of glass particles, these speeds would correspond to dimensional velocities of 278 m/s and 254 m/s, respectively. Such dimensional values are in the same range as the experimental measurements (170 m/s), but are consistently larger. This mismatch with experiments

indicates the need for some adjustment in the particle contact model. The group velocities from the simulations also obey the expected variation with depth in the bed. The group velocity is larger at greater depth.

A linear trend of phase shift with frequency will lead to a phase speed that does not vary with frequency, but only if the phase shift tends to zero as the frequency tends to zero. The intercept on the phase shift axis is clearly nonzero in Figure 5.3. The nonzero phase shift at zero frequency is likely due to the method in which the phase shift is calculated. The pressure signal at the right wall is compared to the displacement of the left wall (as opposed to comparing the pressures at each wall) using a cross-correlation. This comparison was used because of the weak signal amplitude at the left wall due to resonance effects (see Figure 5.2 and Section 5.3) which led to poor results in the cross-correlation. Comparing dissimilar measurements (displacement vs. essentially acceleration) may introduce an additional phase. This additional phase was calculated from a linear fit of the phase vs. frequency curve and subtracted from the phase shift before determining the phase speed.

The phase speed calculated in this manner is shown in Figure 5.4. As expected, the speed is, on average, constant with frequency and equal to the values of the group velocity found above. The roughly constant phase speed corresponds to nondispersive propagation as discussed in preceding chapters. The deviations about the linear trend in the phase versus frequency curves are mirrored in this plot as variations around this constant speed.

5.3   Wave amplitude and attenuation

The input pressure amplitude, Figure 5.5, exemplifies the resonant behavior of the system. In this figure, the second and third peaks correspond to the primary resonance of the simulation cell width and its first harmonic, respectively. Additional simulations with a simulation cell half the width of that used for Figure 5.5 showed the first peak to be some additional resonance or an artifact of the simulation. In the smaller box, the second and third peaks were shifted to higher frequencies, but the first peak remained at the same frequency. Based on the location of the peaks of the pressure amplitude, the resonant frequency is depth dependent, increasing with depth. The natural frequencies are 5.35×10^{-4} and 5.11×10^{-4} at 20 and 50 particle diameters from the base of the simulation cell, respectively. Physically, these peaks correspond to a situation in which the arrival of the reflected wave back at the left wall is exactly in phase with the motion of the left wall. This synchronization leads to pressure peaks at both the left and the right walls. The change in the pressure amplitude on both sides of the simulation cell can be seen in Figure 5.2. The first frequency (division) from the left is the resonant frequency at this sensor location.

Knowledge of these resonant frequencies allows for an alternate calculation of the wave speed. As was done by Hardin and Richart (1963), a "resonant column" method can be used to find the
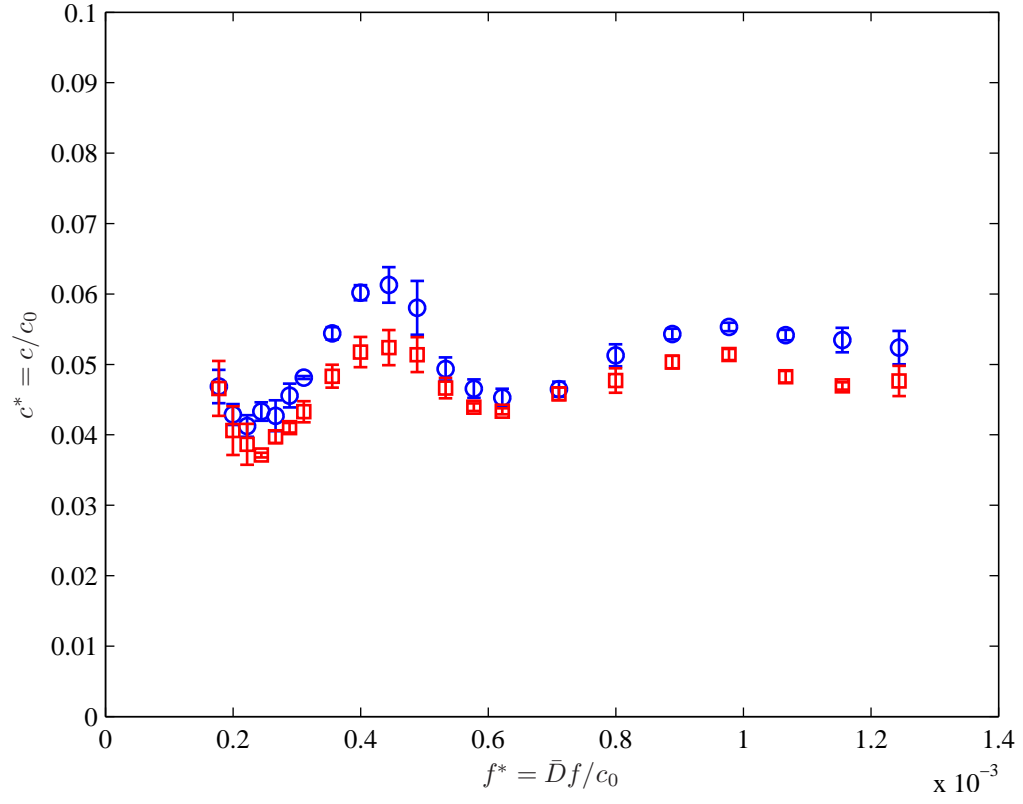
Figure 5.4: Phase speed calculated from the phase shift. Measurements are made 20 ($\circ$) and 50 ($\square$) particle diameters from the floor of the bed.
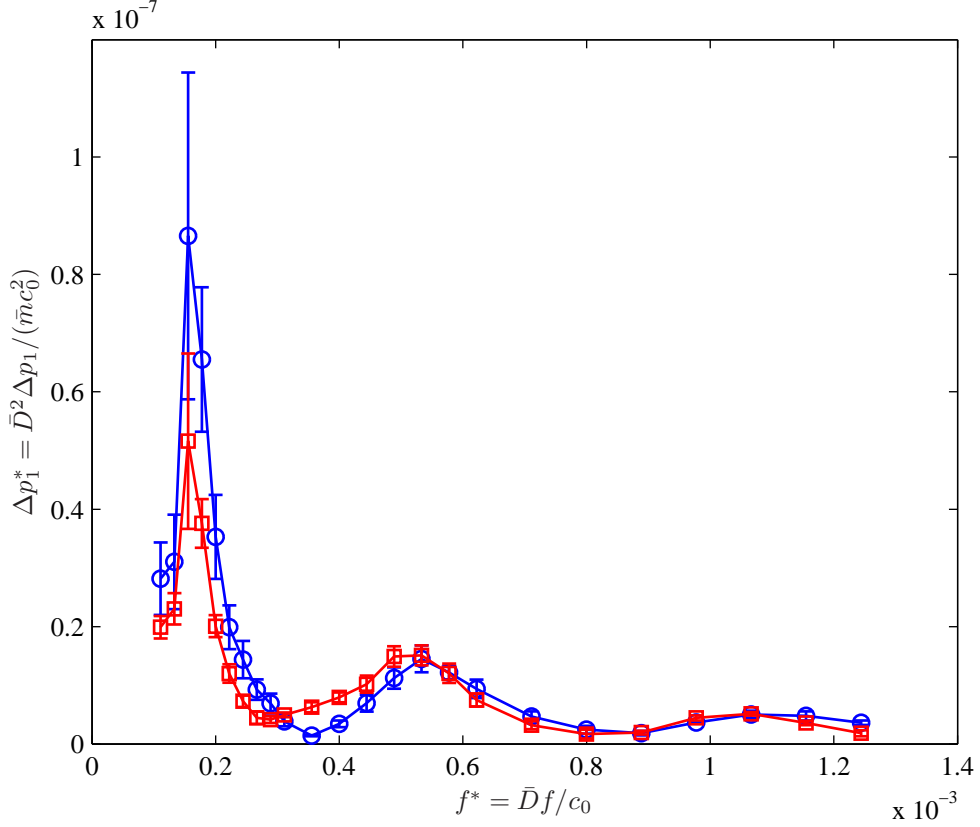
Figure 5.5: Pressure amplitude registered at the left wall of the simulation cell. Measurements are made 20 (∘) and 50 (□) particle diameters from the floor of the bed. Each point is the mean of five independent simulations with the standard deviation of these points shown by the error bars.

wave speed. The resonant frequency should be the reciprocal of the time needed for the wave to travel twice the width of the simulation cell. Thus, the wave speed (in dimensionless units) will be 0.0535 at 20 particle diameters from the bottom and 0.0511 at 50 particle diameters from the bottom. These values are in good agreement with the group velocity measurements presented above (0.0525, 0.0480) and show the same increase in speed for measurements made at greater depth.

The resonant nature of the pressure amplitude casts some doubt on the possibility of drawing conclusions on the magnitude of the attenuation from such simulations. In fact, when compared to the pressure amplitude at right wall, the left wall pressure amplitude was lower over the majority of the frequency range. Thus, for most frequencies, apparent amplification of the wave energy was observed rather than attenuation. The cause of this anomalous behavior may be related to making a pressure measurement on the moving left wall.

5.4   Summary

The results presented in this chapter on simulations with a continuous wave input show good agreement with the corresponding experiments (see Section 3.3). The simulated pressure signals appear identical to those seen in the experiments. A transient drift in the static pressure is observed in the simulations for large pressure amplitudes. The same drift occurred in experiments and is attributed to particle rearrangement in both the experiments and the simulations. The simulations also demonstrate that wave propagation in a granular bed is nondispersive, at least within the frequency range examined. The phase shift between the input and output signal scales linearly with frequency leading to a group velocity that is independent of frequency. The calculated dimensionless group velocities agree well with the experiments when converted to dimensional values using the properties of glass particles. Consistent with nondispersive wave propagation, the phase velocity did not depend on frequency. To obtain this result, a constant phase had to be subtracted from the phase shift results. This constant phase was linked to the method in which the phase shift was calculated. The phase speed was centered about the calculated group velocities and showed the variations that matched those observed about the linear trend of the phase versus frequency curve.

In the course of examining the relationship between the input and output pressure amplitudes, resonance behavior was observed in granular system. Strong peaks in the pressure amplitude occurred at the resonant frequencies of the system. These frequencies depended on the depth in the system at which the pressure was measured. A separate wave speed was calculated from these resonant frequencies following the procedure of Hardin and Richart (1963). This speed agreed well with the group velocity measurements.

Chapter 6

Simulations with pulsed input

Pulsed waves have the advantage of being finite in duration. This discrete size allows for the visualization of a single wave as it crosses a simulated granular bed. The continuous nature of sinusoidal forcing leads to a much more complicated picture as the pressure field in the bed is constantly changing. Additionally, as for the pulsed experimental results, discrete excitation of the bed creates an opportunity for observing nonlinear aspects of the wave propagation that were seen in 1-D particle chain theory and experiments.

6.1   General characteristics

In this section, we will examine the general characteristics of pulsed waves in the simulations and discuss the broad changes that occur with the change of some parameters.

Typical waves that result from a pulsed movement of the left wall of the simulation cell are shown in Figure 6.1. The typical wave consists of a smooth positive pressure peak followed by a region of substatic pressure. The pressure returns to the static value after a series of oscillations. Physically, the pressure peak corresponds to the compression of a number of particles in contact with the wall. The description for one of these particles is as follows. A particle adjacent to the detector at the wall initially compresses due to the passing wave. After the passing of the pressure peak, the particle relaxes past its static compression level before eventually returning to its equilibrium compression after a series of oscillations.

The pressure oscillations are either due to reflections of the wave within the simulation cell or more local effects such as a natural vibration frequency of a particle or particle chain. Reflections may be possible in the simulations due to reduced attenuation in the bed. In the experiments, waves are fully attenuated before they can be detected after a reflection. Reduced attenuation, due to dimensionality, cell size or other effects, may allow for reflections to be detected in the simulations. For small (< 1 mm) particles, the simulation cell is as much as a fifth the width of the experimental box. Each additional particle contact allows for more dissipation before the second arrival of the
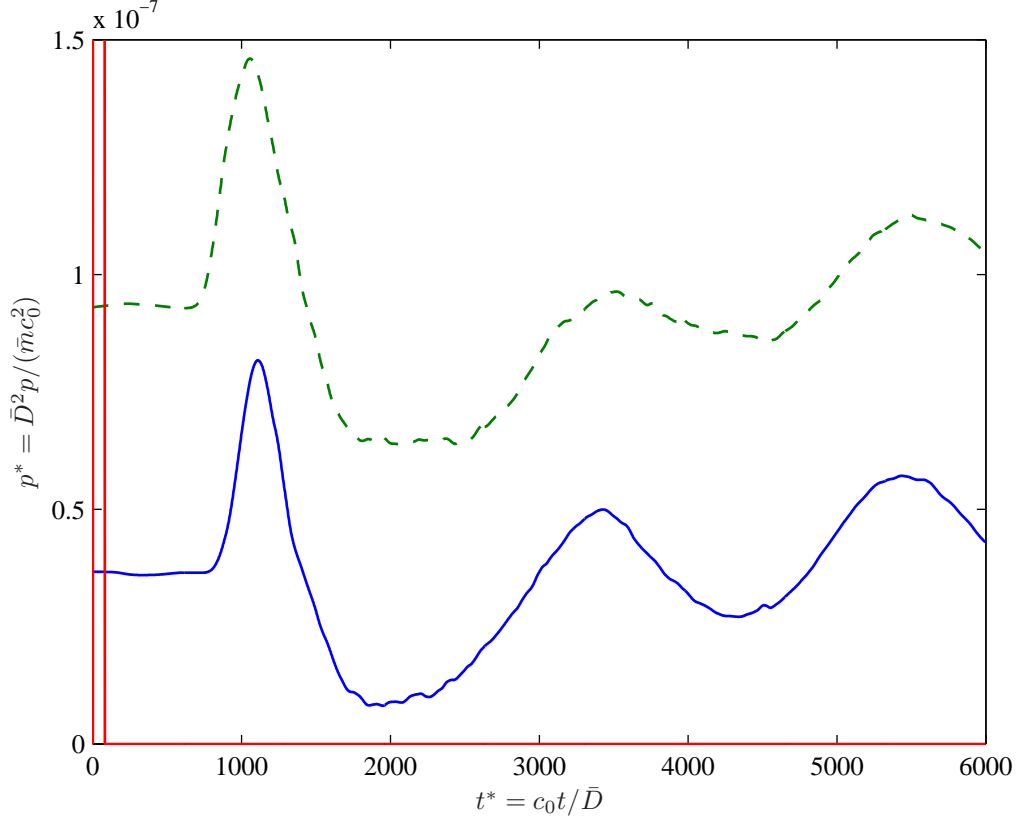
Figure 6.1: Wave shape resulting from a pulsed movement of the left wall. Ratio of input displacement to static deformation is of order 10. Pressure is measured on sensors (10 particles high) on the right wall 50 particles (solid) and 20 particles (dashed) above the bottom with the bed free surface at 76 particles above the bottom. The pulse width is shown on the left of the plot.

wave. Similarly, the additional dimension of the experiments provides more particle contacts and the possibility of energy scatter into the plane. Evidence that ringing following a pulsed wave may be related to the natural frequency of a force chain was found in the experiments (see Section 4.2.1) and may also be related to the oscillations here.

The depth in the bed where the measurement is made affects the undisturbed pressure level as well as the amplitude of the wave. As one would expect, a measurement deeper in the layer leads to a larger static pressure. The difference in the wave amplitude follows from the nonlinearity of the contacts between particles. Since the slope of the force-displacement curve for particle contacts is ever increasing (see Figure 1.2), a constant displacement leads to a greater force at a location with greater prestress.

The width of the wave measured at each of the sensors is similar and both are significantly larger than the width of the input pulse. This was found to be a general trend. Changes in the input pulse width over several orders of magnitude changed the detected width only slightly. This trend is shown explicitly in Figure 6.7. Changes to the shape of the input pulse also led to minimal changes

in the wave width. Due to these insensitivities, we will refer to these waves as semi-permanent. Similar behavior was observed in the experiments, at least over certain ranges of the input pulse width and amplitude (see Section 4.2).
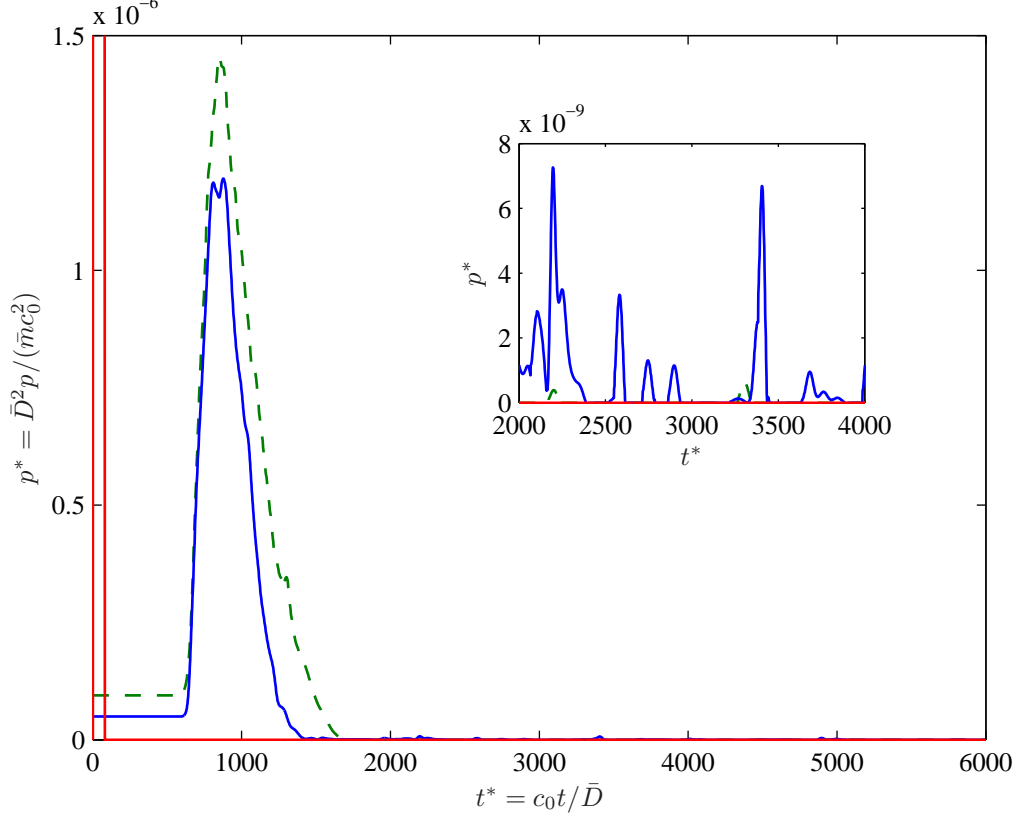
Figure 6.2: Wave shape for a comparatively large amplitude pulse. Ratio of input displacement to static deformation on the order of 100. Pressure is measured on sensors (10 particles high) on the right wall 50 particles (solid) and 20 particles (dashed) from the bottom with a bed free surface at 76 particles. Inset is a detailed view of region behind the wave in which the pressure drops to zero.

A convenient means of comparing different wave amplitudes is to examine the ratio of the input pulse displacement to the static displacement of particles due to the confining stress. The confining stress was obtained as the force at the half-height of the bed due to the weight of the particles above the half-height. A static displacement was calculated from this force using Hertz's law. The order of magnitude of this ratio is noted in the captions of Figures 6.1 and 6.2. As seen in Section 1.2.4, the limits of this ratio define the regimes in which exact solutions for a 1-D chain of identical particles can be found.

Qualitative differences are seen in the wave structure as the amplitude of the input pulse is increased. Figure 6.2 shows the shape of the wave at the two detectors for an input pulse ten times larger than that shown in Figure 6.1. The wave is characterized by a comparatively steep leading edge that resembles a shock front. The trailing edge is less steep, but still tends to zero rather quickly

with none of the oscillations that were observed for the smaller amplitude wave. This drop to zero pressure is a result of a much stronger reflection of the wave from the right wall. Zero pressure implies that the particles at the detector momentarily lose contact with the detector as they recoil from the wall.

An enlarged view of the zero pressure region of the signal, as shown in the inset of Figure 6.2, does reveal some pressure activity. In this region, the pressure signal is characterized by short, relatively rare pressure peaks indicative of collisional particle motion. The amplitude of these peaks ($\Delta p^* \approx 4 \times 10^{-9}$) is three orders of magnitude smaller than the wave amplitude and the width of these peaks, in dimensionless time units, is in the range $t^* = 50 - 70$. Such widths, as well as the shape of the pressure spike, are consistent with measurements made by Zenit (1997) for the collision of a particle on the face of a high frequency response pressure transducer. Zenit measured the width of these pressure spikes to be on the order of 10 μs, with a typical case measuring 22 μs. The measured width of 22 μs corresponds to dimensionless width range of $t^* = 389 - 23$ for glass particles of diameters between 0.3-5 mm, respectively. Comparison of the amplitude of these peaks is difficult due the dimensionality difference between Zenit's experiment and the current simulations. Zenit measured a typical maximum pressure of 20 kPa due to a particle collision with the sensor.

Interestingly, the collisional pressure peaks are only observed at the sensor located higher in the bed. Both pressure traces are plotted in the inset figure, but the trace at the lower sensor is nearly imperceptible. The lack of pressure peaks at the lower sensor is likely a result of reduced particle mobility at depth due to increased overburden. The weight above the particles at 20 particles from the bottom prevents them from entering a collisional regime. Higher in the bed, dilation occurs more easily, creating space in which a particle can translate and then collide.

Since the state of each particle is known entirely, an alternate means of visualizing the wave is to look at the instantaneous force between particles. At its most basic level, the wave is just a propagating force front that is initiated by the force applied at the left wall and is transmitted through particle contacts. Figure 6.3 is the result of such a visualization for the pulsed wave with a moderate pulse amplitude shown in the pressure traces of Figure 6.1. Shading codes the magnitude of the net horizontal force on a given particle. Blue corresponds to zero force and red corresponds to a fixed force value of $F^* = 5 \times 10^{-9}$. The effect of the pulsed motion of the left wall is seen in the first frame. The displacement of the wall creates a wave front that is parallel to the wall. As the wave travels, the curvature of its front increases since the wave travels faster at greater depth. The second and third frames show the development and growth of this curvature. An increase in the wave speed with depth is certainly expected. The effective medium theory of Goddard (1990) predicts that the wave speed, c, will scale with the pressure, p, as $c \sim p^{1/4}$ in the relatively low pressure upper layers of the granular bed. Assuming that the pressure increases linearly with depth, the quarter-power scaling will also hold for the wave speed with depth.
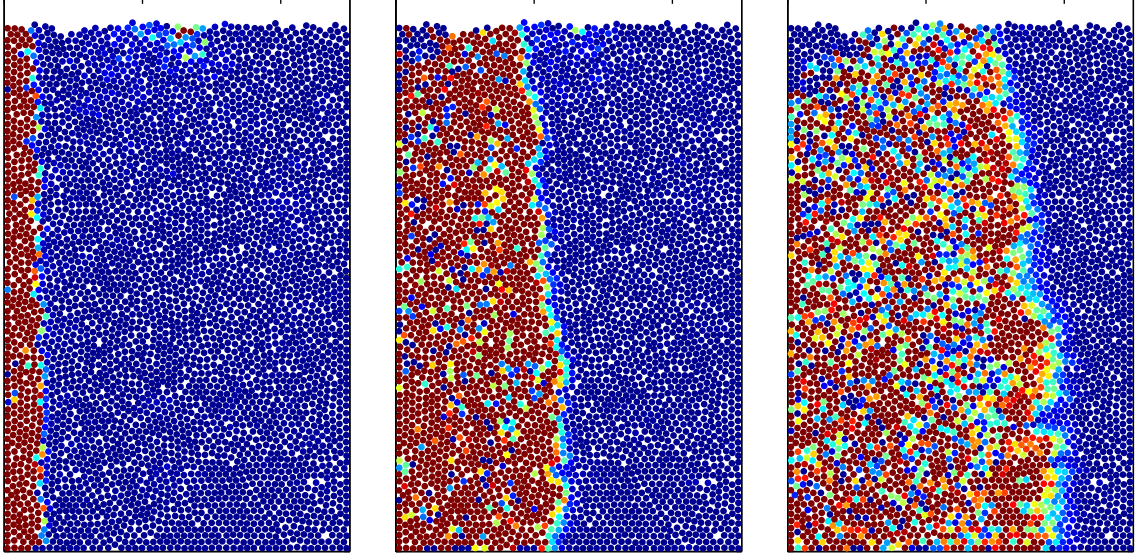
Figure 6.3: Transmission of a pressure wave in a static granular bed. Frames taken at intervals of $t^* = 250$.

Another unique feature of the wave front is its irregularity. Such irregularity is expected due to the heterogeneous nature of the bed. The size of the irregularity elements appears to grow with time. In the first frame, there are variations in the location of the front on the order of one particle diameter with some features deviating by as many as two particle diameters. By the third frame, irregularity elements are typically three particles diameters in size, but can be as large as six diameters.

The effect of dissipation is also seen as the wave evolves. The energy input into the bed is initially focused in a narrow band near the wall as denoted by the high concentration of red particles. By the third frame, this energy is spread over nearly the entire width of the bed leading a reduction in the magnitude of the forces between particles. The combination of this energy diffusion with energy lost to inelasticity in the particle contacts leads to a net dissipation of the energy of the coherent wave detected at the pressure sensor.

For times later than those depicted in the three frames of Figure 6.3, some reflection of the wave from the right wall can be seen. After the first reflection, the wave becomes so weak and scattered that it can no longer be tracked as a coherent entity. Since no additional reflections can be observed, it is likely that the oscillations in the pressure traces are not due to subsequent reflections within the cell. The oscillations are more likely the result of a vibration of the force chains as been hypothesized in the experiments (see Section 4.2.1).

6.2 Parameter sensitivity

As shown in Section 2.2.2, the dimensionless scaling defines a limited number of parameters that are capable of affecting the scaled results. Assuming that the normal force is primarily responsible for transmission of wave energy, the focus should be on the parameters that influence this force. Recall that the normal force, F_n^*, is modeled as a combination of elastic and viscous contributions as

$$F_n^* = \frac{4}{\pi \left(1 - \nu^2\right)} R_{eff}^{*1/2} \delta^{*3/2} + \frac{6}{\pi \left(1 - \nu^2\right)} R_{eff}^{*1/2} A^* \delta^{*1/2} \dot{\delta}^*. \tag{6.1}$$

The only material properties that affect this force are Poisson's ratio, ν, and the dissipation factor, A^*. In what follows, the first two sections will explore the sensitivity of the simulation results to these two parameters. Additionally, the particle deformation and deformation rate will lead to changes in the normal force. The proscribed motion of the piston, as described by the maximum displacement and pulse width, will govern the evolution of these quantities. The sensitivity of the results to these pulse characteristics will be explored in the third and fourth sections.

The procedure for these sensitivity studies is as follows. A baseline set of parameter values was chosen based on property values for glass ($\nu = 0.220$, $A^* = 0.7$) and the pulse shape used in the moderate input pulse of Figure 6.1 ($d_{max}^* = 4 \times 10^{-4}$, $T_p^* = 80$). For each parameter, a range of values were spanned with all other parameters set to these baseline values. At each value in the range, five simulations were run. The results were found to depend on the initialization of the bed, so multiple simulations were performed both to examine the scatter of the results and to average out the configuration dependence.

6.2.1 Poisson's ratio, ν

The only material parameter on which the elastic force (the first term in Equation 6.1) depends is Poisson's ratio. Poisson's ratio also factors into the dissipative force, the second term in Equation 6.1. The dependence of the wave speed on Poisson's ratio is shown in Figure 6.4. The wave speed increases only slightly with ν for values typical of common materials. The materials used in experiments had range of Poisson's ratio 0.22 - 0.42. For larger values of ν (> 0.5), the wave speed increases more rapidly with ν.

The data in Figure 6.4 also show that the depth of the measurement in the bed has a significant effect on the wave speed. Depth increases the static pressure at which the wave speed measurement is made. The difference in the wave speed with depth is consistently greater than the scatter in the data.

Figure 6.4: Wave speed measured at detectors 20 (○) and 50 (□) diameters from the bottom of the cell for various values of Poisson's ratio. Five samples were taken for each ν value. The average of the resulting speeds is plotted with the standard deviation shown by error bars.

6.2.2 Dissipation factor, A^*

The dissipation factor governs the magnitude of the dissipative term of the normal force relative to the elastic term. For $A^* = 0$, collisions are fully elastic in the normal direction. A value of $A^* = 10$ leads to highly dissipative collisions, such that a particle will show no appreciable rebound after a collision.

The wave speed, c^*, shows little dependence on the dissipation factor as shown in Figure 6.5. Between A^* values of zero and one, the wave speed is constant with A^*. Only for larger values does there appear to be only a slight increase in the wave speed with the dissipation factor. The effect with A^* is particularly small in comparison to the change in wave speed with Poisson's ratio. The wave speed varied by nearly a factor of two with increasing ν. Here, there is less than a 10% change in the wave speed with the dissipation factor over the entire range.
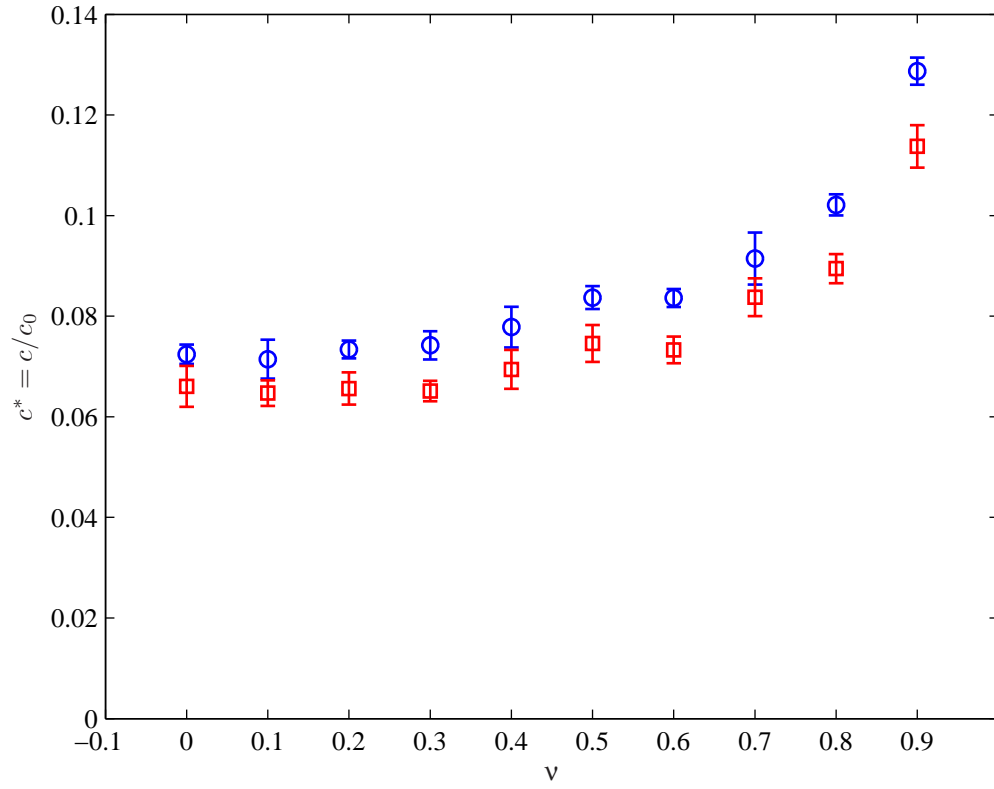

Figure 6.5: Wave speed measured at detectors 20 ($\circ$) and 50 ($\square$) diameters from the bottom of the cell for various values of the dissipation factor, A^*. Five samples were taken for each A^* value. The average of the resulting speeds is plotted with the standard deviation shown by error bars.

6.2.3 Pulse width

The width of the applied pulse dictates the duration of the disturbance in the system. Simulations covering a range of input pulse widths are useful in exploring the semi-permanent nature of the re-

sulting waves. Preliminary simulations suggested that the width of the detected wave was insensitive to the input pulse width. This set of simulations will explore this observation further. Since these simulations were performed at a constant value of the total displacement of the left wall, different values of the pulse width correspond to different values of the acceleration at (and applied force of) the left wall.
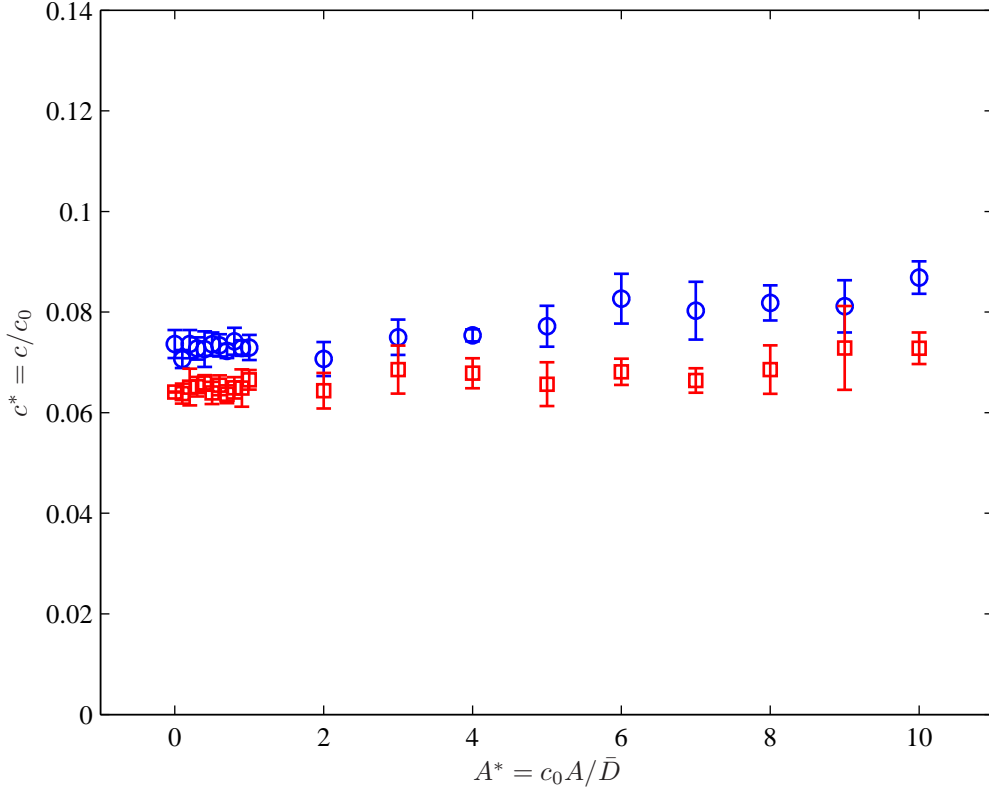

Figure 6.6: Wave speed measured at detectors 20 ($\circ$) and 50 ($\square$) diameters from the bottom of the cell for various values of the input pulse width, T_p^*. Five samples were taken for each T_p^* value. The average of the resulting speeds is plotted with the standard deviation shown by error bars.

Figure 6.6 shows the sensitivity of the wave speed to the input pulse width. There is a gradual decrease in the wave speed with increasing pulse width. There may be a greater increase in the wave speed for small widths, but the limited number of data points in this region makes this conclusion tenuous.

The limits of the width range explored are governed by the resolution of the simulations and observations of the detected wave shape. The smallest input pulse width examined was $T_p^* = 8$. At such small widths, the quasi-static approximation is marginal and temporal resolution begins to be a problem. As a result, we did not examine pulses widths shorter than this value. The upper range of the input pulse width is limited by a breakdown of the characteristic shape of the wave. Waves that result from larger pulse widths are irregularly shaped in comparison and exhibit no coherent wave

structure. This observation is in contrast to the experiments in which the wave width appeared to scale with input pulse width indefinitely. The experimental waves maintained an elevated pressure for the duration of the forward displacement of the piston. In the simulations, the pressure for large-width waves peaks and declines even while the force due to the displacement of the left wall is still applied. The difference between the experiments and simulations may be related to interparticle frictional effects. A reduced amount of friction in the simulations would allow the bed to expand instead of carrying the load applied by the piston.

Figure 6.7: Wave width measured at detectors 20 (○) and 50 (□) diameters from the bottom of the cell for various values of the input pulse width, T_p^*. Five samples were taken for each T_p^* value. The average of the resulting speeds is plotted with the standard deviation shown by error bars.

The dependence of the wave width on the input pulse width is shown in Figure 6.7. At the lower input pulse widths, the wave width is constant with input pulse width. This constant wave width is much greater than the input pulse width in this range and increases with depth in the bed. In this range, the waves are considered semi-permanent. Above $T_p^* = 200$, the wave width increases linearly with the width of the input pulse. These two regimes are similar to those that were observed in the experiments (see Figure 4.6). For all pulse widths examined in the simulations, the measured wave is wider than the input pulse.
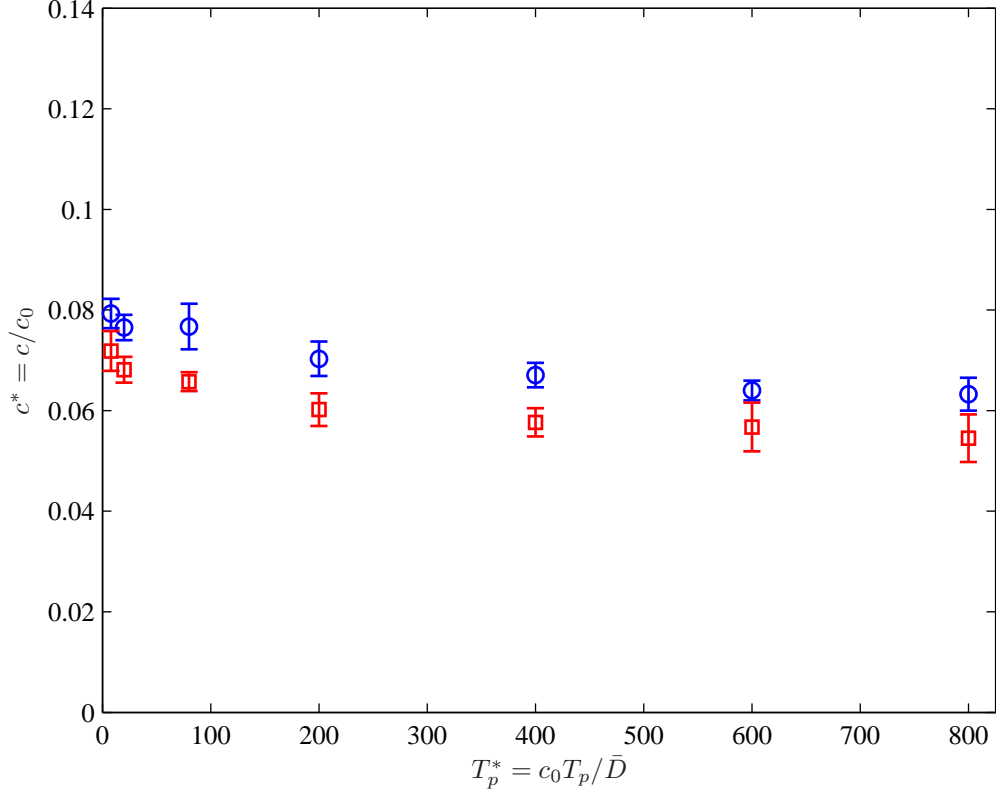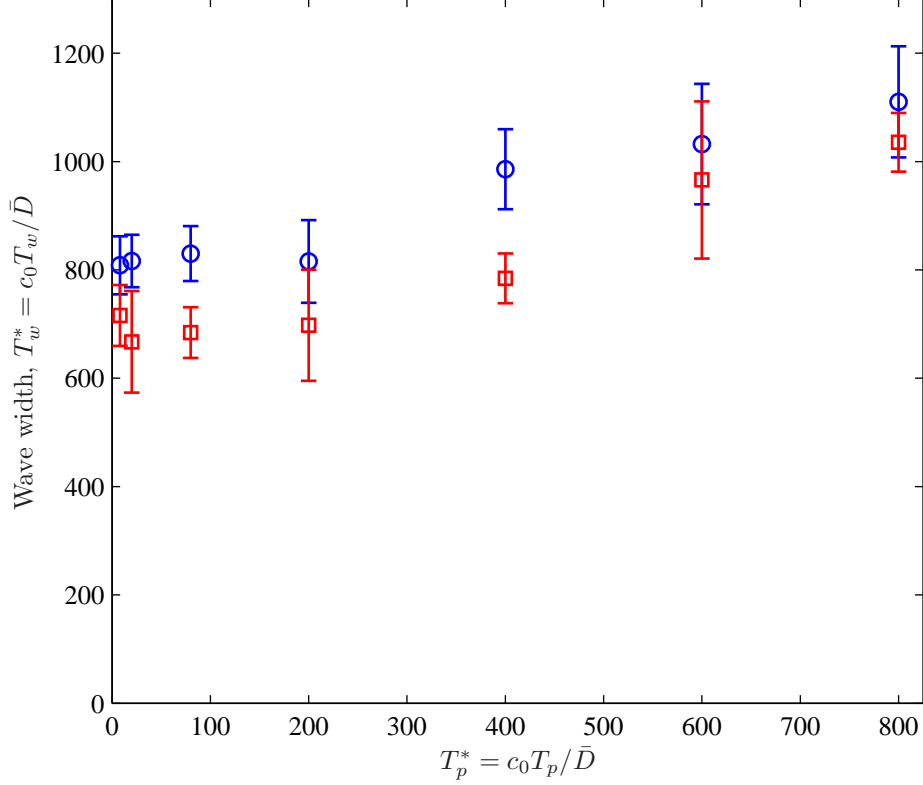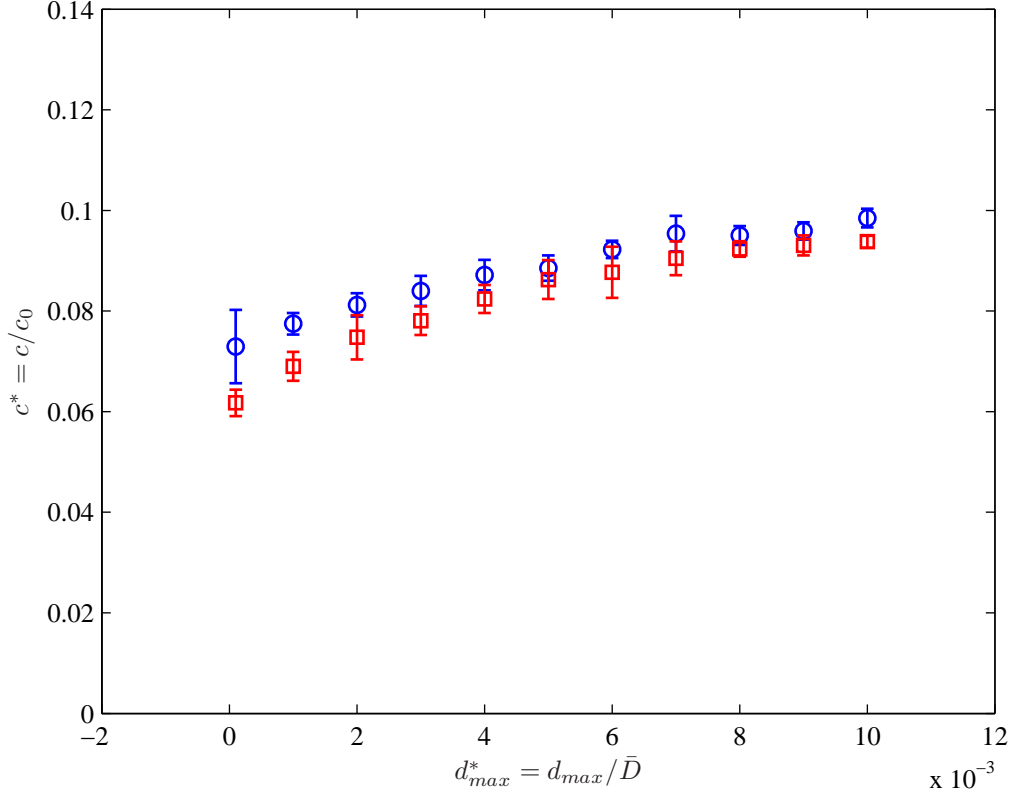
6.2.4 Pulse amplitude

Figure 6.8: Wave speed measured at detectors 20 ($\circ$) and 50 ($\square$) diameters from the bottom of the cell for various values of the maximum input pulse displacement, d^*_{max}. Five samples were taken for each d^*_{max} value. The average of the resulting speeds is plotted with the standard deviation shown by error bars.

A second characteristic of the pulse is its amplitude. Here, we probe the effect of the maximum input pulse displacement at a fixed value of the pulse width. In these studies, the smallest displacement of left wall of the simulation cell was $d^*_{max} = 1 \times 10^{-4}$. Below this value, the waves were too weak to be accurately detected. For the data points taken above $d^*_{max} = 1 \times 10^{-3}$, the shape of the waves was most like the example shown in Figure 6.2 in which a steep leading edge was observed. Smaller input displacement cases were more symmetric front-to-back like Figure 6.1. The largest displacement used was $d^*_{max} = 1 \times 10^{-2}$; at this value, the displacement is a significant fraction (10%) of the size of a single particle.

Figure 6.8 shows the dependence of the wave speed on the displacement of the input pulse. The wave speed increases with input pulse amplitude, plateauing at the larger values of the input pulse displacement. As the displacement of the pulse is increased, the effect of the depth of the measurement appears to decrease. For the smaller displacements, the difference in the speeds at the different sensor locations is more significant. The difference is narrowed at the larger amplitudes.

The behavior of the wave amplitude with input pulse displacement, Figure 6.9, is quite similar to that seen in the experiments (see Figure 4.10). At small displacements, the wave amplitude increases linearly with input pulse displacement. The slope is steeper for the measurement made deeper in the bed. The scatter in the data increases with increasing pulse amplitude. For the largest pulse displacements, the growth of the wave amplitude is no longer linear. The wave amplitude tends to level off at both detectors. In the experiments, the wave amplitude was seen to increase initially and then decrease unpredictably at large input pulse amplitudes. This effect and the increased scatter with amplitude were attributed to bed rearrangement in the experiments. These effects in the simulations also seemed to be linked to bed rearrangement.
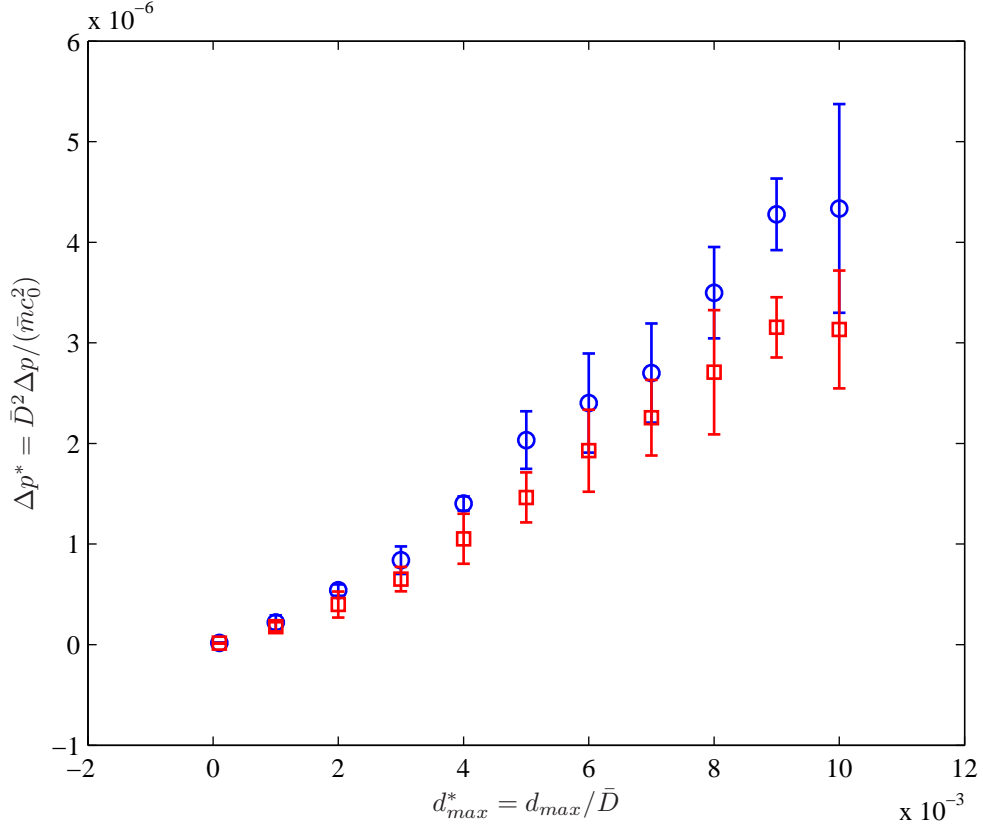
Figure 6.9: Wave amplitude, Δp^*, measured at detectors 20 ($\circ$) and 50 ($\square$) diameters from the bottom of the cell for various values of the maximum input pulse displacement, d_{max}^*. Five samples were taken for each d_{max}^* value. The average of the resulting speeds is plotted with the standard deviation shown by error bars.

A summary of the parametric studies is shown in Table 6.1. The dependence of a variety of measured bed and wave properties on the four main parameters of the normal contact model is listed. The solids fraction, σ, was found to only depend on the dissipation factor and this dependence was only minimal. At the very lowest levels of interparticle dissipation, the solids fraction was observed to increase. This increase may be the result of residual kinetic energy of the particles leading to a

	ν	A^*	T_p^*	d_{max}^*	S_{loc}^*
S_f	✗	✓	✗	✗	✗
p_0^*	✗	✗	✗	✗	✓
Δp^*	✓	✓	✓	✓	✓
T_w^*	✓	✓	✓	✗	✓
c^*	✓	✗	✓	✓	✓

Table 6.1: Trends of the solids fraction (S_f), static pressure (p_0^*), wave amplitude (Δp^*), wave width (T_w^*) and wave speed (c^*) on the simulation parameters: Poisson's ratio (ν), dissipation factor (A^*), input pulse width (T_p^*), maximum input pulse displacement (d_{max}^*), and sensor location (S_{loc}^*) in the sensitivity studies. A significant dependence is noted by a ✓ and no dependence is noted by an ✗.

slight reduction in the density of the bed. The static pressure, p_0^*, in the unperturbed bed scales with the depth of the measurement in the bed, as expected, but nothing else. The detected wave amplitude, Δp^*, is sensitive to all five simulation parameters. The measured wave width depends on all parameters except the input pulse displacement and the wave speed depends on all parameters but the dissipation factor.

The plots used to construct this table can be found in Appendix A.

6.3 Summary

Results from the simulations with a pulsed wave input show good agreement with the corresponding experiments, but allow for even greater exploration of the characteristics of these waves. Over a range of parameter values, the pressure traces from the simulations match the wave shapes seen in the experiments. The exceptions occur at the extremes of the values describing the input pulse shape. For the largest input amplitudes in the simulations, shock-like steepening is observed. Nothing like this was seen in the experiments. For the largest input widths in the simulations, the wave width does not continue to increase accordingly whereas the wave width appeared to increase indefinitely in the experiments. The explanation for this difference may lie in the treatment of friction at particle contacts in the simulations. Neglecting these extreme cases, the agreement in the shape of the waves for simulations and experiments is quite good.

One advantage of the simulations is the ability to visualize the wave at any point in the granular bed. In the experiments, measurements of the pressure can only be made at a few points in the bed. For the simulations, the force condition at any point in the bed is known. Using this knowledge, the wave can be imaged as it is transmitted between particle contacts. Such visualizations show the structure of the wave and how it varies with time and depth in the bed. Diffusion of the wave energy can be seen as the wave traverses the bed. This diffusion coupled with nonconservative particle interactions leads to a net dissipation that is evident in the pressure traces at the far wall of the

simulation cell.

The simulations also allowed for a much wider variation of the system parameters, particularly the material properties of the particles. Through sensitivity studies, a strong dependence was found for the wave speed on Poisson's ratio. Such a strong dependence was not expected beforehand. The dissipation factor, the pulse amplitude, and the pulse width were also found to affect the wave speed, but to a much smaller degree. The confining pressure (as dictated by the depth in the bed at which the measurement was made) was also found to strongly influence the wave speed. The effect of confining pressure is well documented (Goddard, 1990).

As was seen in the experiments, a semi-permanent regime was observed in the simulations for sufficiently small input pulse widths. In this regime, the detected wave width was insensitive to the input pulse width. A second similarity to the experiments was seen with changes to the input pulse amplitude. In the simulations, the wave amplitude increased with input pulse amplitude, but only to a point. The limit is theorized to be the result of particle rearrangement as it was in the experiments. The scatter also increased with larger input amplitudes, consistent with the experiment and the explanation of the particle rearrangement.

Chapter 7

Waves in an agitated granular bed

Creating an agitated state of the bed through shaking allows for the study of wave propagation with changing granular state. Any flowing granular material will be in such a nonzero granular temperature state. Knowledge about the characteristics of wave propagation in an agitated granular material may prove particularly useful as a means of diagnosing a granular flow. Agitation also complicates measurements that were already difficult in the unagitated state. But, unexpectedly, agitation also leads to some simplification of the observed behavior.

In this chapter, results from experiments and simulations of wave propagation in an agitated granular bed are presented. The experiments show that measurements are possible and highlight some of the nonlinear characteristics of the wave in the presence of agitation. The simulations complement these results and also provide insight into the structure of the wave as it crosses the bed.

Agitated granular beds with a sinusoidal wave input are examined in the first two sections of this chapter. Such continuous wave input provides information about the wave propagation characteristics over the entire cycle of the agitation. Although such input can reveal transient effects as the state of the bed changes throughout the agitation cycle, without a windowing procedure, any measurements will be an average over the entire agitation period. Experimental measurements are presented in the first section and complementary simulations are presented in the second section.

7.1 Experiments with continuous input

At the outset of these investigations, there was some doubt about whether wave propagation measurements could be made in the presence of agitation. Figure 7.1, which shows the pressure traces at the two transducers and the acceleration of the piston over two periods of the agitation, demonstrates that such measurements can be made. Although all three sensors detect the low frequency agitation introduced by shaking, they also record the input wave motion with minimal distortion. In fact, the input pressure waves are readily superimposed on the low frequency shaking. In all three
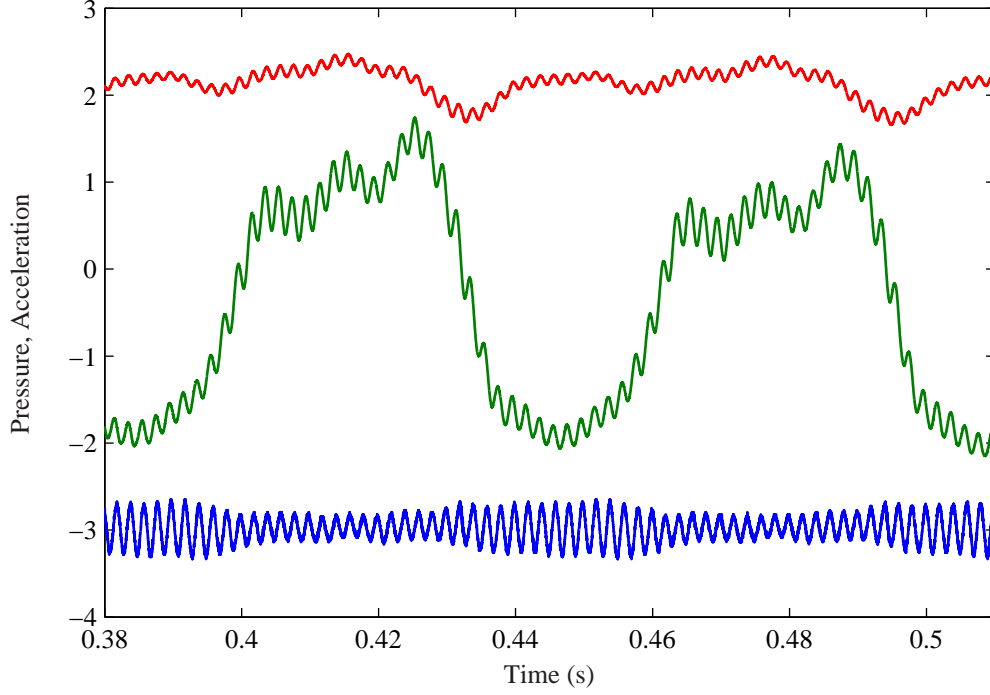
Figure 7.1: Raw signals for the near pressure transducer, far pressure transducer, and accelerometer (middle, top, bottom, respectively) for a vertically agitated bed with sound input in a horizontal direction.

signals, the high frequency input is apparent. The pressure transducer nearest the piston records the shaking frequency most clearly, but it is also seen in the more distant pressure transducer and the accelerometer. The agitation manifests itself in the accelerometer signal as an envelope of modulating amplitude. The amplitude is smallest when the pressure is largest because of the compressed state of the bed. Compression creates a higher pressure and restricts the motion of the piston leading to a smaller acceleration amplitude. Note that all three instruments are aligned with the direction of the piston and are thus perpendicular to the agitation direction.

An indication of the nonlinear nature of the agitated granular bed can be seen by looking at the spectra of the raw signals as exemplified by Figure 7.2. Peaks in the pressure transducer spectra show the input wave frequency (620 Hz) and the agitation frequency (20 Hz). In addition to these primary frequencies, there are also side bands at 20 Hz intervals around each of these peaks. Around the input wave frequency, these side bands are beat frequencies and are indicative of some quadratic nonlinearity. The precise origin of this nonlinearity is not fully known, but nonlinearities in a granular bed abound. The contact condition between particles alone introduces two nonlinearities. Around the agitation frequency, the side bands are harmonics. As evidenced by the relatively small peak in its spectrum at 20 Hz, the accelerometer is much less sensitive to the shaking than either transducer.
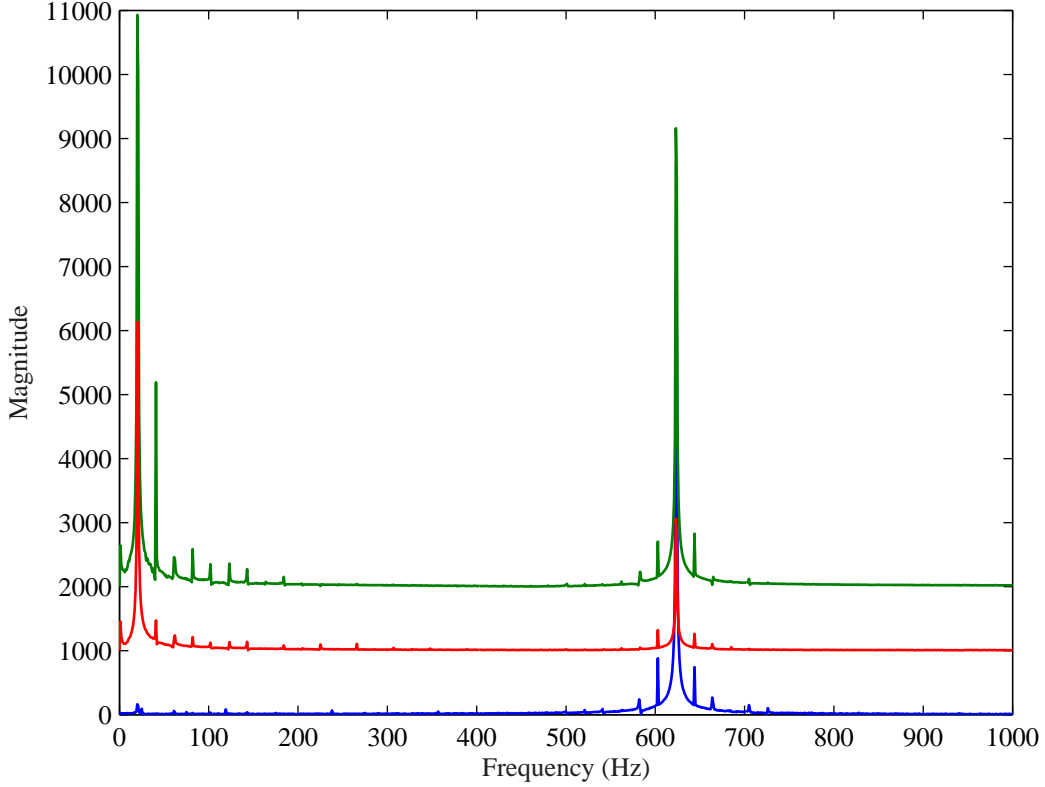
Figure 7.2: Spectra for the near pressure transducer (top), far pressure transducer (middle), and accelerometer (bottom) for a vertically agitated bed with wave input in a horizontal direction. Magnitude offset added for clarity.

Looking at this phenomenon in more detail, Figure 7.3 shows the evolution of the spectra as the shaking amplitude is increased. For no shaking, we see the peak corresponding to the input wave at 600 Hz with a harmonic at twice this frequency. The introduction of agitation leads to a second peak at the agitation frequency (20 Hz) and the side bands mentioned previously. The side bands are also present on the harmonic at 1200 Hz. As the shaking amplitude is increased further, the harmonic of the input wave source is reduced in favor of more side bands around both the shaking frequency and the input wave frequency. For the largest shaking acceleration amplitudes, the side bands span the entire frequency range between the input wave frequency and the agitation frequency.

Measurements of the phase speed in the presence of agitation are shown in Figure 7.4. Agitation leads to a change of state of the bed. The constant reordering of force chains brought on by external agitation constantly shifts the paths of wave propagation. These different states lead to different measured phase speeds. Thus, at low levels of shaking there is a large difference between the measured phase speed depending on the prior history of shaking of the bed. For both the glass and PVC particles, there is as much a 50 m/s difference in the phase speed at the same level of shaking. In this regime, wave propagation is governed by the geometric configuration of the bed
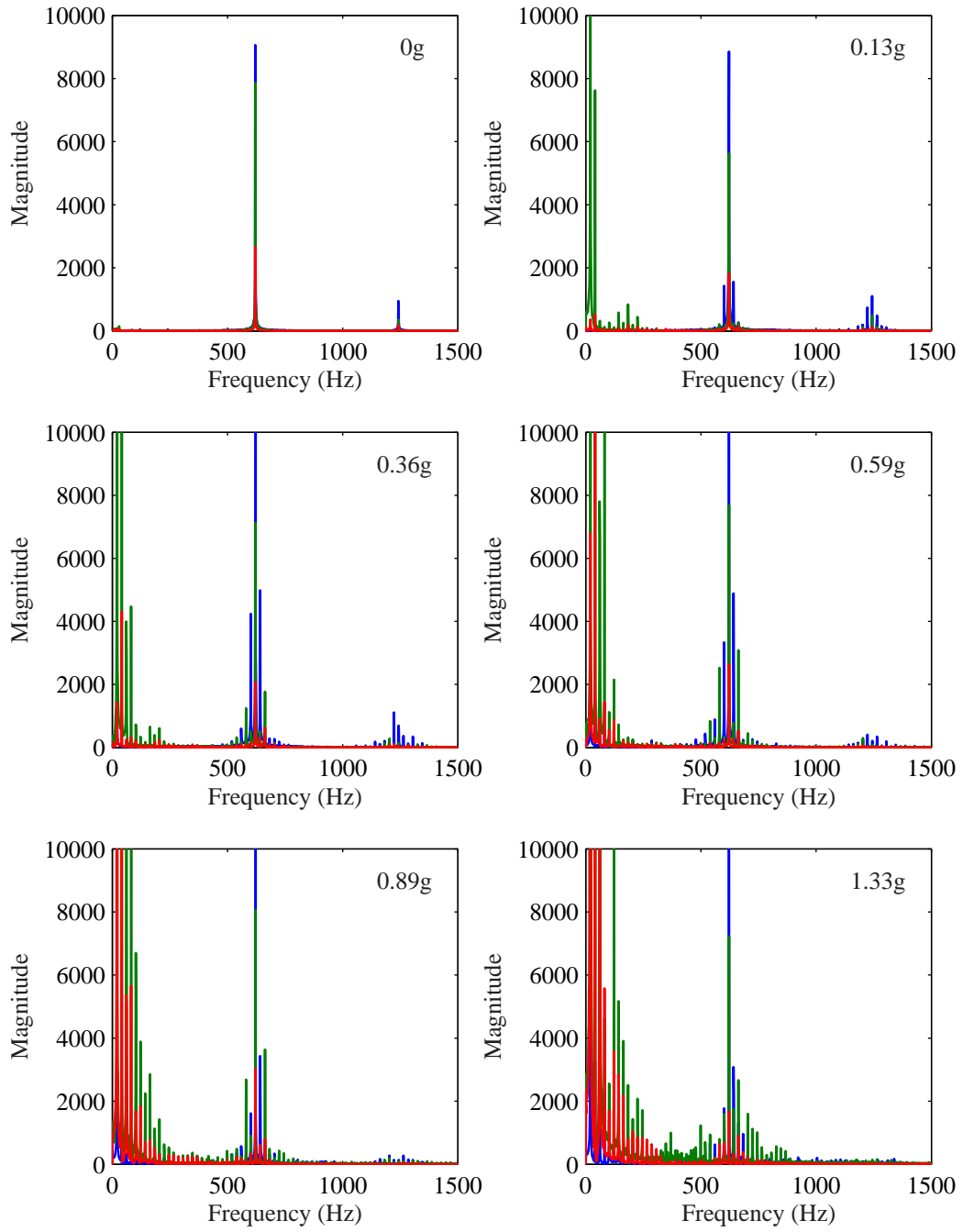
Figure 7.3: Spectra for the near pressure transducer, far pressure transducer, and accelerometer for an increasingly agitated bed with sound input in a horizontal direction. The acceleration amplitude is noted for each plot.

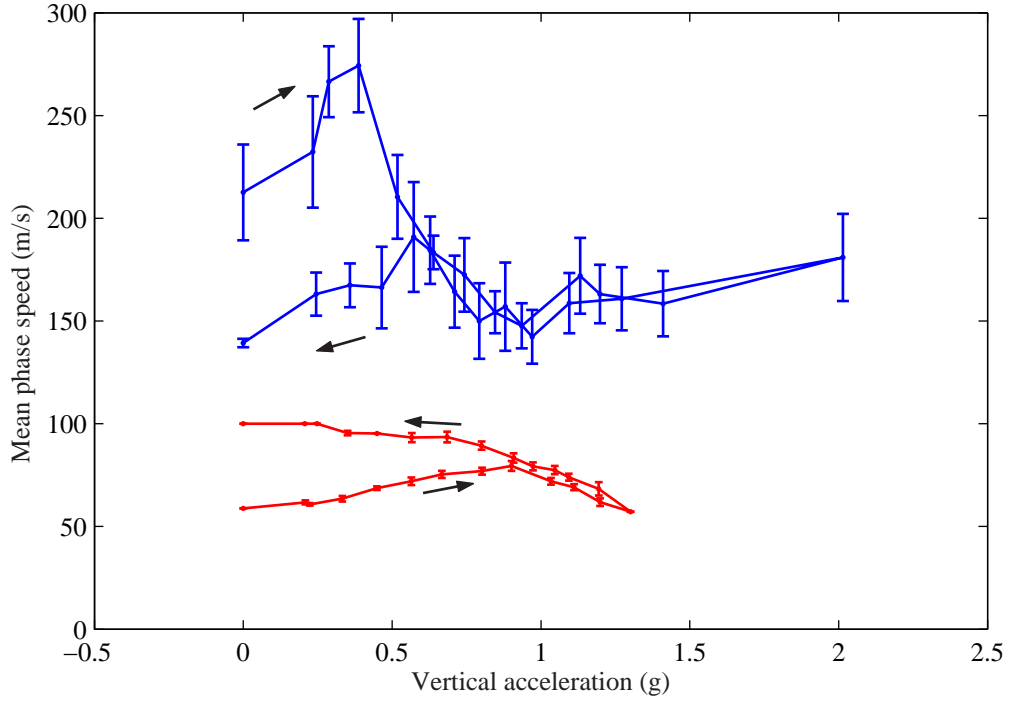which changes as a result of imposed agitation.

Figure 7.4: Phase speed in a shaken bed as the shaking amplitude is first increased and then decreased (shown by arrows). Each data point includes thirteen samples which were averaged. Error bars show the standard deviation of these thirteen values. Measurements were made in 4 mm glass spheres (upper curve) and PVC cylinders (lower curve).

For a large enough degree of agitation, a transition is observed and the variability of the phase speed measurements is significantly reduced. This transition occurs at a slightly different level of shaking for the glass (0.5g) and PVC particles (0.8g), but both levels are below the acceleration at which the particles detach from the base of the container (1g). Beyond this transition point, the phase speed is single-valued suggesting that the state of the bed is determined more by the level of agitation than the static geometric configuration of the particle packing that dominates at low levels of shaking.

The amount of scatter in the measurement of the phase speed is significantly lower for the PVC particles. This discrepancy is likely due to experimental realities more than an innate characteristic of the granular bed. The higher phase speed in the glass leads to less resolution in the measurement of the phase speed at a fixed sampling rate. The other possibility has more to do with the geometry of the particles. The regular, spherical glass particles would be more likely to undergo rearrangement under small loads. The cylindrical PVC particles are less free to rotate and would tend to jam more readily, thus requiring more force to cause a reordering of the packing of multiple particles. This particle mobility argument would explain the reduced scatter and also the delay in the transition to

singe-valued phase speed behavior in the PVC particles.

7.2   Simulations with continuous input

In this section, we present results from simulations with the same excitation as the experiments described in the previous section. The simulations agree well with the observations from the experiments.

Figure 7.5: Pressure signals measured at the source (upper curve) and a detector (lower curve) at half of domain height above the bottom of the simulation cell for combined vertical shaking (20 Hz, 0.5g) and horizontal wave input (500 Hz, 0.2g).

Figure 7.5 shows the pressure measured at the input and output of the simulation cell for a shaken granular bed. The pressure spikes in the first tenth of a second of the signal are an artifact of the simulation initialization. After this transient, the signals settle into a regular pattern. At this time scale both signals are dominated by the agitation frequency which is 20 Hz. This agitation, introduced as sinusoidal motion of the base plate, translates comparatively cleanly into a sinusoidal pressure envelope for the input signal. In contrast, the output signal is slightly distorted. This difference may be due to the way the measurements are made. The input measurement is made over the entire length of the simulation wall so pressure irregularities due to force chains are smoothed

out. The output measurement is made over only a fraction (10 particle diameters) of the simulation wall so effects of the heterogeneous nature of the bed are more readily seen.

A magnified view of these signals, Figure 7.6, shows that in addition to the signal envelopes corresponding to the agitation frequency, the signals also contain the high frequency wave input. This is qualitatively similar to the experimental signals in Figure 7.1. Since the input signal in Figure 7.6 is so cleanly superimposed on the shaking frequency, cross-correlation is still possible to calculate the wave speed. The low frequency component is removed through filtering before the cross-correlation is performed.

Another interesting characteristic of the signals is the time-varying amplitude of the high frequency portion of the signals. This behavior is most apparent in the measured pressure at the input. The amplitude at the peak of the agitation envelope is considerably larger than that at the trough. The peak corresponds to a compressed state of the bed as the floor pushes up against the weight of the bed. In such a compressed state, each of the force chains will have a greater prestress. Due to the nonlinearity of the contact relationship between particles (see Figure 1.2), an identical displacement will produce a greater force (pressure) in a chain with a higher prestress.

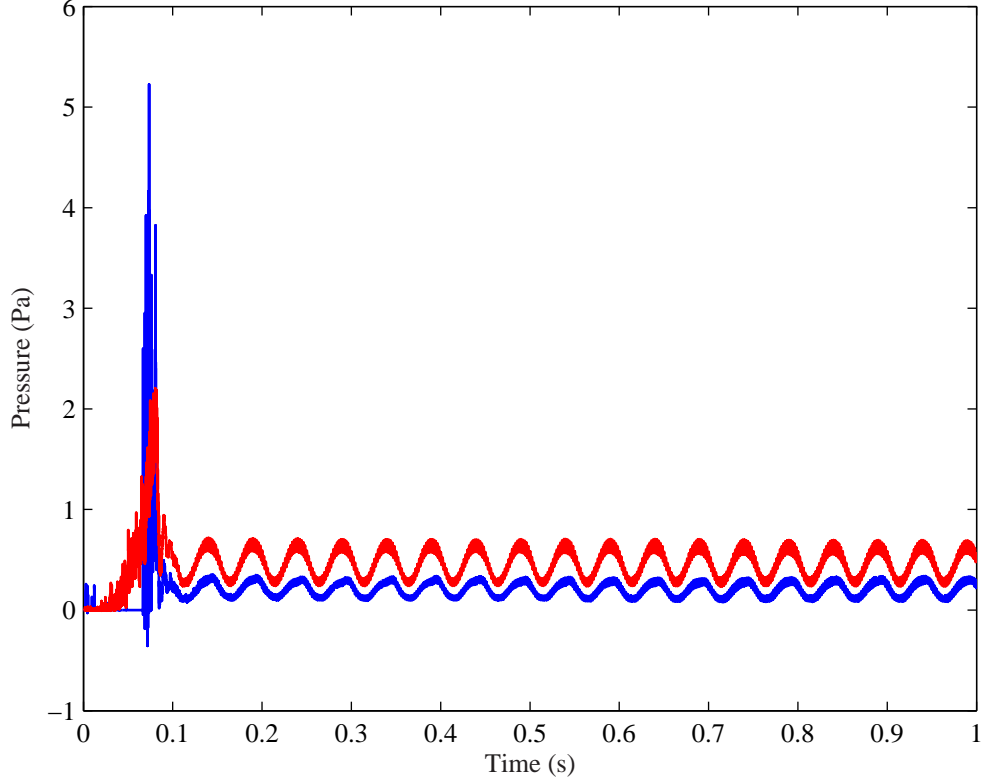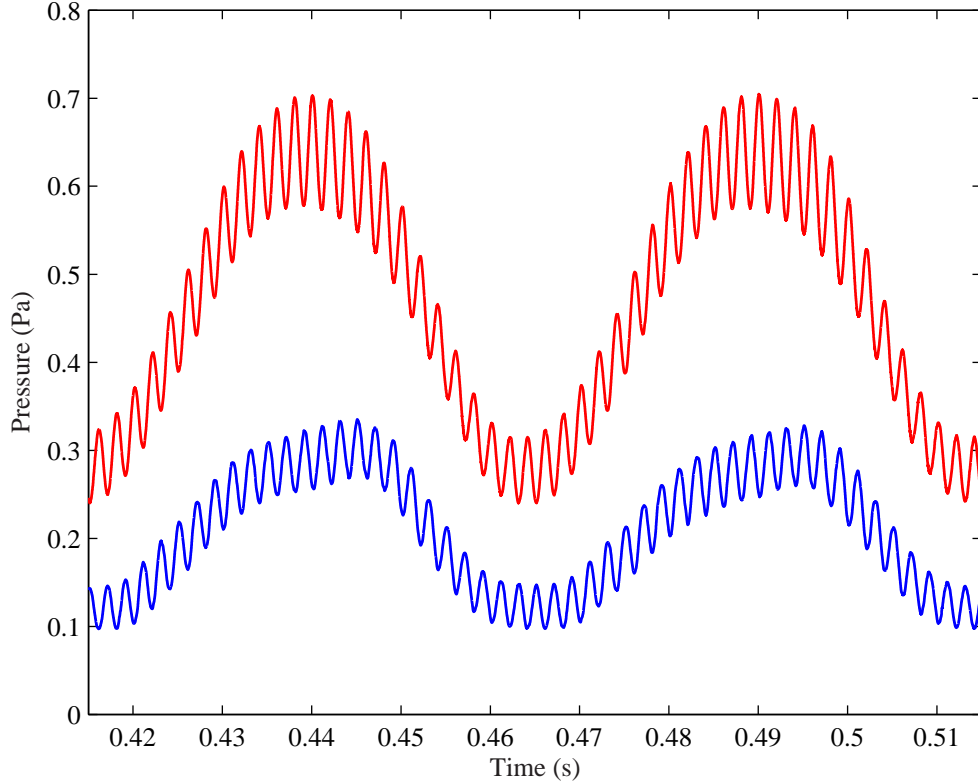Figure 7.6: Detailed view of the pressure signals after the settling period at the source (upper curve) and a detector (lower curve) half of the domain height above the bottom of the simulation cell for combined vertical shaking (20 Hz, 0.5g) and horizontal wave input (500 Hz, 0.2g).
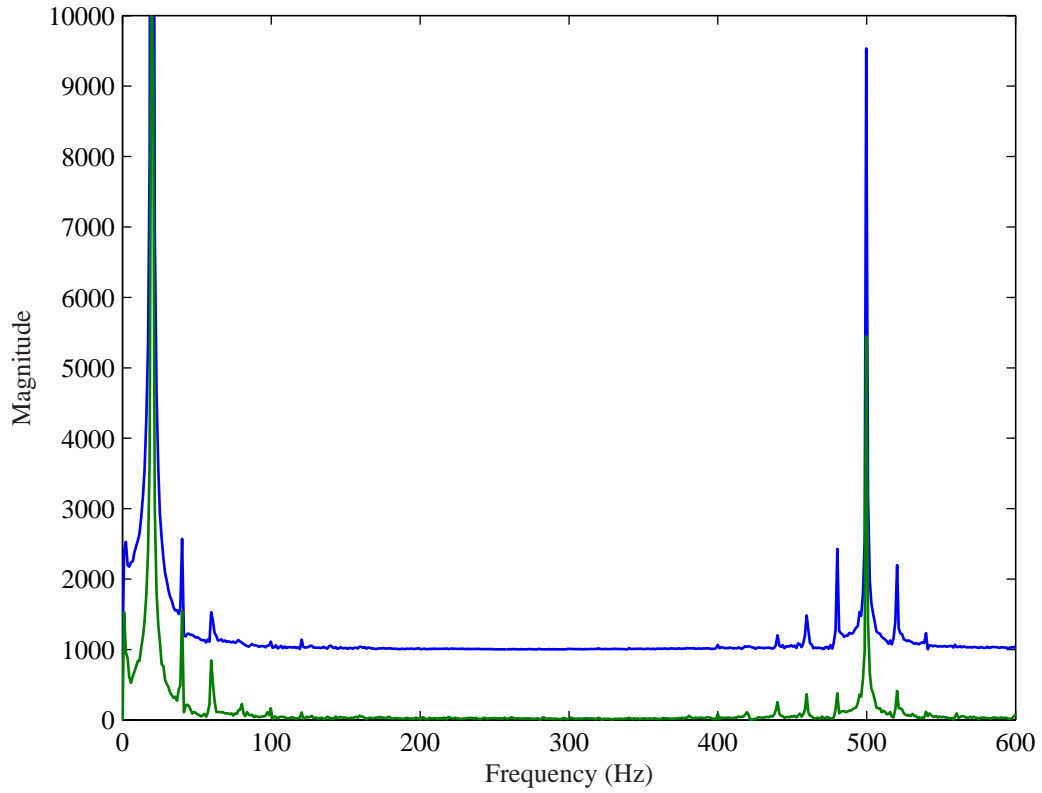
Figure 7.7: Frequency spectra for pressure signals at the source (top) and detector (bottom for combined vertical shaking (20 Hz, 0.5g) and horizontal wave input (500 Hz, 0.2g). Magnitude offset added for clarity.

Figure 7.7 shows the spectra of the pressure signals (comparable to the experimental measurements of Figure 7.2). The spectra demonstrate that nonlinearity, an inherent characteristic of granular beds, enters into the simulations as well. The strong peaks in the spectra correspond to the input wave and shaking frequencies. Beat frequencies in multiples of the agitation frequency are seen around the high frequency peak. This beating is the product of a quadratic nonlinearity in the bed. The condition at particle contacts is the source of at least two nonlinearities as shown in Section 1.2.4.

Clearly there must be some limit of agitation after which waves transmitted through particle contacts can no longer propagate in the granular bed. Once a significant number of particles come out of contact, there are no longer force chains along which to propagate pressure disturbances. Since the granular state changes throughout the agitation cycle, it is also possible that conditions exist for wave propagation only intermittently.
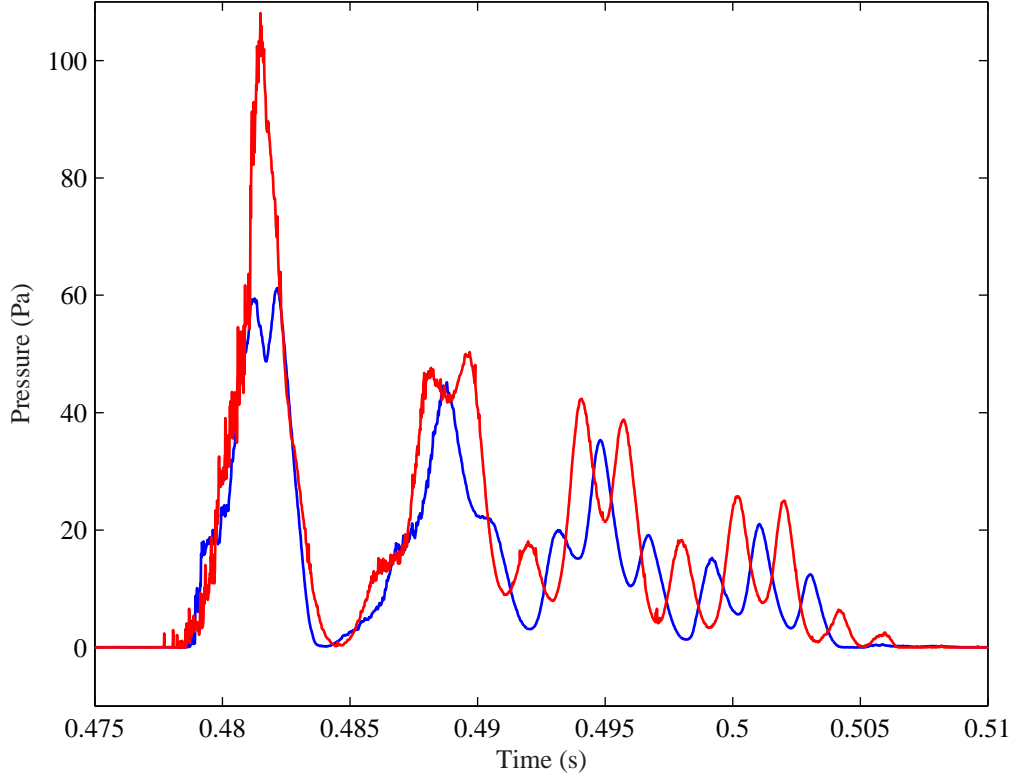

Figure 7.8: Detailed view of the simulated pressure signals after the settling period at the source and a large detector half of the domain height above the bottom of the simulation cell for combined vertical shaking (20 Hz, 1.25g) and horizontal wave input (500 Hz, 1.0g).

Figure 7.8 shows the pressure traces at the walls of the simulation cell over one period of the agitation cycle. The pressure shows the intermittent nature of propagation in a heavily agitated bed. The input wave frequency is evident over only a fraction of the agitation period- from 0.49 to 0.505 seconds. Over the rest of the cycle, the pressure is either zero or relatively large and noisy.

Regions of zero pressure indicate that the particles are out of contact with the wall at the sensor locations. Lack of particle contact suggests an expanded state of the bed. The large pressure spike near the beginning of the signal is the result of the impact of the granular bed on the base of the simulation cell. Wave propagation through particle contacts should be possible in this region, but the relatively weak input signal is obscured by the large pressure that results from the collision of the bed floor.

Phase speed measurements made over a range of agitation acceleration amplitudes are shown in Figure 7.9. The phase speed varies slightly with the agitation level, but nothing like was seen in the experiments (see Figure 7.4). The large variation in the experiments may be the result of a large particle to sensing surface size ratio. Such a condition is avoided in the simulations by scaling the sensor size with particle size. The measurements in the simulations use the phase shift in the input signal over the entire period of the agitation cycle to calculate the wave speed so this is only an average of a possibly transient quantity. The measurement does not take into account the variation of the granular state at various intervals of the agitation cycle.
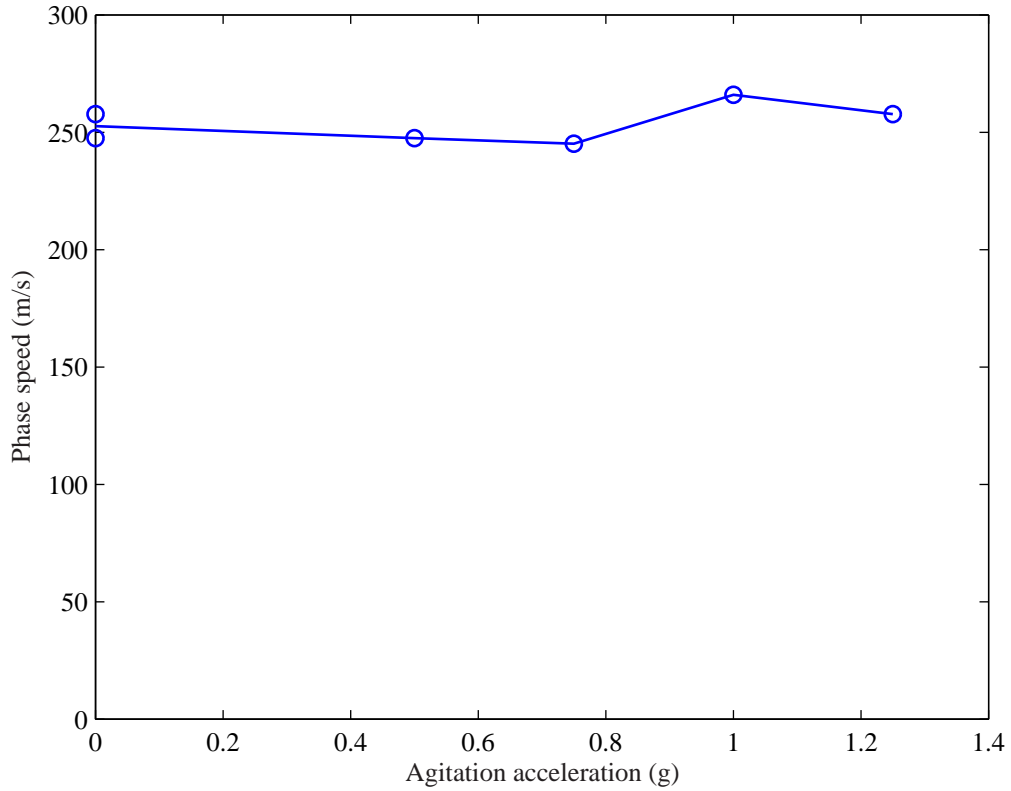

Figure 7.9: Phase speed in a simulated granular bed subject to varying degrees of agitation.

7.3 Experiments with pulsed input

In this and the next section, the focus is on pulsed waves in an agitated granular bed. This form of excitation allows for measurements of the wave propagation characteristics of the granular bed at a particular instant of the agitation cycle as the pulse width is much shorter than the agitation period. Experimental measurements are presented in this section and simulation results are presented in the next section.

Introducing a pulse at the piston while shaking the bed leads to a more complicated signal. The signal, as shown in the upper portion of Figure 7.10, is dominated by the shaking input. The signal at the distant transducer shows the sinusoidal nature of the shaking. For some unknown reason, there is a frequency doubling at the closer transducer. Both at this transducer and the far one, the shaking signal is remarkably consistent from one period to the next. This repeatability allows for a unique bit of data analysis.
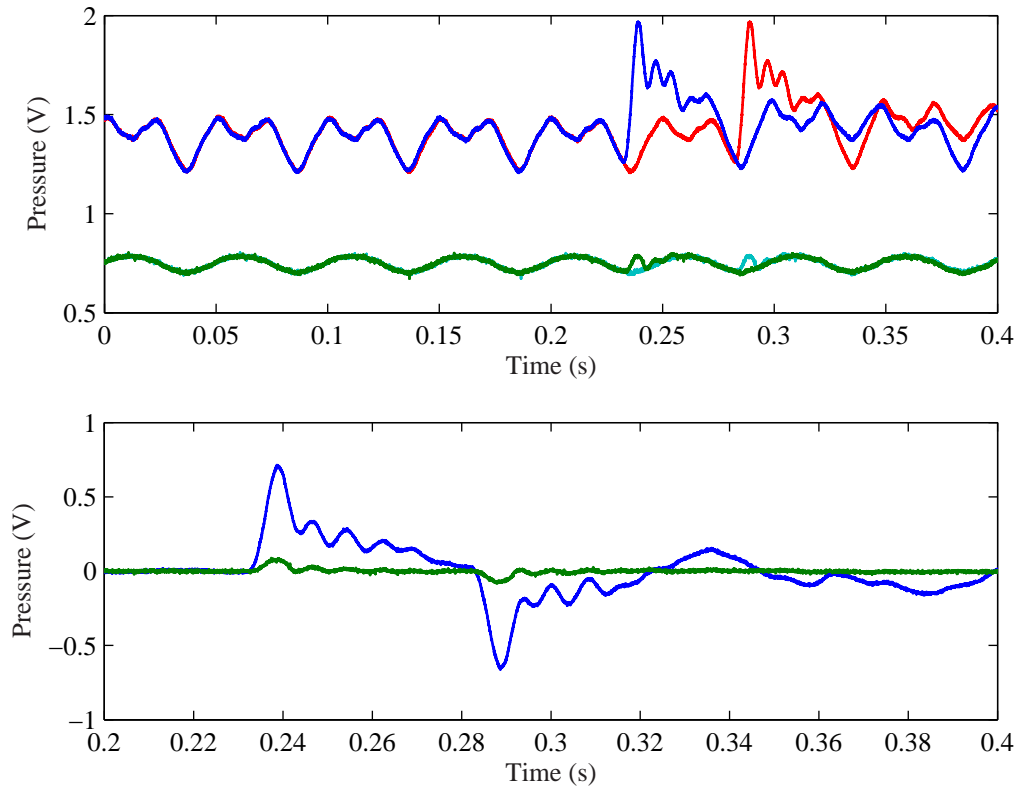
Figure 7.10: The top figure shows the original signals at the near (upper) and far (lower) transducer and also these signals shifted by one period of the shaking. The bottom figure shows the expanded result of subtracting the shifted signals from the original signals.

At the pulse of the piston, the signal takes on a rather clean combination of the shaking and pulse inputs (see Figure 7.10). To isolate the pulse input and remove the shaking component in the signal, the signals are shifted by one period as shown in Figure 7.10. The shifted signal is then subtracted

from the original signal, essentially subtracting out the effect of the shaking on the combined signal. The lower portion of Figure 7.10 shows the result of this subtraction on an expanded time scale. The results are similar to the signals recorded in the non-shaking cases. There is a primary peak followed by a series of oscillations. In contrast to the static signals, the oscillations in the subtracted signal start at a pressure of about half of the wave amplitude and decay linearly to the static pressure value.

Such a procedure assumes superposition of the signals, which may not be entirely valid due to the expected nonlinear nature of the signals. This problem would likely only affect comparisons of the wave amplitudes and attenuation. It should not interfere with the determination of the arrival of the wave and the ensuing wave speed.

7.4   Simulations with pulsed input

In this section, the corresponding simulation results of pulsed excitation in an agitated granular bed are presented. The simulations have the advantage that the structure of the wave within the bulk of the granular bed can be visualized. Such visualizations show how the granular state of the bed varies with depth in the bed as a result of the imposed agitation.

For a shaken granular bed, a pulsed wave can be used to diagnose the state of the bed. By making the input pulse width much shorter in time than the period of the agitation frequency, the wave will travel the width of the bed before any significant change in the bed state can occur.

An example of such a diagnostic pulsed wave is shown by its pressure trace in Figure 7.11 and is visualized in Figure 7.12. The instant of the shaking period captured here, as shown in the inset of Figure 7.11, is just after the bed floor has passed through its maximum elevation and is being pulled away from the bed faster than the bed can fall. A void is created by the retracting floor. As the particles expand into this void, an expansion wave travels upward from the bottom of the bed.

The pressure traces shown in Figure 7.11 demonstrate the variable state at different depths in the agitated bed. At the upper sensor, a wave is detected which is similar to, but slightly distorted from the waves measured in the static bed (see Figure 6.1). The trailing edge of the wave has additional localized peaks which may be the result of late arriving portions of the signal through force chains of variable construction. The amplitude of this wave is significantly smaller than either of the waves in the static beds. Its amplitude is two orders of magnitude smaller than the moderate input amplitude wave of Figure 6.1 and three orders smaller than the larger input amplitude wave of Figure 6.2. The relatively low amplitude is the result of a much lower confining pressure, represented by the static (background) pressure, compared to the non-shaken bed cases. The static pressure is two orders of magnitude smaller than that measured in either of the non-shaken cases. The reduced confining pressure is the result of the change of the state of the bed due to shaking.
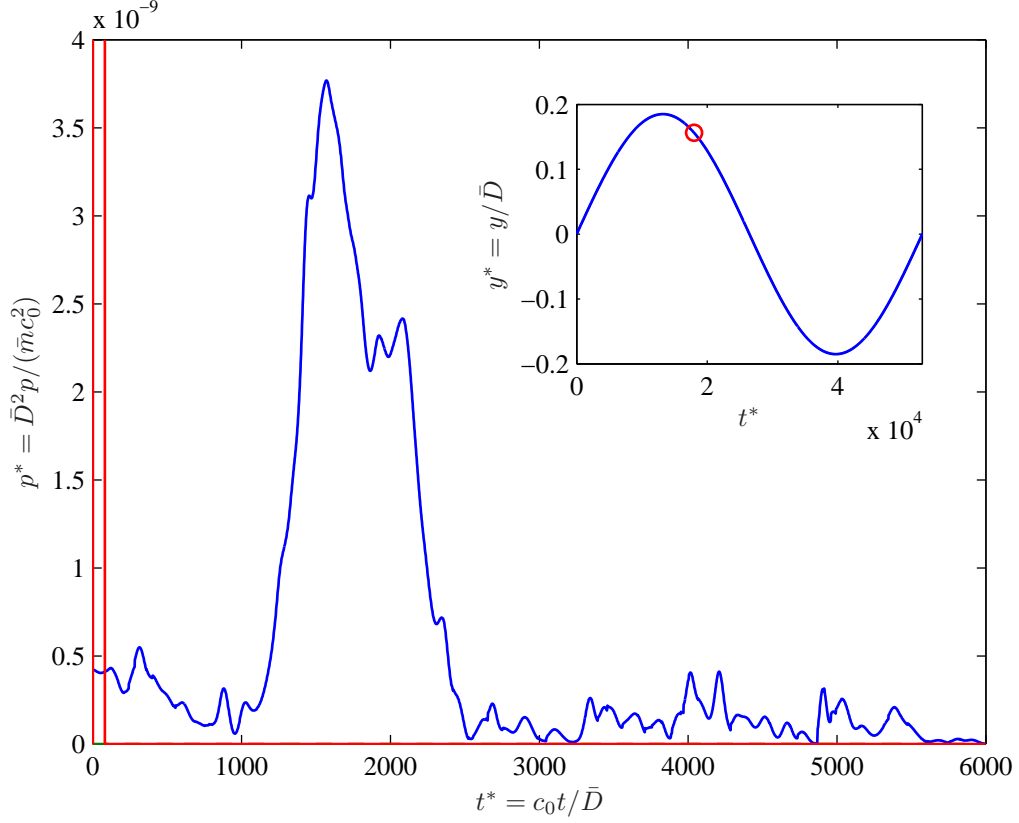
Figure 7.11: Wave shape resulting from a pulsed movement of the left wall. Pressure is measured on sensors (10 particles high) on the right wall 50 particles (solid) and 20 particles (dashed) from the bed floor. The base of the box is shaken with an amplitude of 1.5g. Inset is the position of the bed floor as a function of time with its current location denoted by the circle.

The pressure trace at the lower sensor also is plotted in Figure 7.11, but it goes unnoticed as its value is zero over the entire time shown. Near this sensor, the local density of the bed is so low that no wave can propagate. The confining pressure has been reduced to zero implying that particles are no longer in contact in the portion of the bed near the lower sensor. Without particle contact, no pressure peak can be detected at the lower sensor for this instant of the shaking trajectory. Once the bed is compressed by the floor, the confining pressure will be restored, and a wave will again be able to propagate.

The corresponding visualization, Figure 7.12, echoes the same conclusions seen in the pressure traces of Figure 7.11. Shading codes the magnitude of the net horizontal force on a given particle. Blue corresponds to zero force and red corresponds to a fixed force value of $F^* = 5 \times 10^{-9}$. In the lower half of the bed, the wave initiated at the left wall propagates a limit distance and loses all coherent structure before crossing even half of the bed. The expansion wave created by the retracting floor has reduced the local confining pressure to zero. Without a confining pressure, the particles lose contact. This lack of contact prevents elastic wave propagation. In the upper part of the bed,
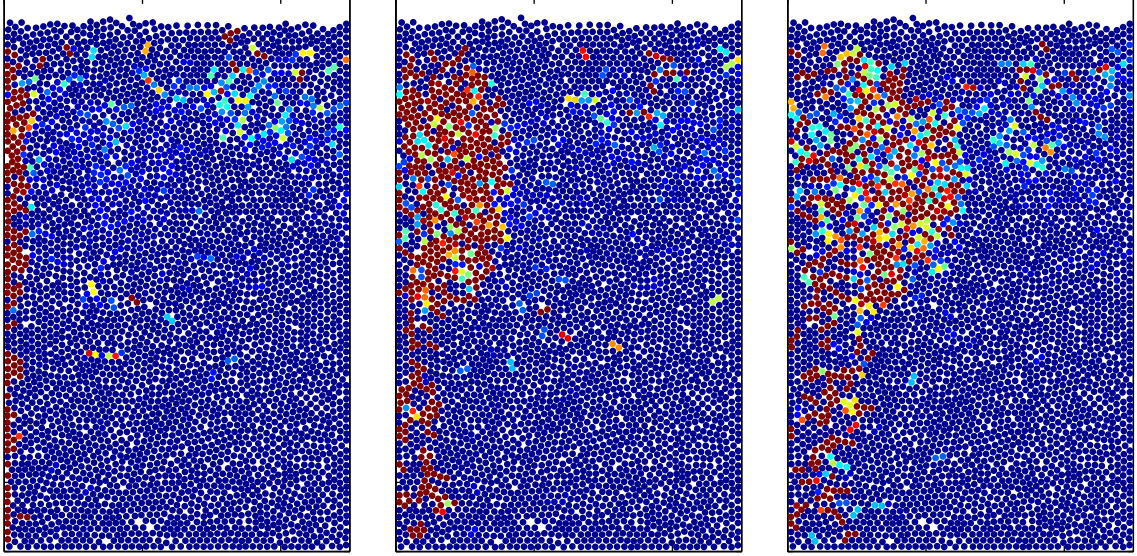
Figure 7.12: Transmission of a pressure wave in a shaken granular bed. Frames taken at intervals of $t^* = 250$.

where the expansion wave has not yet arrived, the input pulsed wave is still able to propagate.

Due to the relative weakness of the wave that does propagate, it is more difficult to comment on the structure of the wave than it was in the case of the static bed. Here, the wave front is parabolic in shape. The fastest portion of the wave travels through the particles around twenty diameters from the free surface. The wave speed decreases both toward the free surface and deeper in the bed toward the more expanded region where no wave can propagate.

The wave in the shaken bed is noticeably slower than those observed in the static bed cases. Both the visualizations (Figure 6.3 and Figure 7.12) of the waves and the pressure traces (Figure 6.1 and Figure 7.11) show evidence of the difference in speed. The visualizations start at the same time and the frames are taken at the same intervals. For the shaken case, it is clear that the high pressure front has not progressed as far across the bed as in the static cases. Likewise, the wave is detected at the pressure sensor sooner in the static cases. The pressure rises above the static value around t*=900 for the static case whereas this pressure change for shaken case occurs at t*=1100. The difference in wave speeds is likely due to the large difference in confining pressure between the static bed cases and the agitated bed case.

7.5   Summary

In this chapter, the characteristics of wave propagation in an agitated granular bed were explored. Imposed agitation actively rearranges the force chains through which the waves propagate. Given this fact, there was some question whether measurements of elastic waves were even possible.

Experiments for both a sinusoidal and a pulsed wave input showed that elastic waves could be detected and their properties determined. Although pressure traces included the effects of the shaking as well as the wave input, these contributions could be separated. For the continuous input cases, extraction of the wave input signal required a sufficient separation of the frequencies of the wave source and the agitation. Filtering was then used to remove the component due to the agitation. In the pulsed wave cases, the repeatability of the pressure due to the shaking allowed for a unique subtraction procedure. Simulations displayed the same superposition of the pressure components from the wave source and agitation and the signals were qualitatively similar to the experiments.

The spectra of the signals in the sinusoidal input experiments demonstrated the nonlinear nature of wave propagation in an agitated granular bed. In addition to peaks from the input wave and agitation frequencies, beat frequencies were observed at intervals of the shaking frequencies about the input wave frequency. The number of beat frequencies increased with the agitation acceleration amplitude. Such beating is indicative of a quadratic nonlinearity in the system. The corresponding simulations showed identical behavior in their spectra.

Wave speed measurements for the sinusoidal input experiments showed interesting behavior as the agitation amplitude was increased. For low shaking amplitudes, the wave speed took different values after undergoing an increasing then decreasing shaking cycle. Differences in the measured speed could be as great as 50 m/s. At sufficiently high shaking amplitudes the wave speed became single-valued. In this range, it appeared that the wave speed was governed more by the granular state rather than the geometrical configuration of the bed. The transition to this single-valued regime occurred at a different agitation amplitude for the glass spheres than the PVC cylinders. Simulations failed to exhibit such a high degree of wave speed variation at low agitation levels.

Simulations with sinusoidal input did show the temporal variation of the granular bed state at various intervals of the shaking. The input wave could only be detected during portions of the agitation period. At times when the bed was locally expanded, zero pressure was detected. During high pressure events, such as the collision of the bed floor with the granular bed, the input source was lost in this noisy pressure spike. The input wave signal was only evident at times when the bed was sufficiently compressed.

Simulations with a pulsed input further examined the effect of the state of the granular bed on wave propagation properties through it. Pressure traces and visualizations of forces within the bed showed that due to state changes induced by the shaking, wave propagation could be spatially localized. Propagation was possible in the upper layers of the bed where the bed was in a relatively compressed state. The expanded state of the lower portion of the granular bed prevented elastic wave propagation. In the region where propagation was possible, the wave speed was found to be lower than that measured in an unagitated bed. The slower wave was attributed to a lower confining pressure due to agitation.

Chapter 8

Discussion

This final chapter frames the observations of the previous chapters within the general concepts of the wave propagation in a granular material. The first section summarizes the results of the preceding chapters. After this summary, the focus turns to some additional analysis that unifies the main results of this thesis. The first of these sections categorizes the pulsed waves in relation to theoretical predictions for nonlinear waves in granular systems. The second section summarizes the effect of agitation on wave speed measurements in terms of a single system parameter, the local instantaneous confining pressure.

8.1   Summary

8.1.1   Unagitated bed

In the unagitated granular bed, two different forms of excitation were used to produce waves. The first type was a sinusoidal piston motion. This form of wave input allowed for the examination of the dispersion characteristics of the granular bed and the variability of measurements of the phase speed and attenuation with time. The second type of excitation was a pulsed movement of the piston. Such pulses create a wave of finite duration that provides information about the nonlinear nature of wave propagation in the granular bed. Experiments and complimentary simulations were performed for both forms of wave input.

The sinusoidal input studies were divided into two sets of experiments. The first set fixed the acceleration amplitude of the piston and varied the frequency. These experiments showed that the wave propagation was nondispersive as was previously observed by Liu and Nagel (1994). Since the propagation was nondispersive, the group velocity (which is a constant for nondispersive waves) was used to compare different experimental conditions. The greatest influence on the group velocity was found to be the material composition of the particles as characterized by the sound speed ($\sqrt{\frac{E}{\rho}}$) in the bulk material. The group velocity was measured to be 170 m/s in glass spheres and 70 m/s in

PVC cylinders. The effect of particle size was minimal. Consolidation and an increased overburden of particles increased the group velocity for the glass particles between 10-20%. Measurements of the attenuation showed an increasing trend with increasing frequency in an irregular fashion. The attenuation changed sharply with small changes to the frequency. Again, particle composition was found to have the largest effect.

Simulations with a sinusoidal input agreed well with the experiments provided the particle/particle interaction model was realistic. The simulated pressure signals were qualitatively similar to the experimental traces and the simulations also showed that the wave propagation was nondispersive. Group velocity measurements in the simulations resulted in higher values (252-277 m/s for glass particles). This mismatch with experiments indicates the need for some adjustment in the particle contact model. The simulations also displayed system resonances that were seen in the experiments.

The second set of sinusoidal input experiments involved fixing the piston frequency and varying the acceleration amplitude. These constant frequency experiments demonstrated the tenuous nature of the particle contact network. Measurements of the phase speed and attenuation in an unconsolidated bed showed a high degree of hysteresis while increasing and then decreasing the acceleration amplitude of the piston. Scatter was also high in these measurements as both the phase speed and attenuation varied with time at large input amplitudes. Both the scatter and the hysteresis are the result of particle and force chain rearrangement from the action of the input waves alone. Performing the same experiments in a consolidated bed led to more repeatable data and reduced scatter.

The second form of input into the granular bed was a pulsed wave. Such finite duration waves are particularly useful for probing the attenuation characteristics of the bed since the energy input is finite. The amplitude of these waves was seen to decrease exponentially with distance and the rate of decay was 2.5 times greater in the PVC particles than in the glass particles.

Two sets of experiments were performed to elucidate the relationship between the input pulse shape and the characteristics of the measured wave. In the first set, the amplitude of the input pulse amplitude was fixed and the pulse width was varied. A semi-permanent wave regime was observed for the smallest pulse widths. In this range, the detected width was 10 ms regardless of changes to the input width. Both the amplitude of the waves and the attenuation were constant at sufficiently large input widths, but increase for smaller widths.

Constant pulse width experiments confirmed previous observations on the effect of increasing wave amplitude. Particle rearrangement led to increased scatter and irregular changes in wave amplitude and width measurements for the largest input amplitudes. The wave speed showed no variation with wave amplitude. Any variation was lost in the relatively high degree of the scatter in the wave speed data compared to the other measurements. The wave speeds measured in both the glass (120 m/s) and PVC (60 m/s) particles were comparable to, but slightly smaller than the group velocities measured in the continuous input experiments.

In the course of these experiments, some interesting oscillations in the pressure signal were seen behind the primary pulsed waves. Due to the relatively low frequency (40-80 Hz) of these oscillations, they must occur over some appreciable length and may be the result of a natural frequency of the force chains. To support this idea, the oscillation frequency was compared to the confining pressure. Consistent with what is expected for the natural frequency of a force chain, the oscillation frequency increased for larger confining pressure and increased with the stiffness of the particle material. Analysis of a 1-D chain of particles showed that the natural frequency would be of the correct order for a chain of reasonable length (100 particles). The primary frequency of the chain was found to decrease rapidly as the length of the chain increased.

The effect of consolidation was also examined. Consolidation of the bed was seen to consistently decrease attenuation and increase the wave speed through the granular bed. Consolidation increased the wave speed from 140 to 175 m/s in the glass particles and from 60 to 80 m/s in the PVC particles.

Results from the simulations with a pulsed wave input showed good agreement with the experiments and allowed for even greater exploration of the characteristics of these waves. Over a range of parameter values, the pressure traces from the simulations match the wave shapes seen in the experiments. The exceptions occur at the extremes of the values describing the input pulse shape. For the largest input amplitudes in the simulations, shock-like steepening is observed. Nothing like this was seen in the experiments. For the largest input widths in the simulations, the wave width does not continue to increase accordingly whereas the wave width appeared to increase indefinitely in the experiments. The explanation for this difference may lie in the treatment of friction at particle contacts in the simulations. Neglecting these extreme cases, the agreement in the shape of the waves for simulations and experiments is quite good.

One advantage of the simulations is the ability to visualize the wave at any point in the granular bed. In the experiments, we are limited to measurements of the pressure at a few points in the bed. For the simulations, the force condition at any point in the bed is known. Using this knowledge, the wave can be imaged as it is transmitted between particle contacts. Such visualizations show the structure of the wave and how it varies with time and depth in the bed. Diffusion of the wave energy can be seen as the wave traverses the bed. This diffusion coupled with nonconservative particle interactions leads to a net dissipation that is evident in the pressure traces at the far wall of the simulation cell.

The simulations also allowed for a much wider variation of the system parameters, particularly the material properties of the particles. Through sensitivity studies, a strong dependence was found for the wave speed on Poisson's ratio. Such a strong dependence was not expected beforehand. The dissipation factor, the pulse amplitude, and the pulse width were also found to affect the wave speed, but to a much smaller degree. The confining pressure (as dictated by the depth in the bed at which the measurement was made) was also found to strongly influence the wave speed. The effect

of confining pressure is well documented (Goddard, 1990).

8.1.2 Agitated bed

Imposed agitation actively rearranges the force chains through which the waves propagate. Given this fact, there was some question whether measurements of elastic waves were even possible.

Experiments for both a sinusoidal and a pulsed wave input showed that elastic waves could be detected and their properties determined. Although pressure traces included the effects of the shaking as well as the wave input, these contributions could be separated. For the continuous input cases, extraction of the wave input signal required a sufficient separation of the frequencies of the wave source and the agitation. Filtering was then used to remove the component due to the agitation. In the pulsed wave cases, the repeatability of the pressure due to the shaking allowed for a unique subtraction procedure. Simulations displayed the same superposition of the pressure components from the wave source and agitation and the signals were qualitatively similar to the experiments.

The spectra of the signals in the sinusoidal input experiments demonstrated the nonlinear nature of wave propagation in an agitated granular bed. In addition to peaks from the input wave and agitation frequencies, beat frequencies were observed at intervals of the shaking frequencies about the input wave frequency. The number of beat frequencies increased with the agitation acceleration amplitude. Such beating is indicative of a quadratic nonlinearity in the system. The corresponding simulations showed identical behavior in their spectra.

Phase speed measurements for the sinusoidal input experiments showed interesting behavior as the agitation amplitude was increased. For low shaking amplitudes, the phase speed took different values after undergoing an increasing then decreasing shaking cycle. Differences in the measured speed could be as great as 50 m/s. At sufficiently high shaking amplitudes the phase speed became single-valued. In this range, it appeared that the phase speed was governed more by the granular state rather than the geometrical configuration of the bed. The transition to this single-valued regime occurred at a different agitation amplitude for the glass spheres than the PVC cylinders. Simulations failed to exhibit such a high degree of phase speed variation at low agitation levels.

Simulations with sinusoidal input did show the temporal variation of the granular bed state at various intervals of the shaking. The input wave could only be detected during portions of the agitation period. At times when the bed was locally expanded, zero pressure was detected. During high pressure events, such as the collision of the bed floor with the granular bed, the input source was lost in this noisy pressure spike. The input wave signal was only evident at times when the bed was sufficiently compressed.

Simulations with a pulsed input further examined the effect of the state of the granular bed on wave propagation properties through it. Pressure traces and visualizations of forces within the bed showed that due to state changes induced by the shaking, wave propagation could be spatially

localized. Propagation was possible in the upper layers of the bed where the bed was in a relatively compressed state. The expanded state of the lower portion of the granular bed prevented elastic wave propagation. In the region where propagation was possible, the wave speed was found to be lower than that measured in an unagitated bed. The slower wave was attributed to a lower confining pressure due to agitation.

8.2   Wave characterization

In this section, the pulsed waves are categorized by comparing the measured wave shape to that predicted by 1-D nonlinear wave theory as derived by Nesterenko (2001).
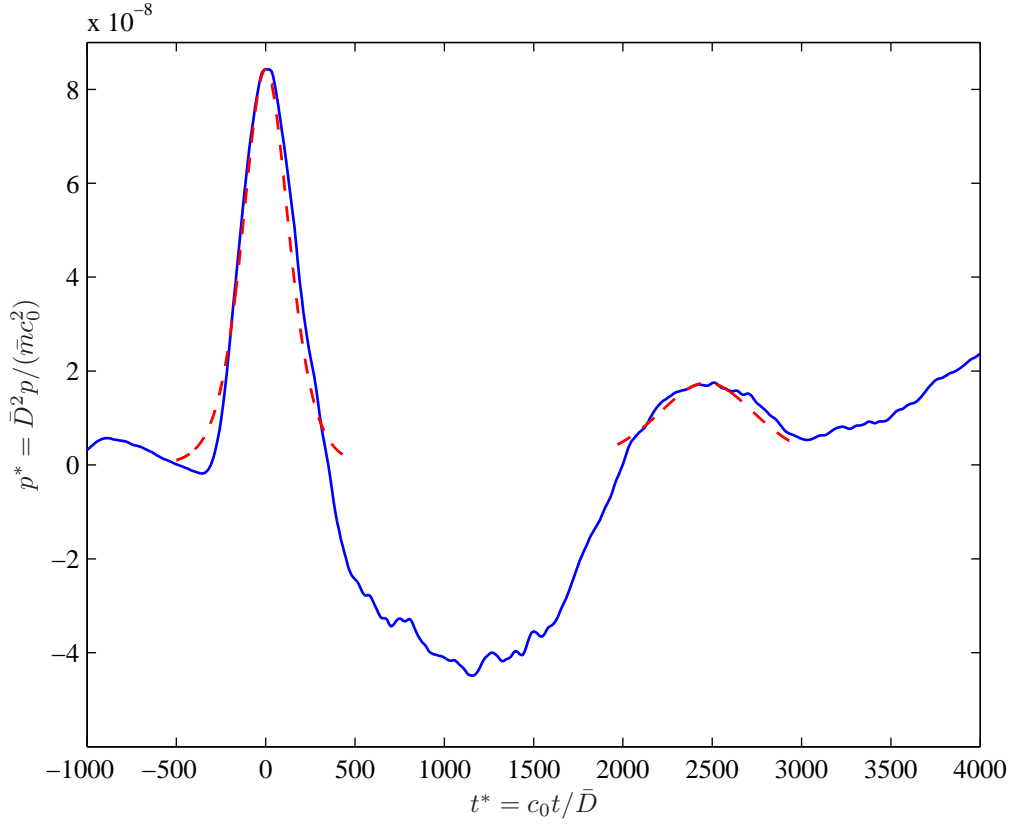

Figure 8.1: Simulated pressure trace (solid) compared to the theoretical shape (dashed) for a 1-D particle chain (Nesterenko, 2001).

Figure 8.1 shows a comparison between the wave shape recorded from simulations and the theoretical shape of a soliton predicted for a strongly compressed 1-D particle chain (see Section 1.2.4.1). The theoretical wave shape (Equation 1.12) is fit to the primary wave and also to a pressure peak following the primary wave that may be a secondary wave. The value of $\frac{\sigma}{c_s\gamma}$, which characterizes the composition of the chain and its initial compression, is chosen along with the amplitude, $\Delta\xi_m$, to fit the primary wave. For the secondary wave, the value of $\frac{\sigma}{c_s\gamma}$ is maintained and the amplitude

is adjusted to the detected value. The theory predicts the appropriate broadening of this secondary wave based on the reduction of the amplitude alone. Such scaling along with the relatively good fit of the theory to the observed shapes suggests that the simulated waves may in fact be the solitons predicted by the 1-D chain theory.

The second observation that agrees with the 1-D chain theory is the semi-permanent form of the waves for pulsed experiments and simulations. For small input pulse widths, the wave width was seen to be insensitive to additional changes to the input width or other characteristics of the input pulse shape. Due to dissipation in the current experiments and simulations, these waves can at best be semi-permanent. The dissipation leads to a reduction in amplitude over time, but from case to case, the wave width appears to be remarkably similar. Such a semi-permanent form is akin to predictions of the 1-D chain theory in the opposite limit, the weakly compressed chain (see Section 1.2.4.2). Solutions in this limit predict a wave with constant width that is nearly equal to five particle diameters.

Although some semi-permanent form is observed in the pulsed experiments and simulations, it is not to the degree or the magnitude of what is predicted by nonlinear 1-D theory. The simulations produce waves that are consistently larger in size (on the order of 100 particle diameters) than the five particle diameters predicted by the 1-D theory. Even by reducing the input pulse width, waves less than 100 particle diameters in width could not be produced. The difference may be related to the 3-D, random nature of a real granular bed. Additional degrees of freedom in three-dimensional beds permit more complex behavior that consequently makes comparisons with the 1-D predictions difficult.

8.3 Variation with agitation

For an agitated bed, the parameter that most affects the wave speed is the local confining pressure. As observed by Potapov and Campbell (1996), the solids fraction is a weak indicator of changes in the contact condition between particles. A significant change to the bed microstructure is required to significantly influence the solids fraction. In contrast, imperceptible changes in the microstructure were seen to affect wave propagation (Haff, 1987; Liu and Nagel, 1993). The local confining pressure is a much better predictor of changes at the particle contacts.

The dependence of the wave speed on the local pressure is shown in Figure 8.2. The effect of agitation is to extend the range of pressure over which the measurement can be made. Higher pressures can be reached when measurements are made in the compressed state of the agitation cycle. Lower pressures can be attained during expansion portions of the agitation cycle. The two sets of unagitated bed data correspond to measurements performed at two depths in the bed.

When plotted against the confining pressure, the results from the unagitated and agitated bed
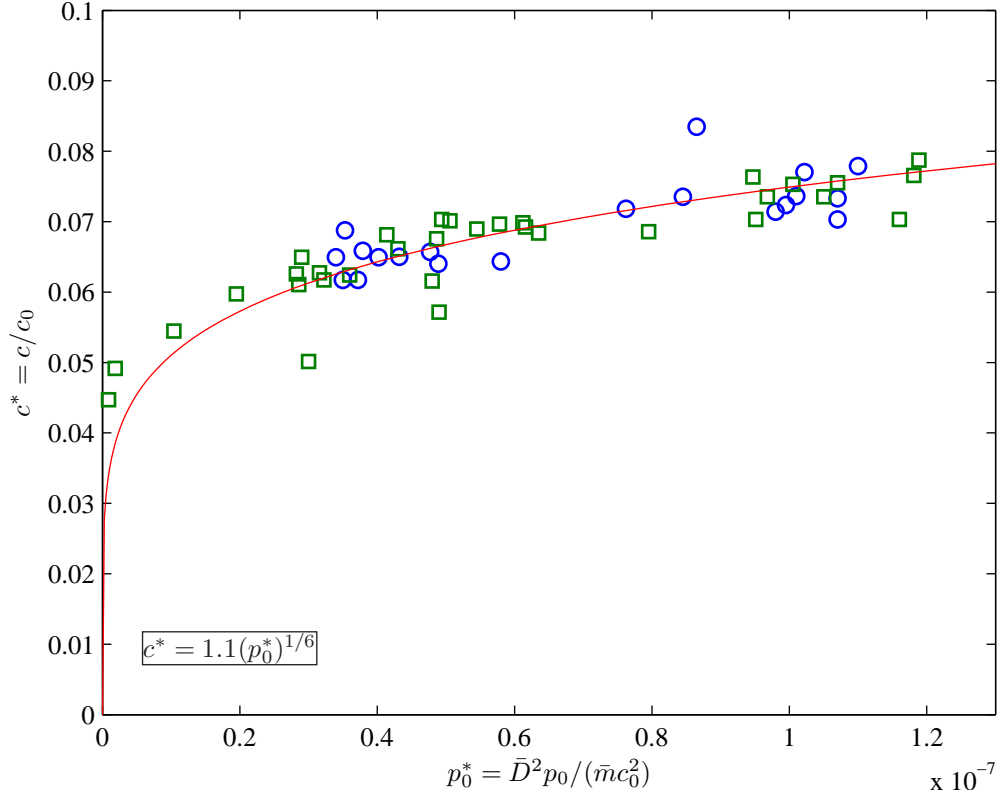
Figure 8.2: Wave speed as a function of the confining pressure, p_0^*, for pulsed wave simulations. Results from agitated ($\square$) as well as unagitated ($\circ$) cases are plotted.

cases coincide. The general trend is an increase in the wave speed with increasing local confining pressure, p_0^*. A power relationship with $1/6$ for the exponent (as predicted by theory (Goddard, 1990)) provides a good fit to the data. In real particle beds at low confining pressures, Goddard (1990) predicts a $1/4$ power relation; however the change from $1/6$ to $1/4$ is probably caused by asperities (Goddard, 1990). Such asperities are not included in the present simulations so the Hertzian prediction ($1/6$ power) is expected to hold over the entire pressure range.

Bibliography

G. Ben-Dor, A. Britan, T. Elperin, O. Igra, and J. Jiang (1997). Experimental investigation of the interaction between weak shock waves and granular layers. *Experiments in Fluids* **22**, 432–443.

N. V. Brilliantov, F. Spahn, J.-M. Hertzsch, and T. Pöschel (1996). Model for collisions in granular gases. *Physical Review E* **53**(5), 5382–5392.

C. S. Campbell (1990). Rapid Granular Flows. *Annual Review of Fluid Mechanics* **22**, 57–92.

C. S. Campbell and C. E. Brennen (1985). Computer-simulation of granular shear flows. *Journal of Fluid Mechanics* **151**, 167–188.

C. Coste, E. Falcon, and S. Fauve (1997). Solitary waves in a chain of beads under Hertz contact. *Physical Review E* **56**(5), 6104–6117.

P. Cundall and O. Strack (1979). A discrete numerical model for granular assemblies. *Geotechnique* **29**, 47–65.

J. Duffy and R. Mindlin (1957). Stress-strain relations and vibrations of a granular medium. *ASME Journal of Applied Mechanics* **24**, 585–593.

J. Duran (2000). *Sands, Powders, and Grains: An Introduction to the Physics of Granular Materials*. Springer.

J. Geng, D. Howell, E. Longhi, R. Behringer, G. Reydellet, L. Vanel, E. Clément, and S. Luding (2001). Footprints in sand: the response of a granular material to local perturbations. *Physical Review Letters* **87**(3).

J. Goddard (1990). Nonlinear elasticity and pressure-dependent wave speeds in granular media. *Proceedings of the Royal Society of London* **430**, 105–131.

W. Goldsmith (1960). *Impact*. Edward Arnold Publishers Ltd.

P. K. Haff (1987). Micromechanical aspects of sound waves in granular materials. In *Brown Bag Preprint Series*, no. BB-66.

S. Harada, S. Takagi, and Y. Matsumoto (2003). Wave propagation in a dynamic system of soft granular materials. *Physical Review E* **67**(061305).

B. Hardin and F. Richart (1963). Elastic wave velocities in granular soils. *ASCE Journal of the Soil Mechanics and Foundations Division* **89**, 33–65.

E. Infeld and G. Rowlands (2000). *Nonlinear Waves, Solitons, and Chaos.* Cambridge University Press.

H. M. Jaeger, S. R. Nagel, and R. P. Behringer (1996). Granular solids, liquids, and gases. *Review of Modern Physics* **68**(4), 1259–1272.

X. Jia, C. Caroli, and B. Velicky (1999). Ultrasound propagation in externally stressed granular media. *Physical Review Letters* **82**(9), 1863–1866.

K. Johnson (1987). *Contact Mechanics.* Cambridge University Press.

V. Kamenetsky, A. Goldshtein, M. Shapiro, and D. Degani (2000). Evolution of a shock wave in a granular gas. *Physics of Fluids* **12**(11), 3036–3049.

A. Lazaridi and V. Nesterenko (1985). The detection of isolated waves of a new type in a one-dimensional granular medium. *Journal of Applied Mechanics and Technical Physics* **26**, 45.

M. Leibig (1994). Model for the propagation of sound in granular materials. *Physical Review E* **49**(2), 1647–1656.

S. Leibovich and A. R. Seebass (1978). *Nonlinear Waves.* Cornell University Press.

J. Lighthill (1978). *Waves in Fluids.* Cambridge University Press.

J. F. Lindsay, D. R. Criswell, T. Criswell, and B. Criswell (1976). Sound-producing dune and beach sands. *Geological Society of America Bulletin* **87**, 463–473.

C. Liu (1994). Spatial patterns of sound propagation in sand. *Physical Review B* **50**(2), 782–794.

C. Liu and S. R. Nagel (1992). Sound in sand. *Physical Review Letters* **68**(15), 2301–2304.

C. Liu and S. R. Nagel (1993). Sound in a granular material: Disorder and nonlinearity. *Physical Review B* **48**(21), 646–650.

C. Liu and S. R. Nagel (1994). Sound and vibration in granular materials. *Journal of Physics: Condensed Matter* **6**, A433–A436.

H. Makse, N. Gland, D. Johnson, and L. Schwartz (1999). Why effective medium theory fails in granular materials. *Physical Review Letters* **83**(24), 5070–5073.

S. Melin (1994). Wave propagation in granular assemblies. *Physical Review E* **49**(3), 2353–2361.

NDEC (2004). *Talking About Disaster: Guide for Standard Messages.* National Disaster Education Coalition, Washington, D.C.

  URL http://www.disastereducation.org

V. F. Nesterenko (1984). Propagation of nonlinear compression pulses in granular media. *Journal of Applied Mechanics and Technical Physics* **5**, 733–743.

V. F. Nesterenko (2001). *Dynamics of Heterogeneous Materials.* Springer-Verlag New York, Inc.

F. Nori, P. Sholtz, and M. Bretz (1997). Booming sand. *Scientific American* pp. 84–89.

S. Ogawa (1978). Multitemperature theory of granular materials. *Proceedings of the US-Japan Seminar on Continuum-Mechanical and Statistical Approaches to the Mechanics of Granular Materials* pp. 208–217.

A. V. Potapov and C. S. Campbell (1996). Propagation of elastic waves in deep vertically shaken particle beds. *Physical Review Letters* **77**(23), 4760–4763.

B. Velický and C. Caroli (2002). Pressure dependence of the sound velocity in a two-dimensional lattice of Hertz-Mindlin balls: Mean-field description. *Physical Review E* **65**.

C. R. Wassgren (1997). *Vibration of granular materials.* Ph.D. thesis, California Institute of Technology.

G. B. Whitham (1974). *Linear and Nonlinear Waves.* John Wiley & Sons.

J. R. Zenit (1997). *Collision Mechanics in Solid-Liquid Flows.* Ph.D. thesis, California Institute of Technology.
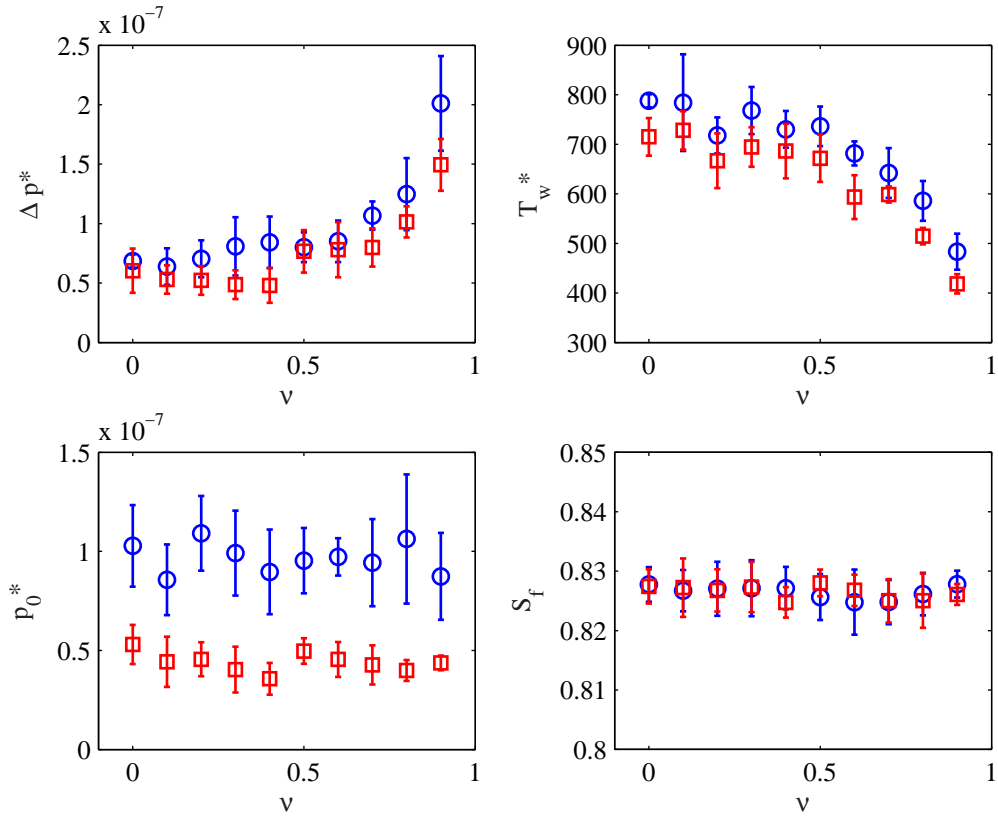
Appendix A

Additional parameter sensitivity plots

Figure A.1: Wave amplitude (Δp^*), wave width (T_w^*), static pressure (p_0^*), and solids fraction (S_f) measured at detectors 20 ($\circ$) and 50 ($\square$) diameters from the bottom of the cell for various values of Poisson's ratio, ν. Five samples were taken for each ν value. The average is plotted with the standard deviation shown by error bars.
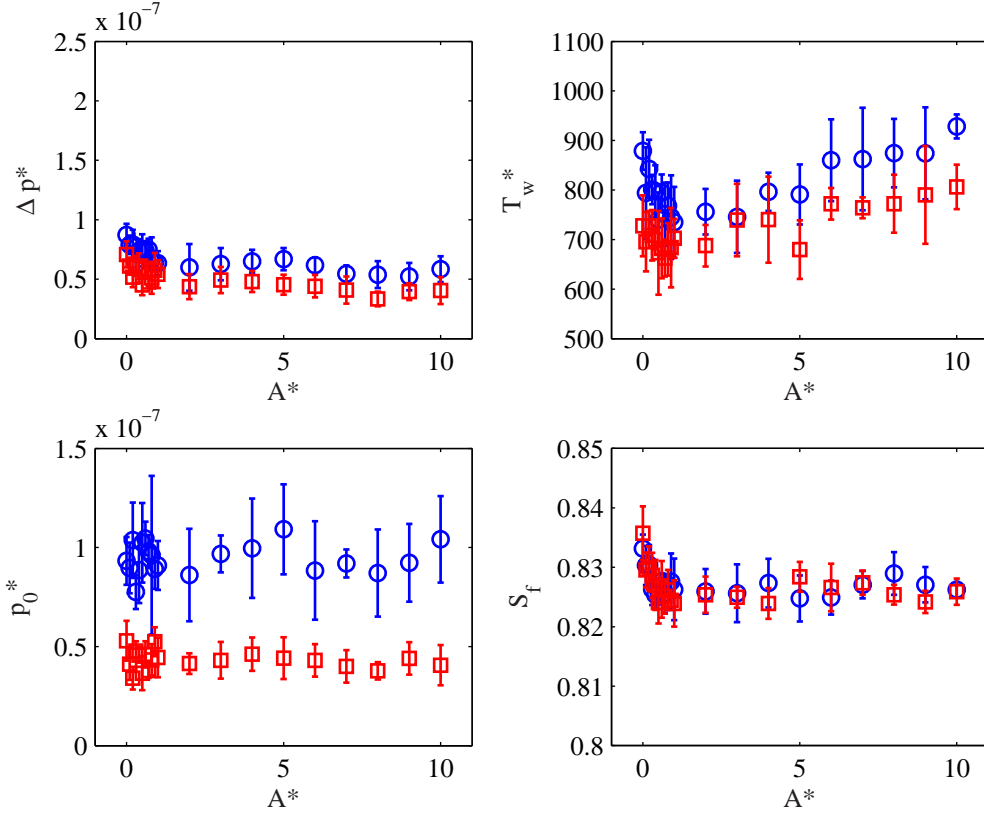
Figure A.2: Wave amplitude (Δp^*), wave width (T_w^*), static pressure (p_0^*), and solids fraction (S_f) measured at detectors 20 ($\circ$) and 50 ($\square$) diameters from the bottom of the cell for various values of the dissipation factor, A^*. Five samples were taken for each A^* value. The average is plotted with the standard deviation shown by error bars.
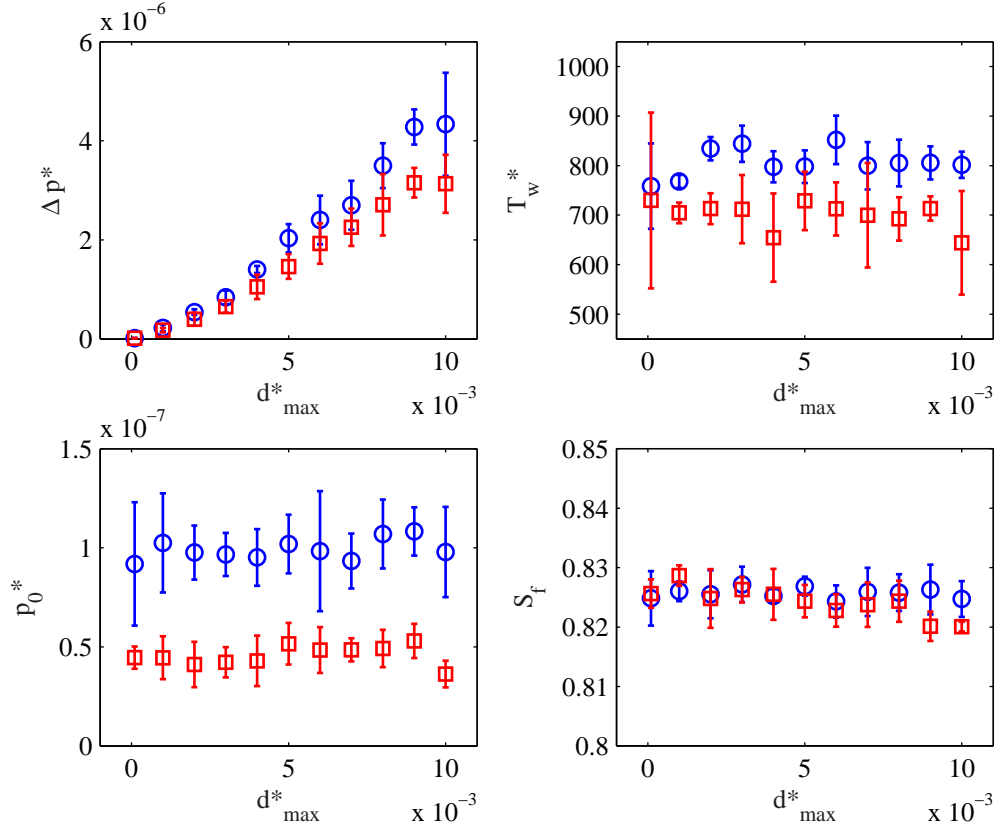
Figure A.3: Wave amplitude (Δp^*), wave width (T_w^*), static pressure (p_0^*), and solids fraction (S_f) measured at detectors 20 ($\circ$) and 50 ($\square$) diameters from the bottom of the cell for various values of the maximum input pulse displacement, d_{max}^*. Five samples were taken for each d_{max}^* value. The average of the resulting speeds is plotted with the standard deviation shown by error bars.
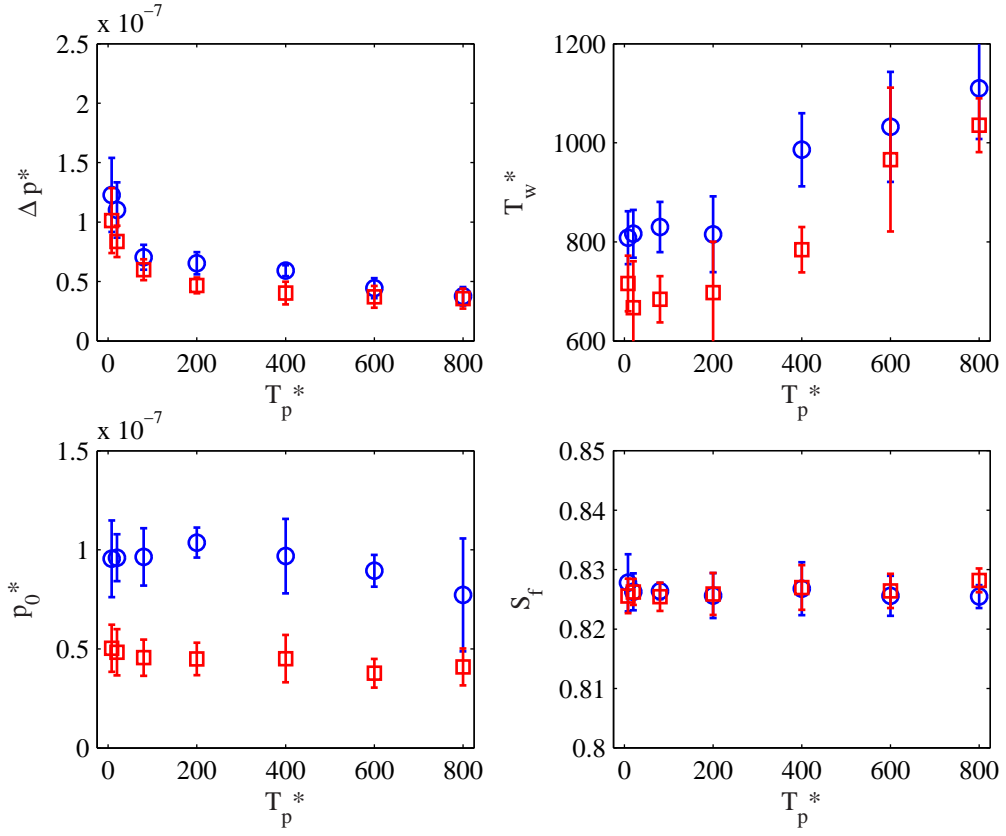
Figure A.4: Wave amplitude (Δp^*), wave width (T_w^*), static pressure (p_0^*), and solids fraction (S_f) measured at detectors 20 ($\circ$) and 50 ($\square$) diameters from the bottom of the cell for various values of the input pulse width, T_p^*. Five samples were taken for each T_p^* value. The average is plotted with the standard deviation shown by error bars.